INFLUENCE OF SOLID INCLUSION PHASE ON THE MECHANICAL BEHAVIOR OF THERMOPLASTIC POLYMER COMPOSITE AND BLEND

A Dissertation

by

PENG LIU

Submitted to the Office of Graduate and Professional Studies of
Texas A&M University
in partial fulfillment of the requirements for the degree of

DOCTOR OF PHILOSOPHY

Chair of Committee,	Hung-Jue Sue
Committee Members,	David E Bergbreiter
	Terry Creasy
	Chii-Der Steve Suh
Head of Department,	Andreas A. Polycarpou

August 2016

Major Subject: Mechanical Engineering

ABSTRACT

The objective of this work is to investigate the influences of the solid inclusion phase on the physical and mechanical properties of the thermoplastic polymer composites, as well as the mechanisms that cause the properties' deterioration upon exposure to hydrothermal environment. In order to obtain fundamental understanding of structure-property relationships of multicomponent polymeric materials, this dissertation work focuses on two important factors, which are the spatial dispersion of the inclusion phase, as well as its interface with the polymer matrix. Two different systems, polypropylene containing multiwalled carbon nanotubes (MWCNTs) and poly(ether ether ketone) (PEEK) containing 50 wt.% of poly(benzimidazole) (PBI) particles were employed as model systems.

Remarkable increases in modulus and strength of polypropylene, containing only trace amounts (0.1 wt.%) of individually dispersed F-MWCNTs were observed. The influence of the individually dispersed F-MWCNTs on the morphology of the crystal domains of PP and the mechanisms responsible for the observed increases in modulus and strength were examined.

PBI particles (average size 50 μm) were blended as an inclusion phase with PEEK to form a 50:50 weight ratio blend. The objective of this work is to investigate the reinforcing effect of PBI on performance in high temperature operating regimes (above 250 ºC). The interfacial affinity between PEEK and PBI at various conditions has been systematically studied by investigating the fracture behavior of PEEK/PBI blend.

In addition, all samples were studied by polarized optical microscopy and dynamic mechanical analysis (DMA) to establish correlation between the morphology and properties. An underexplored aspect of this blend system is connected with the tendency of the PBI component to absorb and retain significant amounts of moisture. The effect of retained moisture on the performance of this type of blend in certain application environments is poorly understood. This dissertation work investigates the mechanisms that cause the mechanical property deterioration of PEEK/PBI blends on exposure to hot water at 288 °C. In order to determine the underlying physics linked to property decrease, PEEK/PBI blends were subjected to several different treatments prior to characterization.

DEDICATION

To my beloved parents and my 24 year old self who stepped into the Ph.D. program of Mechanical Engineering at Texas A&M University.

ACKNOWLEDGEMENTS

I would like to give my most sincere gratitude to Dr. Hung-Jue Sue, who has provided valuable guidance and served as a role model during my stay here at Texas A&M University. I would like to thank my committee members, Dr. Bergbreiter, Dr. Creasy, and Dr. Suh, for their guidance and support throughout the course of this research. I would also like to thank Dr. Naraghi for serving as a substitute committee member during my final exam.

Special thanks to Dr. Tim Bremner for providing me with this great opportunity that has enabled me to acquire both the knowledge, as well as the critical thinking necessary for solving realistic engineering problems. Throughout the course of this research, and through various side projects, I have been very fortunate to have the opportunity to interact and exchange ideas with a number of experts in the polymer science community, and would like to personally thank Mr. Lorenzo DiSano of Ensinger North America, Dr. Jason Ren of Baker Hughes, Dr. Hiroaki Sugiyama and Dr. Michael Mullins of Dow Chemical Company for valuable discussions.

I also would like to thank Mr. Sean Kohl of Testing Machine Inc., Mr. John Wilson of TA Instruments and Mr. David Pollock of TA Instruments for the valuable discussions and technical assistances.

I would like to acknowledge the generous support provided by the consortium for Advancing Performance Polymers in Energy Appications (APPEAL) at Texas A&M University.

TABLE OF CONTENTS

Page

LIST OF FIGURES

FIGURE Page

LIST OF TABLES

CHAPTER I

INTRODUCTION

1.1 Background

During the past several decades, significant efforts have been devoted to the preparation and development of multicomponent polymeric materials, as evidenced by the large number of scientific papers and industrial patents dedicated to this class of materials. By blending different polymers or adding reinforcing particles into a polymer matrix, it is hoped that a combination of favorable properties may be obtained. Progress in multicomponent polymeric materials is most hindered by the fact that there is no clear understanding of the mechanisms by which morphology and microstructure directly influence bulk response in solid polymer composites or blends. This dissertation work focuses on gaining insights into the mechanisms by which morphology and microstructure directly influence bulk response in polymer composites and blends.

1.2 Research Scope

1.2.1 Polypropylene and CNT nanocomposites

Recently, nanometer-diameter filler particles have attracted great attention for their potential use in improving material properties. It is hoped that nanoparticles will not only afford improvements in material performance without reducing other properties, but that they may possibly be used to achieve multifunctional property enhancement, as is seen in high strength, high conductivity carbon nanotubes (CNTs).

Although great efforts have been made to integrate nanoparticles into polymeric materials, little progress has been made to understand the direct role of nanoparticles in controlling the physical behavior of the composite. This is largely due to the fact that most dispersion methods fail in establishing a consistent, stable dispersion of well-exfoliated CNTs unless there is significant physical or chemical modification to the polymer matrix and/or nanoparticles. This dissertation work presents the excellent dispersion and compatibilization of multi-walled carbon nanotubes (MWCNTs) inside of a commercial polypropylene (PP) [1]. The influence of trace amounts of individually dispersed MWCNTs on the crystallization, morphology, tensile and dynamic mechanical behavior of PP is reported. A discussion of the results correlates the tensile behavior with the microstructure of the system across broad length scales.

1.2.2 Polyether ether ketone (PEEK) and Polybenzimidazole (PBI) Blend

In the past decade, there has been a step change increase in the performance requirements of polymer-based materials in hydrocarbon exploration and recovery phases. For example, today there is a high demand for materials that are capable of withstanding high pressure (>15,000 psi) and high temperature (>200 °C) environments, at times accompanied by corrosive or reactive species like H_2S. Conventional fluoropolymer based materials tend to fail in service under these conditions. There is a rising demand for the development innovative polymer materials that can withstand harsh environments. The most popular and rapidly growing base polymer material for these applications comes from the poly(ether-ether-ketone) type of polymers. However, the elasticity of PEEK begins decreasing significantly at temperature above its T_g.

Improved properties with regards to the mechanical strength and creep behavior are desired for the applications that have a service temperature above 200 °C. The initial approach adopted by the industry focused on evaluating various high temperature thermoplastics and fluoropolymer compounds [2]. The results of five materials tested are shown in Table 1.1. Poly [2,2'-(m-phenylene-5,5'-bibenzimidazfole] (PBI) presents a T_g of 420 °C. It can be used in high temperature due to its high glass transition temperature (T_g) and good retention of mechanical properties at elevated temperature as shown in Figure 1.1 and 1.2 [3]. However, the presence of the imide group in its chemical structure results in a tendency to retain a significant amount of water. By itself, it is not an ideal material for harsh environment application when a large amount of water is involved. This dissertation work covers the preparation and properties of a PEEK/PBI 50:50 polymeric blend used to serve as a structural material in high temperature environments up to 288 ˚C. The PEEK/PBI type of polymer blend has many desirable features when compared to the conventional fluoropolymer based commercial thermoplastics, in low chemical reactivity, high corrosion resistance in acidic and caustic environments, high modulus. The PEEK/PBI blend offers an upper end operating temperature at 300 ºC. The DMA storage modulus curves in Figure 1.3 below reflect the higher retention of modulus at elevated temperature for the PEEK/PBI blend relative to pure PEEK [2]. This dissertation works also investigates the mechanisms that cause the deterioration of mechanical properties after harsh environment exposure.

Table 1.1. Initial Laboratory Material/Design Evaluation of polymeric compound used in seal element. The test protocol follows by pressurizing the seal element made of various polymeric compounds at room temperature. After 3 hours under these conditions, the temperature was raised to 343 ˚C if a reasonable seals was established at room temperature [2].

Material	Results
100% PBI	Small amount of leaking at ambient temperature. Cracks that propagated from a chipped edge is observed. No significant deformation is observed at high temperature.
Compression Molded PEK/PBI	The seal held at 2500 psi water at 21 °C with 17,500 lbs clamping force applied. The seal failed at 335 °C due to significant deformation.
Compression Molded PEEK	No seal is achieved at 21 °C even with 50,000 lbs of applied clamping force.
Compression molded PEEK/PTFE/Carbon fiber	The seal held at 2500 psi water at 21 °C with 50,000 lbs clamping force applied. The seal failed at 300 °C due to significant deformation.
Compression molded PTFE/Graphite with metal mesh backup	The seal held at 2500 psi water at 21 °C with 7500 lbs clamping force applied. The seal failed at 343 °C due to significant deformation.

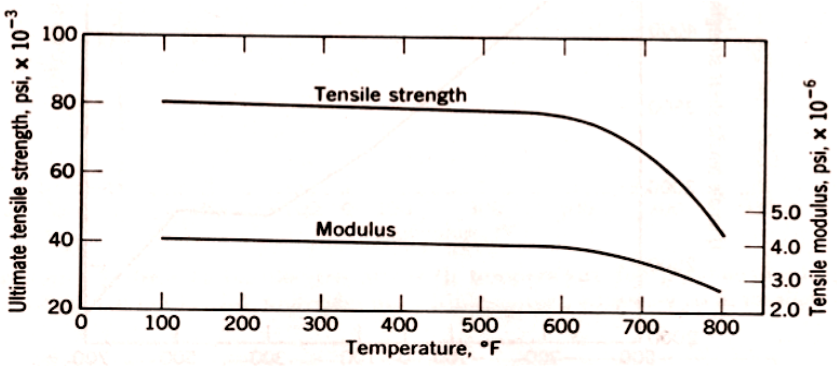

Figure 1.1. Tensile strength and modulus of poly (2,2'-m-phenylene-5,5'-bibenzimidazole) as a function of temperature. Figure reprinted from Encyclopedia of Polymer Science and Technology, Levin H.H. Copyright (1999-2014), with permission from John Wiley and Sons[3].

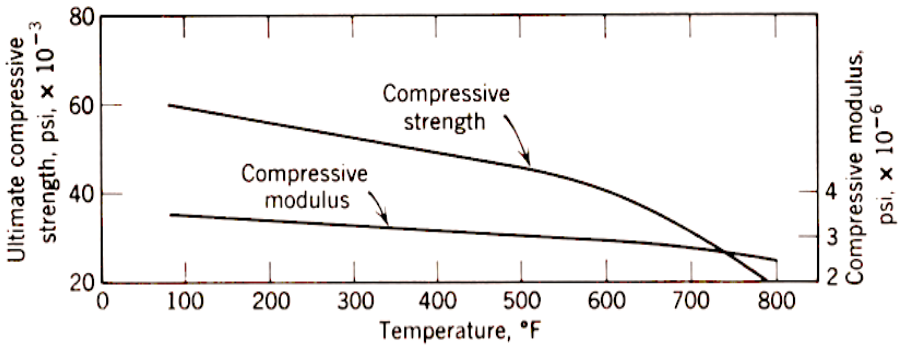

Figure 1.2. Compress strength and modulus of poly (2,2'-m-phenylene-5,5'-bibenzimidazole) as a function of temperature. Figure reprinted from Encyclopedia of Polymer Science and Technology, Levin H.H. Copyright (1999-2014), with permission from John Wiley and Sons[3].

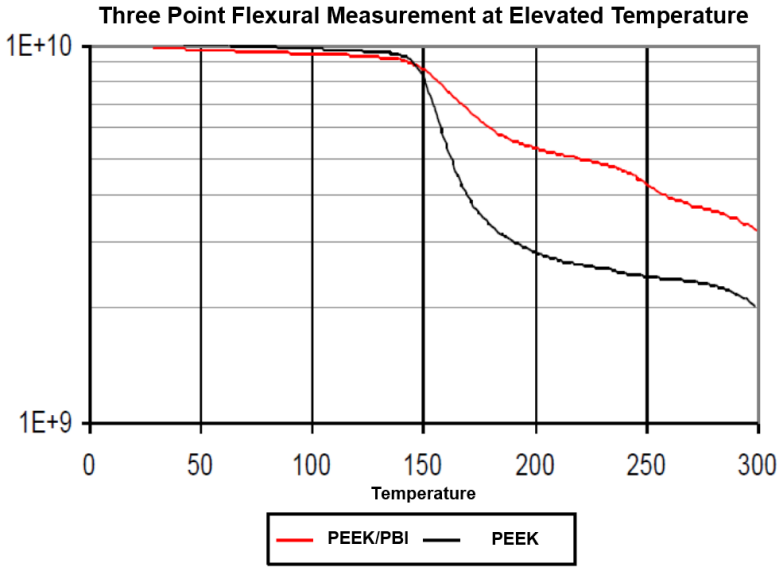

Figure 1.3. The DMA flexural modulus measurement of PEEK/PBI and PEEK at elevated temperature. Figure was adopted from reference [2] with the permission of the author.

1.3 Research objectives and significance

The objective of this dissertation work is to obtain fundamental understanding of the basic physical relationships between microscale structural variables and the macroscale properties of polymer composites. The study focuses on the interface

between the inclusion phase and polymer matrix. We uncovered a number of rather distinct molecular interactions at the interface that strongly influence the properties of the composites. Another aspect of this dissertation work is to illustrate the influence of the spatial dispersion of the inclusion phase on the morphology development, as well as the resultant material properties. The model system PP/CNT provides knowledge of the spatial arrangement of individually dispersed nanoparticles with the crystal and amorphous domains of a polymer matrix. By improving the dispersion process to better manage the interface, we managed to reduce the concentration of CNT necessary to increase the modulus of PP. The dispersion and surface functionalization methods for CNT that we developed are expected to play an important role in the designing of novel polymer/CNT nanocomposite materials.

PEEK/PBI is a composite that is used in a variety of extremely harsh conditions by the oil and gas industry. The primary objective of the PEEK/PBI research is to understand the materials science of this composite in order to develop improved materials with longer lifetimes. After consulting with industry, we chose to study this material by immersing samples in 288 °C hot water under a pressure of 1600 psig.

This study is unique in its focus on two high performance thermoplastics, PEEK and PBI, neither of which have been thoroughly studied individually. Still less is understood about the PEEK/PBI blend, which has been selected by industrial interests for certain applications that aim for the high temperature operating regimes. To our knowledge, this work is the first examination of the hygrothermal-dependent properties

of the PEEK/PBI blend. As such, we hope to provide new and useful information to the scientific community as well as the affiliated industry.

It is expected that the present dissertation work will contribute significantly to the fundamental understanding of the structure-property relationship of polymers containing nano- and micro-domains, including the understanding of the effect of spatial dispersion of nanoparticles and the interface/interphase.

1.4 Layout of the Dissertation

In Chapter II, a brief review is presented regarding structure-property relationships for a polymer matrix containing solid particles. The current issues involved in the development of polypropylene and CNT nanocomposite materials are highlighted. Chapter II also provides a review of the research on the immiscible polymer blends and the mechanism that can promote the affinity between the immiscible components through the formation of secondary bonding. Chapter III investigates microstructural mechanisms responsible for the observed remarkable increase in modulus and strength of polypropylene containing only trace amounts of multi-walled carbon nanotubes (MWCNTs). Chapter IV focuses on gaining fundamental insight into the tensile and fracture behavior of PBI after being subjected to different environmental conditions. The mechanisms that cause the property deterioration of PBI are investigated. The studies conducted in Chapter IV provide the groundwork for fundamental understanding on the effect of PBI as an inclusion phase in the PEEK/PBI blend. Chapter V describes factors governing the interfacial phenomena of a 50:50 weight ratio PEEK and PBI blend. The phase behavior and mechanical properties of melt-blended and subsequently

compression molded PEEK/PBI blends have been investigated. Concluding remarks summarizing the research outcome and considerations for future research efforts are given in Chapter VI. Finally, citation of the references in this dissertation is documented.

CHAPTERII

LITERATURE REVIEW

2.1 Introduction

Many engineering applications require that reinforcing particles be introduced into polymeric materials to enhance their physical and mechanical properties[4]. In real life application of these reinforcing particles, issues such as the tendency of forming aggregation and phase separation between the inclusion phase and polymer matrix impose difficulties for achieving the desired properties[5, 6]. Over the past few decades many new multicomponent polymeric materials have been developed[7]. Incorporation of one or more polymeric or inorganic components into the polymer matrix to form a composite is a common and versatile way to develop new materials with a desirable combination of properties[8, 9]. The design and development of these multicomponent polymeric materials are strongly dependent on two major characteristics, which are the morphology and interface of the inclusion phase and matrix. In general, the term morphology refers to the shape and spatial distribution of the inclusion phase inside the polymer matrix, as well as the resultant microstructure of the multicomponent polymeric material.

Although micron-diameter particles have been used extensively for decades to tailor certain polymer properties, these improvements have traditionally come at a performance cost related to polymer strength, ductility, and processability[10-12]. These critical issues reveal the importance of gaining insights of the mechanisms by which

morphology and microstructure directly influence bulk response in polymer composites and blends.

2.2 Polypropylene and CNT Nanocomposites

Recently, nanometer-diameter filler particles have attracted great attention for their potential use in improving material properties [13]. It is hoped that nanoparticles will not only afford improvements in material performance without reducing other properties, but that they may possibly be used to achieve multifunctional property enhancement, as is seen in high strength, high conductivity carbon nanotubes (CNTs) [14]. Given their immense surface area to volume ratio, nanoparticles are also attractive for use in applications involving energy conversion, gas storage, and barrier properties [15-17].

Although great efforts have been made to integrate nanoparticles into polymeric materials, little progress has been made to understand the direct role of nanoparticles in controlling the physical behavior of the composite. This is largely due to the fact that most dispersion methods fail in establishing a consistent, stable dispersion of well-exfoliated nanoparticles unless there is significant physical or chemical modification to the polymer matrix and/or nanoparticles.

For nanocomposite materials server in structural application, the need to establish reliable predictive model for their large-scale mechanical performance is highly desired. The behavior of the polymer nanocomposite is complicated by several important factors, including: (1) short-range and long-range interactions between nanoparticles, (2) the

polymer/nanoparticle interfacial region, which becomes more significant with decreasing nanoparticle diameter, and (3) a number of intermediate structural parameters which are not easily identified or controlled, including dispersion and nanoparticle geometry. Yet another obstacle to gaining insight into the effects of nanoscale structure on macroscale response involves the difficulty in differentiating between local and non-local behaviors. Since most characterization methods rely on visual analysis of 2D sectioning of 3D networks, they are sensitive to spatial inhomogeneities that may be especially significant given the non-equilibrium character of most polymer nanocomposites.

Our research group has concentrated on the development of fully exfoliated and well-dispersed nanomaterials that are stable in various solvents and can be transferred to a polymer matrix without aggregation[1, 18-20]. This dissertation will present recent results involving α-zirconium phosphate (ZrP) nanoplatelets and multi-walled carbon nanotubes (MWCNTs), and discuss the commercial significance of these findings in the context of engineering applications.

2.3 Individually Dispersion of CNTs into Polypropylene

The individual exfoliation of CNTs is challenging because CNTs are known to rapidly self-assemble into parallel bundles or ropes following synthesis. This is due to strong intertube van der Waals (vdW) interactions and π- stacking. We have developed the first innocuous and robust method for the complete debundling of nanotube aggregates into an individually dispersed state using a colloidal approach based on reversible electrostatic coupling of ZrP nanoplatelets to oxidized CNTs (Figure 2.1). ZrP

nanoplatelets are able to overcome short-range vdW interactions and physically de-bundle the CNTs by localizing sonication energy at tube-tube interfaces. Isolation of individually exfoliated CNTs in solution can be achieved by inducing precipitation of the ZrP nanoplatelets with either acid or salt addition [20, 21]. Current efforts are dedicated to developing structure-property relationships to identify mechanisms associated with individual CNTs and discerning conditions for which bundling may be preferable.

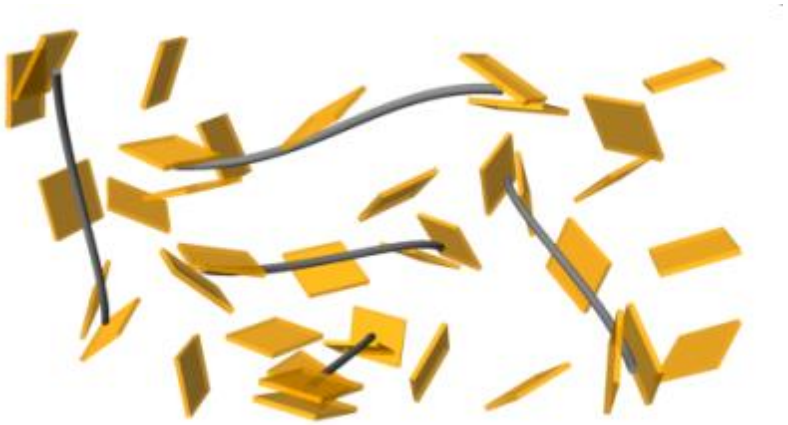

Figure 2.1. Schematic of hybrid structure formed from CNTs electrostatically tethered to ZrP nanoplatelets.Figure reprinted from Chemistry of Materials 22(12) (2010) 3773-3778. Copyright (2010), with permission from American Chemistry Society [22].

Schematic of hybrid structure formed from CNTs electrostatically tethered to ZrP nanoplatelet [22]. Our group has developed several techniques to compatibilize individual MWCNTs with a PP matrix and has reported the electrical conductivity of these PP/MWCNT nanocomposites [18]. Our dispersion approach introduced no damage to the MWCNT structure, and we observed uniform dispersion in PP at relatively high loading (Figure 2.2). It was found that the transition to an electrically conductive

network is related to the well-known geometric percolation, but contact resistance through the matrix phase reduced the conductivity at high MWCNT loading. We have also correlated the notable enhancement in thermal stability at extremely low loading with the free radical quenching ability of the dispersed nanoparticles. Our findings indicate that the onset of conductive behavior cannot simply be defined by electron tunneling between disconnected nanotubes, as was previously determined for the SWCNT thin film networks [21]. Figure 2.2 Disentangled and uniformly dispersed MWCNTs in poly(propylene) at loading of 0.5 wt. %; adapted from[18]. We have recently observed a tremendous increase in the mechanical properties of PP at extremely low CNT loading, which we have attributed to the selective reinforcement of interspherulitic and interlamellar regions by the MWCNTs, which behave as "super"-tie chains [19]. Similar strengthening behavior has been observed for nanoparticle/epoxy composites, for which the nanoparticles interact and delocalize stress concentration [23, 24] . Our study on delamination toughness of a carbon fiber reinforced composite containing a nanocomposite interlayer is among the first reports of successful utilization of nanoparticles to address delamination toughness of a composite structure [24]. The mechanisms of toughening are due to the ability of MWCNTs to interact and shield damage when loosely aggregated. Likewise, the properties of the PP/MWCNT composites discussed earlier are dependent on the unique incorporation of the MWCNTs in the interspherulitic domains in order to elicit a unique response. We have also achieved successful dispersion and full exfoliation of ZrP/MWCNT hybrid nanoparticles in an epoxy matrix [22]. Noteworthy increases in modulus and strength, which could not

be attributed to the behavior of either individual phase, were observed for this hybrid composite. Although both phases contributed to the improved modulus, the ability of the interacting MWCNTs to shield internal defects from growing to a critical size has been implicated as the cause of the marked increase in strength. This hybrid approach yields unique properties that are otherwise not possible and may present a new direction for materials research.

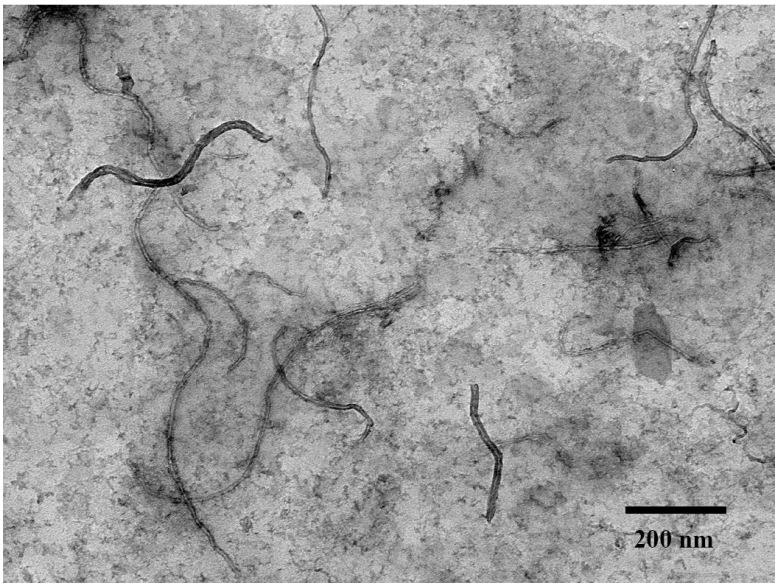

Figure 2.2. Disentangled and uniformly dispersed MWCNTs in polypropylene at loading of 0.5 wt.%. Figure reprinted from Carbon 50(12) (2012) 4711-4721, copyright (2012), with permission from Elsevier [18].

2.4 Polyether ether ketone (PEEK) and Polybenzimidazole (PBI) Blend

Polymer blending provides a versatile approach to develop new materials with the beneficial features of each component [25, 26]. However, the development of new useful blends is significantly limited by the incompatibility of many polymer pairs of interest [27]. The extended Flory-Huggins theory has demonstrated that there are

substantial thermodynamic barriers to obtaining a one-phase polymer blend at a molecular level [28-32]. Most polymers pairs are immiscible at ambient temperatures and form multiphase systems whose bulk properties are governed by the properties of the interfaces between the different phases [33-35]. The interface of incompatible polymer blends tends to exhibit low mechanical strength during large deformation and fracture because of the lack of physical and chemical interaction across the phase boundaries and poor interfacial adhesion [34-37]. As a result, scientific interest in the nature of the interfacial region between immiscible macromolecular phases has intensified. In particular, special attention has been addressed to understand the formation of the interface in binary or multicomponent polymer systems, so that their properties may be better controlled or predicted[38]. A valuable guideline for successful blend technology requires a sound scientific basis. However, understanding the evolution of the interface during a mixing process is extremely difficult because it is necessary to account for factors such as diffusion, phase penetrations and the contribution of forced mixing, etc. This does not only hold for large-scale industrial applications, but also for scientific problems. Nevertheless, theories of polymer-polymer mixing have been created based on semi-empirical results of relatively simple model systems[30, 39, 40]. In particular, these theoretical considerations aim at understanding the main effects, including molecular weight, polydispersity and composition in polymer-polymer thermodynamics.

Several strategies have evolved to overcome the thermal dynamic barrier associated with unfavorable mixing of polymers[41, 42]. The addition of a graft

copolymer or block copolymer as a compatibilizer is a common route to promote the compatibility of blend components. One of the major drawbacks of this approach is that much of the compatibilizing agent does not reside at the interface after processing. It is generally accepted that the free energy of mixing is usually positive for polymer blends due to a small entropic contribution[31, 43]. However, in the past decades, studies have demonstrated that it is possible to have an exothermic process by introducing specific interactions between the components [41, 44-46]. In these cases, intermolecular forces result in a negative enthalpy term. As a result of this, the compatibility between the mixing components is promoted. This concept has been employed to overcome the inherent drawbacks associated with multi-phase composites such as interfacial weaknesses and the presence of defect sites. The resulting materials could have a range of desirable features, for instance improved impact strength and barrier properties.

Poly(ether ether ketone) (PEEK) is a thermoplastic that is used in demanding engineering applications. It is used in various forms (matrix, coating, fiber) for a large variety of areas including energy production, electronics and medical components[47, 48]. Depending on its percentage of crystallinity, the modulus of PEEK drops significantly at temperatures higher than its glass transition temperature (T_g). Applications involving temperatures above its T_g necessitate an inclusion phase that is able to reinforce the PEEK matrix. As a consequence, its operating range can be expanded. Polybenzimidazole is primarily used for high temperature application because it presents a glass transition temperature of 427 °C and retains its mechanical properties up to 400 °C in dry condition [3]. In previous studies, PBI has been used as a component

in polymeric blends [39, 42, 49-51]. In these cases, the enhanced interactions developed between PBI and the other components have been attributed to the formation of hydrogen bonding at the imide of the PBI backbone[42, 49, 50]. In addition, some studies have demonstrated the enhanced miscibility by the presence of single T_g and well defined single tan δ relaxation peaks that are intermediate between those of the pure components[39, 50]. The intermolecular interactions promoted by the presence of hydrogen bonding are considered to play a key role in enhancing the compatibility of these polymer blends. We have hypothesized that a hydrogen bond may form between the N-H group of PBI and the carbonyl group of PEEK. Blending of PEEK and PBI is expected to be an effective route to combine the favorable properties of both polymers for use in harsh environment applications.

An underexplored aspect of this blend system is connected with the tendency of the PBI component to absorb and retain significant amounts of moisture. Because of the amorphous nature of PBI and the presence of N-H groups in its backbone, it is prone to hydrolysis degradation at temperatures above 250 °C [52]. Moisture retention can also cause significant swelling of PBI, which potentially will introduce stress at the PEEK/PBI interface. Their influence on the performance of this type of blend in certain application environments is poorly understood. This dissertation work shall attempt to elucidate the factors governing the interfacial phenomena of a 50:50 weight ratio PEEK and PBI blend. The phase behavior and mechanical properties of melt-blended and subsequently compression molded PEEK/PBI blends have been investigated. In the application where high temperature and high pressure are involved, the associated

mechanical properties need to be specified in detail. It is critically important to gain understanding of the mechanisms that cause the deterioration of stiffness, fracture toughness and strength over prolonged service. This understanding includes the various parameters that are involved in the degradation process, namely time, temperature and the presence of aqueous or acidic environments. In addition, we are particularly interested in the characteristics of the interface between PEEK and PBI when the blend is subjected to various conditions. Achieving this objective requires obtaining quantitative measurements of the adhesion strength of the two components. This is made challenging by the complexity of the current system's composition, which includes semi-crystalline PEEK reinforced with PBI particles and potentially a high water content. The irregular geometry of the PBI particle as well as the small length scale involved are additional obstacles to evaluating the nature of the interface. These difficulties have led to the use of AFM-based quantitative nano-mechanical mapping (QNM) technique to determine the values of properties such as stiffness and elastic modulus. In the intermittent contact mode, the AFM cantilever oscillates in proximity to a surface. The amplitude of the cantilever deflection can be used to determine its conservative and dissipative interactions with the surface. These parameters can be correlated to the viscoelastic response of the examined material if correctly interpreted. Compared to the conventional phase and force modulation imaging technique such as nano-indentation, the AFM-based QNM is able to acquire the elastic modulus of a sample surface with high spatial resolution without compromising the data acquisition speed. Dokukin and Sokolov's study demonstrated the moduli obtained from QNM are

comparable to the data measured with the other commonly used techniques, for instance the nano-indentation and dynamic mechanical analysis (DMA) [53]. Although measurements taken by QNM for soft materials tend to overestimate values due to the excessive stress induced by a sharp tip, no such discrepancy is observed for more rigid materials. Therefore, we expect this method to be suitable for assessing the characteristics of the interface for our present study.

CHAPTER III

INFLUENCE OF TRACE AMOUNT OF WELL-DISPERSED CARBON NANOTUBES ON STRUCTURAL DEVELOPMENT AND TENSILE PROPERTIES OF POLYPROPYLENE[*]

3.1 Introduction

Carbon nanotubes (CNTs) are a class of high aspect ratio, multi-functional nanomaterials that have been extensively investigated as filler materials to enhance the physical and mechanical properties of polymers. In order to effectively modify the performance of a polymer with low CNT loading, the individual nanofillers must be well dispersed, which increases the interfacial area between the CNTs and polymer matrix . In non-polar, commodity polymers, such as polyethylene (PE) and polypropylene (PP), compatibility is an additional concern because of the lack of interaction between the CNTs and polymer matrix.

For commercial applications, dispersion by mechanical shearing in the melt is preferable to achieve high volume production, but generally fails to provide good dispersion even at optical resolution scale. Extreme shearing conditions are often required to disrupt large aggregates, but significantly reduce the length and damage the CNTs, and may degrade the polymer matrix [54-56]. Chemical surface modification

[*] This chapter is reprinted from *Macromolecules*, **2013**, *46* (2), pp 463–473, Peng Liu, Kevin L. White, Hiroaki Sugiyama, Jiang Xi, Takeshi Higuchi, Taiki Hoshino, Ryohei Ishige, Hiroshi Jinnai, Atsushi Takahara, and Hung-Jue Sue.

may be used to improve the dispersion state and compatibility of the CNTs prior to mixing, which reduces the mechanical energy required during melt processing. However, achieving excellent dispersion usually requires extensive chemical treatment that may significantly modify the CNT properties and reduce aspect ratio [54, 56-58]. These challenges are a consequence of the enormous length-dependent interaction potential between CNTs [59], and are responsible for the current lack of fundamental knowledge and broad disagreement regarding how CNTs influence polymer properties [60].

PE and PP make up the vast majority of worldwide polymer production because they are inexpensive, easily processable, and highly versatile. There has been substantial interest in developing PP/CNT composites with enhanced performance at sufficiently low loading to retain these advantageous properties. It is well-established that CNTs are effective α-form crystal nucleating agents for PP, and significantly reduce spherulite size, enhance crystallization kinetics, and increase crystallization temperature [55, 61-64]. However, there is generally no significant change in degree of crystallinity, crystal structure, or dynamic mechanical relaxation behavior [64-69]. Despite promising reports that have shown CNTs can significantly improve dimensional stability, reduce cycle time, decrease combustion heat release rate, and improve thermal stability [18, 64, 70-74], the ability of CNTs to enhance mechanical properties has been limited. To effectively utilize and identify the contribution of CNTs in reinforcing semi-crystalline thermoplastics, scalable processing approaches to disentangle and stabilize the CNTs before and after mixing in the polymer matrix are needed.

In this work, we correlate the tensile behavior of a commercial PP containing multi-walled carbon nanotubes (MWCNTs) with the microstructure of the system across broad length scales. Excellent dispersion and compatibilization were achieved using our well-established nanoplatelet-assisted dispersion approach [1, 20, 21], followed by subsequent reaction with octadecylamine (ODA) [18], which is a long-chain fatty amine functional group well known to be miscible with PP. This unique processing method takes advantage of the reversible electrostatic interaction between exfoliated α-zirconium phosphate (ZrP) nanoplatelets, which have a positive surface charge, and lightly oxidized CNTs. During ultrasonication, the high aspect ratio ZrP nanoplatelets focus mechanical energy within CNT aggregates and promote their individual dispersion in aqueous solven [1, 20, 21]. The concentration of energy across the surface of the CNTs prevents significant stretching or bending of the nanotubes during sonication that would otherwise result in the rupture and scission of long CNTs [57, 58]. The ZrP nanoplatelets may be subsequently removed from solution by the introduction of an acid to disrupt the electrostatic interaction between the ZrP and CNT phases [20, 21]. We have recently reported that this method results in high yield (> 95%) of individually dispersed single-walled carbon nanotubes (SWCNTs) and MWCNTs in aqueous solution, while completely removing any detectable trace of the ZrP nanoplatelets [1, 20].

In our previous work, we showed that after reacting with ODA, the recovered functionalized MWCNTs (F-MWCNTs) are stable in PP and remain well dispersed at up to 2 wt.% loading in compression-molded samples [75]. The disentanglement process is

extremely beneficial for properties related to the surface area of the F-MWCNTs, such as thermo-oxidative stability, the onset of electrically conductive behavior, and PP crystallite nucleation. In this work, we report remarkable improvements in the mechanical properties of injection-molded PP containing only 0.1 wt.% F-MWCNTs. The structure of the PP/F-MWCNT nanocomposites is investigated across several length scales in order to elucidate the microstructural mechanisms responsible for the observed behavior. The implications of the present findings for engineering applications of nanoparticle-filled polymers are discussed.

3.2 Experimental

3.2.1 Materials

Pristine MWCNTs (P-MWCNTs) (purity > 90%, average outer diameter of 10-12 nm, and length of 0.1-10 um) and ODA ($CH_3(CH_2)_{17}NH_2$, 97%) were purchased from Sigma-Aldrich. The P-MWCNTs were purified by mild oxidation and disentangled with exfoliated ZrP nanoplatelets using our established nanoplatelet-assisted dispersion approach [76-78]. The ZrP nanoplatelets were synthesized with length and width of 100 μm and exfoliated to an individual layer thickness of 0.7 nm using tetra(*n*-butylammonium hydroxide) (Sigma-Aldrich, 1 mol L^{-1} in methanol), which has been previously reported in detail [79-81]. The disentangled MWCNTs were isolated from solution by the addition of acid to coagulate and precipitate the ZrP nanoplatelets [20, 21]. The disentangled MWCNTs were functionalized with ODA prior to mixing with PP according to our recently reported method [75]. The MWCNTs become hydrophobic

after reacting with ODA and precipitate from aqueous solution. The recovered F-MWCNTs were thoroughly washed and dried in an oven overnight at 80°C.

3.2.2 Preparation of PP/MWCNT composites

The F-MWCNTs were added to xylene and sonicated for 1 hr at room temperature. PP pellets were added to the F-MWCNT/xylene solution and stirred for 1 hr at 125°C to obtain a masterbatch with 2 wt.% F-MWCNT. Ethanol was added to precipitate the PP/F-MWCNT from solution. The recovered powder was washed several times and dried under vacuum overnight at 80°C. The PP/F-MWCNT masterbatch was compounded with PP to concentrations of 0.1 and 0.6 wt.% using a System 40 Haake mixer at 60 RPM and 180°C for 2 min. For comparison, PP/P-MWCNT (0.1 wt.%) and PP/ODA (0.5 wt.%) systems were prepared using the same processing conditions. Specimens were manufactured with a CS-183 MMX mini injection molder at fixed melt and mold temperatures of 195°C and 90°C, respectively, with injection rate of 0.25 cm^3/s. The molded samples were slowly cooled to room temperature.

3.2.3 Characterization

Samples for transmission electron microscopy (TEM) and transmission electron microtomography (TEMT) were prepared using a diamond knife to face-off trimmed block specimens from the core region prior to staining. The faced-off block was exposed to vapor from an aqueous solution containing 0.5 wt.% RuO_4 for 12 hours. Ultra-thin sections were prepared using a Reichert-Jung Ultracut E microtome with diamond knife at cryogenic temperature. TEM specimens were prepared with thickness

of 60-80 nm. Thin sections were placed on a 300-mesh Formvar-coated copper grid and examined using a JEOL 1200 EX TEM operating at an accelerating voltage of 100 kV. For TEMT, thin sections of PP/F-MWCNT (0.1 wt.%) were prepared with thickness of about 150 nm. A JEOL JEM-2200FS computerized TEM operating at an accelerating voltage of 200 kV was used to record a series of 135 projections along a single tilt axis at tilt angles ranging from -67° to 66° with an angular interval of 1°. The images were aligned using Au colloidal beads deposited on the thin section surface. The positions of 14 Au nanoparticles were tracked throughout the series of tilted images[82, 83]. The images were acquired at resolution of 0.36 nm/pixel. The maximum calculated deviation between the aligned images was ± 0.8 pixel.

Optical microscopy (OM) specimens of injection-molded PP nanocomposites with dimensions of 5 x 5 x 2.5 mm^3 were cut from the core region and polished. The specimens were etched with an oxidizing solution containing 3 wt.% potassium permanganate in mixed solvent of sulfuric acid and phosphoric acid to preferentially attack the amorphous regions of the polymer [84]. Specimens were examined using an Olympus BX60 OM under bright field conditions in reflectance mode.

X-ray diffraction specimens were cut from the core region of injection-molded samples with dimensions of 5 x 5 x 2.5 mm^3. The incident X-ray beam was perpendicular to the molding direction for both wide-angle X-ray diffraction (WAXD) and small-angle X-ray scattering (SAXS) measurements. WAXD experiments were performed with a Bruker-AXS D8 diffractometer with CuK_α radiation (wavelength, λ =

0.154 nm) operating at 40 kV and 50 mA. Specimens were placed inside an aluminum sample holder and scanned at room temperature over diffraction angle, 2θ, from 2° to 70° with step size of 0.03°. The WAXD results were normalized relative to the total scattering intensity of each specimen. SAXS measurements were performed at room temperature using a synchrotron X-ray radiation source (BL40-B2 beamline, $\lambda = 0.1$ nm) at the SPring-8 synchrotron research facility in Hyogo Prefecture, Japan. Scattered X-rays were detected using a 3000 × 3000 pixel imaging plate over a scattering vector range of 0.05 $nm^{-1} < q < 4$ nm^{-1}. The scattering vector, $q = 4\pi(\sin\theta)/\lambda$, was calibrated based on the average of 3 peaks of silver behenate with a sample-to-detector distance of 2.2 m. All SAXS measurements were corrected for intensity fluctuations in the main beam and sample absorption. The scattering intensity was corrected to account for background scattering.

Dynamic mechanical behavior was investigated using an ARES-G2 rheometer (TA instruments) in torsional mode. The strain amplitude was 0.01%, which was verified to be within the linear viscoelastic region of all samples at -20°C. The temperature was ramped at a constant rate of 3°C/min from -20 to 150°C at fixed frequency of 1 Hz. The glass transition temperature, T_g, was assigned to the temperature associated with the first maximum in $\tan\delta = G''/G'$, where G'' and G' are the loss and storage moduli, respectively.

Tensile tests were carried out in accordance with ASTM D638-08. Room temperature tensile tests were performed on an MTS screw-driven test machine with

crosshead speed of 5 mm/min. True strain was measured using a calibrated MTS contact extensometer, model 632 12B-50, and was verified with a MTS LX1500 laser extensometer. The initial gauge length of the tensile specimens was 25.4 mm. The reported standard deviation in elastic modulus, E, and tensile yield strength, σ_y, are based on at least five specimens.

3.3 Results

3.3.1 Dispersion and microstructure

The dispersion of F-MWCNTs and crystalline morphology of PP in the injection-molded composites were investigated with TEM. The micrographs clearly show that the disentangled F-MWCNTs remain individually dispersed after molding (Figure 3.1). At 0.1 wt.% loading, the injection-molded F-MWCNTs appear to be highly extended and oriented in the molding direction. The microstructure of the PP/F-MWCNT (0.6 wt.%) consists of much closer spaced MWCNTs that are similarly extended and preferentially oriented in the flow direction. In our previous report on compression-molded samples, the uniformly dispersed F-MWCNTs are randomly oriented and partially coiled in the PP matrix [18]. This suggests that the shearing forces during molding conditions are responsible for the orientation and conformation of the F-MWCNTs. Although it is difficult to precisely determine the dispersion using TEM, the dispersion quality of the 0.6 wt.% F-MWCNT system appears to be reduced compared to the dispersion at lower loading. The spherical, black inclusions in the image are attributed to catalyst-induced phase separated domains of the ruthenium heavy metal from the staining solution.

Elemental analysis confirmed the presence of iron and ruthenium heavy metal species in the spherical aggregates.

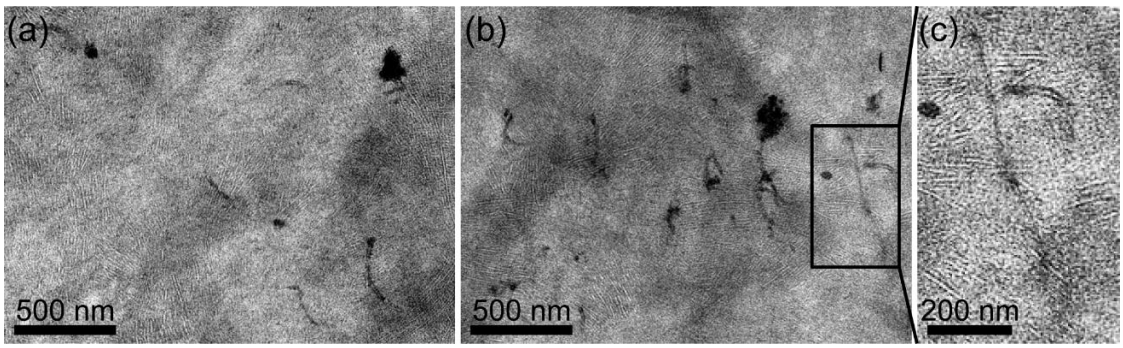

Figure 3.1. TEM images of stained PP/F-MWCNT nanocomposites demonstrating homogeneous dispersion of the MWCNTs. (a) PP/F-MWCNT (0.1wt.%); (b) PP/F-MWCNT (0.6wt.%); (c) higher magnification of (b) showing detail of lamellae structure and oriented F-MWCNT. Flow direction is from bottom to the top of the images.

After extensive TEM analysis, we concluded that in the vicinity of the F-MWCNTs, the PP lamellae are predominantly oriented perpendicular to the F-MWCNT axis (Figure 3.1c). The highly ordered interface extends along the entire F-MWCNT length, which is consistent with previous reports on CNT-induced transcrystallinity in PP [68, 85, 86]. The total diameter of the transcrystalline regions appears to be relatively small and localized near the CNTs. It is important to note that conventional 2D TEM provides only limited information regarding the PP/CNT interface because the spatial association among the observed structural features is not clear. The influence of the F-MWCNTs on the 3D morphology of the PP matrix was elucidated with TEMT. A series of micrographs were obtained over a broad range of tilting angles, and were subsequently aligned using Au nanoparticles deposited on the surface. This technique has previously been applied to study the complex morphology of various systems

including block copolymers [87-90] and polymer nanocomposites [83, 91-93], although we are unaware of any previous TEMT investigations on a CNT-filled polymer. The calculated error in image alignment is less than the resolution of the images.

A series of TEMT slices through the thickness of the PP/F-MWCNT (0.1 wt.%) sample is shown in Figure 3.2. The images are centered on a single horizontally oriented F-MWCNT, and the PP crystalline lamella appear vertically oriented. The image progression corresponds to an incremental slicing through the thickness of the TEMT specimen (*z*-axis). The individual images represent 0.36 nm thick projections, and each sequential image in Figure 3.2 is separated by 3.6 nm along the *z*-axis. The observed PP lamellae are therefore positioned less than 0.36 nm from the F-MWCNTs, which verifies that the features are spatially associated. The F-MWCNT and well-defined PP lamellae in Figure 3.2d and Figure 3.2g are lightly shaded to improve clarity. An accompanying high-resolution TEMT video showing the detailed microstructure and interaction between the F-MWCNT and PP lamellae at lower magnification is provided.

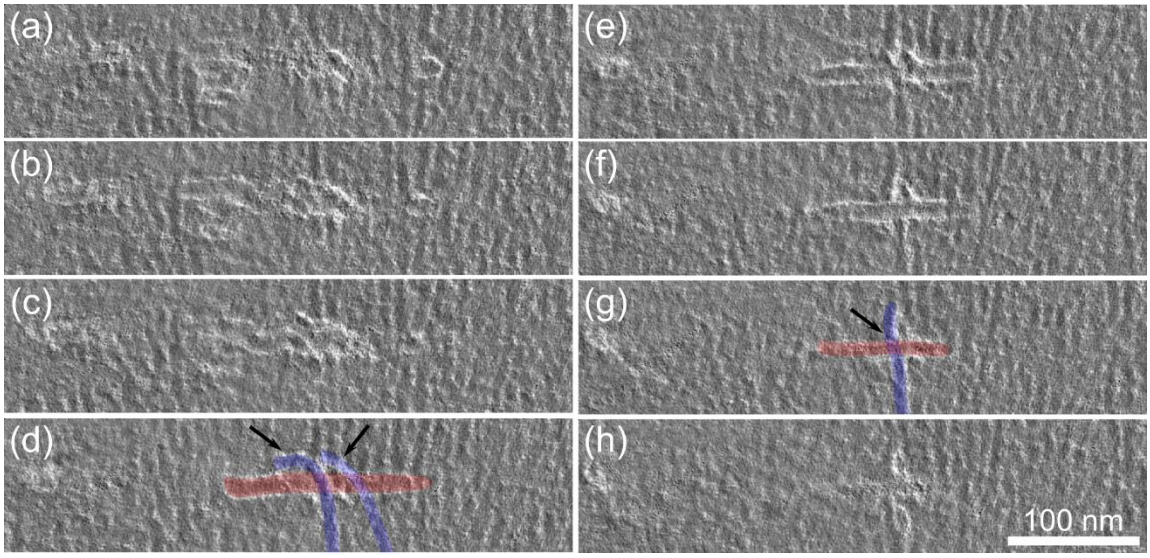

Figure 3.2. Sequence of TEMT slices of PP/F-MWCNT (0.1 wt.%) nanocomposite obtained from serial tilt projections. Each image represents a 0.36 nm slice through the thickness of the sample. Sequential images are separated by 3.6 nm along the *z*-axis. A single horizontally oriented MWCNT is centered in each image. The PP lamellae are oriented perpendicular to the long axis of the F-MWCNT are aligned vertically.

The F-MWCNT shown in Figure 3.2 is about 500 nm long, but appears shorter because of the narrow depth of field for the individual images. The position of the F-MWCNT also appears to shift throughout the image series due to its waviness in the *z*-direction. The position of the lamellae shifts with the F-MWCNTs, which indicates that the orientation of the PP lamellae follows the curvature of the nanotubes at the interface, and confirms that the lamellae extend radially from the F-MWCNT surface as extended, 2D stacks. In Figure 3.2d, two black arrows highlight a pair of PP lamellae, shaded blue, that are clearly positioned above the surface of the F-MWCNT, which is shaded red. The image in Figure 3.2g is 10.8 nm below the image in Figure 2d along the thickness direction, and shows the same lamellae positioned beneath the F-MWCNT. These images conclusively demonstrate that the F-MWCNT is intermingled with the crystalline

lamellae, as well as the amorphous layers that inter-connect the lamellae stacks. Further work is being pursued to generate volume-rendered 3D images to better elucidate the global morphological features of this system.

The bulk crystal structure of the PP nanocomposites was investigated using OM and is shown in Figure 3.3. The neat PP exhibits a characteristic spherulitic structure with clearly defined boundaries and average diameter on the order of 30 μm (Figure 3.3a). In the PP/F-MWCNT (0.1 wt.%) (Figure 3.3b) and PP/F-MWCNT (0.6 wt.%) (Figure 3.3c) systems, the individual spherulites are no longer clearly visible, which is attributed to extensive heterogeneous nucleation of PP crystallites from the well-dispersed F-MWCNTs. Both systems exhibit highly uniform microstructure and show no evidence of macroscopic clustering or aggregation. In contrast, the crystalline morphology of the PP/P-MWCNT system (Figure 3.3d) consists of visible MWCNT agglomerates that appear to be preferentially localized at grain boundaries between spherulites. Specimens containing 0.5 wt.% ODA exhibit spherulitic morphology similar to the neat PP, with spherulite diameter increased to 50 – 60 μm. This behavior is characteristic of a miscible functional group, which we previously observed from differential scanning calorimetry (DSC) measurements of compression-molded samples [75].

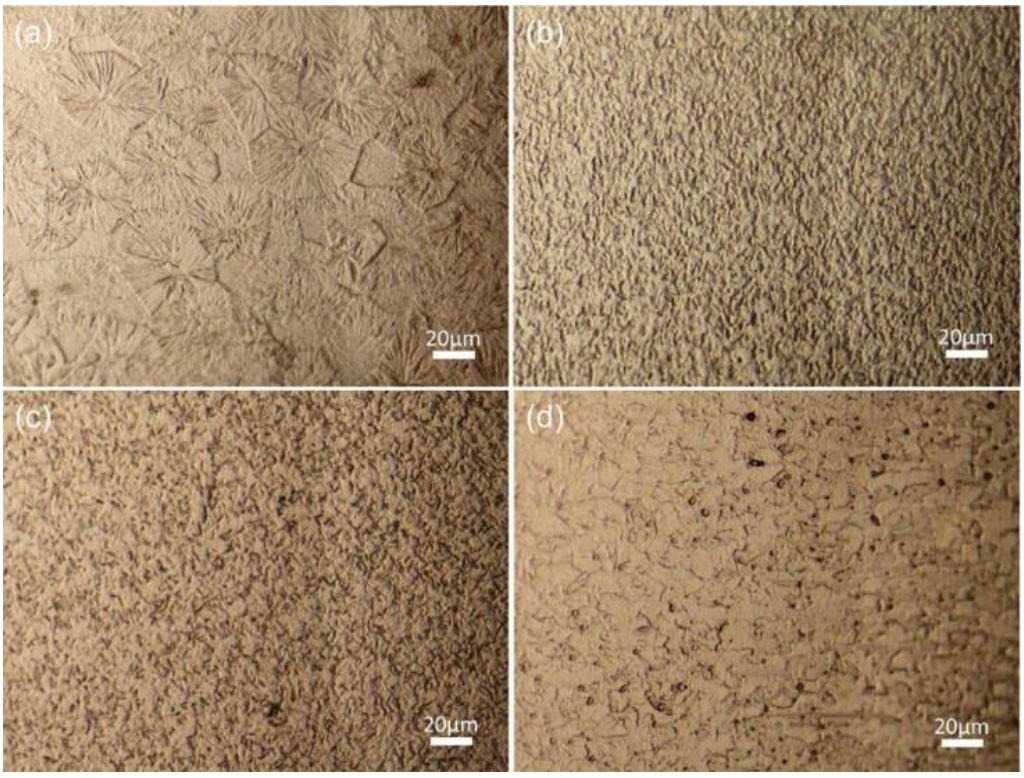

Figure 3.3. Optical micrograph of PP composites taken from the core region of injection-molded specimens after permanganic acid etching. (a) Neat PP, (b) PP/F-MWCNT (0.1 wt.%), (c) PP/F-MWCNT (0.6 wt.%), and (d) PP/P-MWCNT (0.1 wt.%).

3.3.2 Crystal structure

The WAXD patterns are shown in Figure 3.4 and several relevant structural parameters are summarized in Table 3.1. Isotactic PP is polymorphic and may crystallize into monoclinic α-form, trigonal β-form, or orthorhombic γ-form crystallites, depending on processing conditions, isotacticity, and the presence of nucleating agents . The monoclinic α-form crystal is most common, and is responsible for the diffraction peaks measured at 14.1°, 16.9°, 18.5°, and 21.2°, which are indexed to reflections on the (110), (040), (130), and (111) lattice planes, respectively. The diffraction peak at 21.8° is attributed to α-form crystal reflections on the (-131) and (041) lattice planes [94],[48].

The diffraction peak at 25.5° is due to reflections on both the (060) lattice plane of the α-form crystal and the (002) graphitic plane of the MWCNTs [95]. The diffraction peak at 16.1° is due to reflections on the (300) lattice plane of the β-form crystal [50]. Diffraction associated with the γ-form crystal is typically observed as sharp peaks near 15.0° and 20.2°, and were not present in this work. The position of the diffraction peaks for all injection-molded samples varied by less than the step size of the WAXD experiment, and are consistent with the well-established reciprocal spacing of lattice planes in isotactic PP [94]. This indicates that there is no conformational disorder or change in d-spacing of the PP crystal unit cell due to the presence of the MWCNT or ODA.

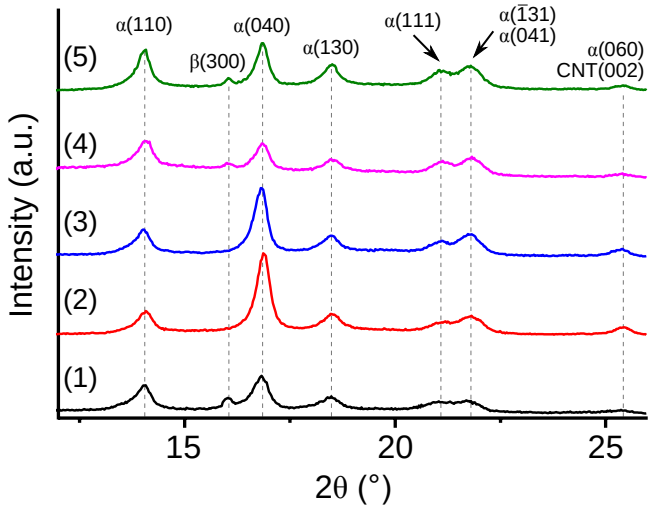

Figure 3.4. WAXD patterns of injection-molded PP composite materials. (1) neat PP, (2) PP/F-MWCNT (0.1 wt.%), (3) PP/F-MWCNT (0.5 wt.%), (4) PP/P-MWCNT (0.1 wt.%), and (5) PP/ODA (0.5 wt.%).

Table 3.1. Summary of crystal structure parameters from WAXD investigation for injection-molded PP nanocomposites. *K* is empirical factor describing percentage of β-form crystals contained within the total crystal content of the PP matrix, calculated from Eqn. 1; $I_{(110)}/I_{(040)}$ is ratio of relative intensity of reflections on (110) and (040) lattice planes; FWHM is full-width at half maximum for reflection on specified planes.

	K (%)	$I_{(110)}/I_{(040)}$	FWHM (°)	
			(110)	(040)
Neat PP	14.6±2.3	0.87	0.56±0.02	0.56±0.02
0.1 wt.% F-MWCNT	0	0.33	0.38±0.01	0.36±0.02
0.6 wt.% F-MWCNT	0	0.43	0.42±0.01	0.36±0.01
0.1 wt.% P-MWCNT	15.3±0.5	1.03	0.52±0.02	0.53±0.02
0.5 wt.% ODA	11.5±1.9	1.15	0.51±0.02	0.44±0.02

The relative amount of β-form crystals within the total crystal content of the PP was estimated by the semi-quantitative factor *K* introduced by Turner-Jones et al. [94]. The value is a ratio of the integral intensities of crystalline reflections associated with the α-form and β-form crystal phases, and is given by the expression: $K = I_\beta/(I_{\alpha1}+ I_{\alpha2}+ I_{\alpha3})$ (1) where I_β is the intensity of the (300) reflection of the β-form crystal, and $I_{\alpha1}$, $I_{\alpha2}$, and $I_{\alpha3}$, are the intensities of the (110), (040), and (130) reflections of the α-form crystal, respectively. The neat PP in this work contains 14.6 ± 2.3% β-form crystallites, estimated from Eqn. 1. In systems containing 0.1 wt.% and 0.6 wt.% F-MWCNTs, there is a complete absence of β-form crystals, which confirms the well-known α-crystal

nucleating effect of CNTs in PP [65, 66]. The PP/P-MWCNT (0.1 wt.%) and PP/ODA (0.5 wt.%) systems do not show a significant change in *K* relative to the neat PP. In the PP/P-MWCNT system, the residual β-form crystal fraction is attributed to the decreased surface area of the poorly dispersed P-MWCNTs compared to the F-MWCNTs at the same loading, which limits the extent of heterogeneous nucleation. This indicates that if good dispersion can be achieved without decreasing aspect ratio, less than 0.1 wt.% MWCNT is sufficient to modify the global crystal structure of PP.

The relative size, distribution, and orientation of PP crystallites was inferred from the height and breadth of reflections on the (110) and (040) planes, which are the primary reflections of α-form PP [96]. Both PP/F-MWCNT systems show a substantial increase in (040) intensity, $I_{(040)}$, and a negligible change in (110) intensity, $I_{(110)}$, compared to the neat PP, and show a significant decrease in diffraction width on both lattice planes. The decrease in $I_{(110)}/I_{(040)}$ indicates that at 0.1 wt.% F-MWCNT loading, there is preferential crystal growth normal to the (040) lattice plane or, equivalently, growth normal to the (110) plane is restricted [97, 98]. The decrease in diffraction width suggests that the crystallite size and perfection along both primary lattice planes is increased. At higher loading of 0.6 wt.% F-MWCNT, there is no further change in crystallite structure, although the slight increase in $I_{(110)}/I_{(040)}$ and diffraction width on the (110) plane may indicate a decrease in dispersion quality.

The PP/P-MWCNT (0.1 wt.%) system exhibits essentially identical diffraction intensity and peak width on both primary lattice planes as the neat PP. In the PP/ODA

(0.5 wt.%) system, the intensities of both primary reflections are increased, and the diffraction width on the (040) lattice plane is decreases slightly, which suggests some increase crystal perfection and size. The increase in $I_{(110)}/I_{(040)}$ indicates that the presence of ODA favors crystal growth along the a*-axis [96], which shows that the ODA functional group is not responsible for the observed change in crystal structure in the PP/F-MWCNT systems. WAXD profiles of compression-molded systems were also obtained, but revealed no significant change in crystal structure between the systems. The observed differences in WAXD patterns for the injection-molded samples are therefore attributed to the alignment and extension of the MWCNTs during molding, and the corresponding change in PP crystal orientation and growth behavior.

The diffraction intensity at 25.5°, normalized relative to the dominant (110) reflection of the PP matrix, is not significantly affected by the introduction of 0.1 wt.% P-MWCNT or 0.5 wt.% ODA, but increases by a factor of 3.2 and 3.8 in PP composites containing 0.1 wt.% and 0.6 wt.% F-MWCNT, respectively. This is significantly greater than the observed increase in $I_{(040)}$, which suggests that the increased intensity at 25.5° is primarily due to the (002) graphite reflection of F-MWCNTs aligned in the molding direction. At 0.6 wt.% F-MWCNT loading, although $I_{(110)}/I_{(040)}$ decreases, the relative intensity of the diffraction peak at 25.5° increases, which is consistent with an increased number of (002) graphitic lattice planes due to MWCNTs aligned in the molding direction.

OM and WAXD investigations revealed that the long-range and atomic-scale features of the PP crystal microstructure, respectively, are significantly modified by the addition of F-MWCNTs. SAXS is sensitive to the intermediate-range repeat unit structure of PP and was measured through the thickness of the injection-molded samples using synchrotron radiation. The 2D SAXS pattern of the neat PP shows isotropic scattering characteristic of a population of spherically symmetric assemblies containing stacked lamellar structure with regular crystalline-amorphous microstructure. Both PP/F-MWCNT systems exhibit similar symmetry, which indicates that the preferential crystallite orientation observed with WAXD does not result in anisotropy over longer length scales.

The azimuthally averaged SAXS patterns are shown in Figure 3.5. The first maxima, q_1, is related to the alternating crystalline-amorphous microstructure of the PP lamellae, and can be used to calculate the long period, L, using Bragg's law, where $L = 2\pi/q_1$. The long period is the average sum of the crystalline lamellae thickness and the thickness of amorphous regions between crystallites, and was determined from the Lorentz-corrected intensity profile to account for the random distribution of lamellae orientations in reciprocal space. The long period of the neat PP is $L^{LC} = 15.47$ nm. The addition of 0.1 wt.% F-MWCNT causes a negligible change in L^{LC}, and at higher loading of 0.6 wt.% F-MWCNT, L^{LC} increases to 16.72 nm. Increasing long period with CNT loading has been previously reported and attributed to an increase in lamellae thickness [99]. However, we were unable to find sufficient TEM evidence to support this claim, and observed no change in degree of crystallinity from either WAXD or DSC

measurements to suggest a change in crystalline fraction (not shown). It is more likely that the increase in long period is due to scattering from the MWCNT phase. The MWCNTs used in this work have inner diameter of ~ 5-6 nm, which should increase scattering intensity for q < 1/R = 0.3-0.4 nm^{-1}. This is in excellent agreement with results for the PP/F-MWCNT (0.1 wt.%) system, which show no significant deviation in intensity from the neat PP until about 0.35 nm^{-1}. The scattering intensity of the PP/F-MWCNT (0.6 wt.%) is increased over all values of *q*, which is attributed to scattering between more closely spaced F-MWCNTs.

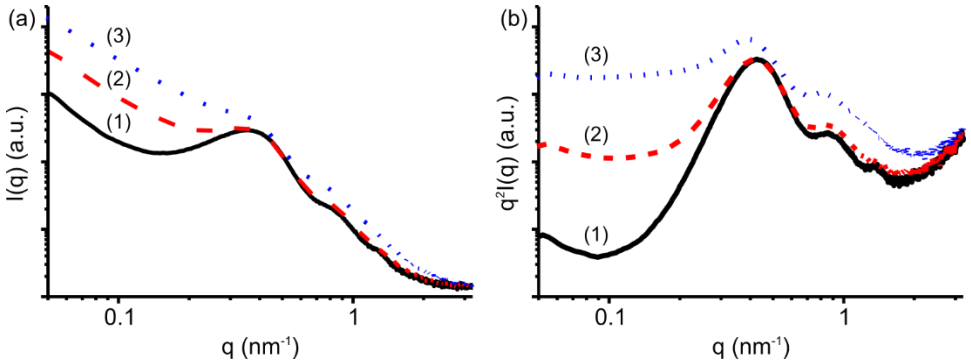

Figure 3.5. SAXS profiles of (1) neat PP, (2) PP/F-MWCNT (0.1 wt.%), and (3) PP/F-MWCNT (0.6 wt.%) systems. (a) Intensity, I(q), versus scattering vector, q, and (b) Lorentz-corrected intensity, q2I(q), versus q.

For the neat PP, additional scattering maxima are clearly defined at higher *q*, and show a nearly integer relationship with q_1: $q_2/q_1 = 1.96$ and $q_3/q_1 = 3.10$. This integer ratio between maxima is characteristic of a periodic lamellae microdomain structure [100]. The ratio between q_2 and q_1 is not affected by F-MWCNT loading: $q_2/q_1 = 2.00$ and 2.01 for the PP/F-MWCNT (0.1 wt.%) and PP/F-MWCNT (0.6 wt.%) systems, respectively. The third maxima, q_3, does not change with 0.1 wt.% F-MWCNT loading,

but could not be discerned at 0.6 wt.% F-MWCNT loading, which is attributed to the increased background scattering at high q. Based on the SAXS measurements, it is apparent that the F-MWCNTs do not significantly modify the intermediate-range microdomain structure of the PP matrix.

The 3D microstructure of the isotropic composite systems was further probed using the 1D correlation function, γ_1. (Details on the calculation can be found in our previous work on SAXS of oriented poly(ethylene terephthalate) [101]. The long period, L^{SC}, was calculated from the second maxima in the correlation curve based on the self-correlation triangle method described by Strobl and Schneider [102]. The intercept of the initial portion of the correlation curve and the horizontal tangent of the first minima provide an estimate of the thickness of one phase, L_1. Assuming a simple 2-phase model with sharp interfaces between crystalline and amorphous domains, the thickness of the second phase may be calculated from the expression $L_2 = L^{SC} - L_1$, and was found to slightly increase with F-MWCNT loading. Based on TEM evidence, L_2 is the lamellae thickness, which indicates that L_1 is the thickness of amorphous regions between lamellae. A summary of the lamellae and interlamellar thicknesses determined from SAXS measurements is provided in Table 3.2. The 1D correlation function shows a significant decrease in the depth of the primary minimum and height of the maximum with increasing F-MWCNT content. This may indicate diminished packing efficiency in the crystalline regions at 0.6 wt.% F-MWCNT loading, which also decreases interlamellar spacing, L_1, to maintain constant degree of crystallinity. At 0.1 wt.% F-MWCNT loading, there is no significant change in thickness measurements from the

neat PP, which supports our claim that the F-MWCNTs are extremely well integrated with the lamellar structure. However, due to the similarity in dimensions of the PP lamellae thickness and the MWCNT diameter, further work is necessary to substantiate this interpretation.

Table 3.2. Summary of SAXS measurements of injection-molded PP composites. L^{LC} is long period determined from Lorentz-corrected SAXS profile; L^{SC} is long period determined from second maxima in the 1D correlation function, γ_1; L_1 is the thickness of amorphous domains between lamellae; L_2 is the lamellar thickness.

	L^{LC}	L^{SC}	L_1	L_2
	[nm]	[nm]	[nm]	[nm]
Neat PP	15.47	14.82	3.1	11.7
0.1 wt.% F-MWCNT	15.51	14.85	3.0	11.9
0.6 wt.% F-MWCNT	16.72	15.75	2.7	13.1

3.3.3 Dynamic mechanical analysis

The DMA curves of the injection-molded PP composites are shown in Figure 3.6. For clarity, only the neat PP and PP/F-MWCNT systems are shown. The storage modulus of the neat PP exhibits a relatively narrow plateau region approaching T_g = 6.6°C, followed by a progressive decrease with temperature due to cooperative relaxation within amorphous domains. The loss factor, tan δ, is a measure of the damping ability of a material, and provides a sensitive measure of molecular-scale

motion and relaxation in semi-crystalline polymers. Slightly above the low temperature maxima in tan δ corresponding to T_g, there is a broad mechanical relaxation extending from 55 - 125°C, with peak at T_α = 91.6°C. The higher temperature α-relaxation peak of isotactic PP is generally attributed to damping within the crystalline lamellae [103, 104]. Approaching 150°C, the rapid decrease in storage modulus and corresponding increase in mechanical damping are due to the onset of crystalline melting.

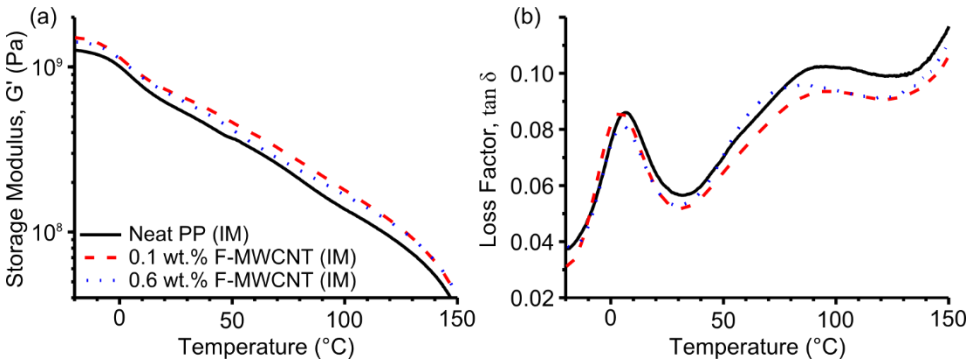

Figure 3.6. DMA measurements of injection-molded PP composite systems. (a) Storage modulus and (b) loss factor, tan δ, obtained from isochronal measurements at frequency of 1 Hz and ramp rate of 3°C/min in torsion.

The PP/F-MWCNT (0.1 wt.%) system exhibits the highest storage modulus throughout the observed temperature range, and shows maximum reinforcing efficiency relative to the neat PP at 95°C, where G' is increased by about 30%. Increasing F-MWCNT loading to 0.6 wt.% does not further improve storage modulus below T_g, and decreases G' throughout the broad α-relaxation transition at higher temperatures. The storage modulus of PP is not significantly changed with the addition of either 0.1 wt.% P-MWCNT or 0.5 wt.% ODA.

Both PP/F-MWCNT systems exhibit a slight decrease in T_g, which is consistent with measurements on decreasing β-crystal content reported by Jacoby et al. [103] and Crissman [105]. The onset of the higher-temperature crystalline relaxation does not vary significantly between the different systems, although the slope of tan δ is significantly increased in the PP containing F-MWCNT (0.6 wt.%) and P-MWCNT (0.1 wt.%). This is attributed to a greater concentration of defects and disorder within the crystalline structure. For the PP/F-MWCNT (0.1 wt.%) system, the peak temperature of the α-relaxation is slightly increased and the peak intensity is decreased, which is anticipated for higher α-crystal content [103]. However, the decreased slope of tan δ is unique and cannot be attributed to the observed change in crystal structure. The decrease in temperature dependent relaxation approaching the α-transition suggests that the F-MWCNTs are able to resist relaxation of PP chains within crystalline domains and likely also at crystalline-amorphous interfaces.

Approaching T_α, the amorphous domains become fully relaxed as the crystalline lamellae approaches the melt state. It is interesting to note that in this region, the tan δ profiles for both PP/F-MWCNT systems are nearly identical and their respective values of G' begin to converge. At ~ 130°C and up to the onset of melting, the storage moduli of the injection-molded PP/F-MWCNT systems are identical. This suggests that the observed differences between the systems containing F-MWCNTs primarily originate from features in the amorphous region and crystalline-amorphous interfaces, which indicates that the higher loading of F-MWCNTs are not well integrated within the crystalline structure and therefore fail to provide any additional reinforcement benefit.

Clear interpretation of the molecular scale mechanisms present in the injection-molded samples is challenging because of the polymorphic character of the PP matrix, and potentially frozen-in molecular orientation at the PP/F-MWCNT interface. Compression-molded samples were prepared to more clearly elucidate interaction between the phases in the absence of multiple crystal phases, molecular orientation or external forces (Figure 3.7). The T_g is negligibly affected by the presence of the F-MWCNTs, which indicates that the overall dynamic mechanical behavior is not significantly altered. The peak intensity of tan δ at T_g is significantly increased in the PP/F-MWCNT (0.1 wt.%) system, and the slope of tan δ is decreased for $T > T_g$ (Figure 3.7b). Three separate samples were measured to confirm that these behaviors were consistent. The increased damping at T_g is not likely related to any MWCNT-induced change in the PP matrix, and there is no clear reason why the MWCNTs would directly enhance mechanical damping. The enhanced damping is therefore attributed to the presence of a fluid-like PP/ODA interface at the F-MWCNT surface, which was suggested in our previous work [75]. The compression-molded PP/ODA (0.5 wt.%) system exhibits a significant decrease in G' and increase in tan δ throughout the entire temperature range, which supports this conclusion. Below T_g, the storage modulus is slightly increased with the addition of 0.1 wt.% F-MWCNT (~10%), and increases relative to the neat PP with temperature. No significant change in DMA spectra was observed in the PP/P-MWCNT (0.1 wt.%) system relative to the neat PP.

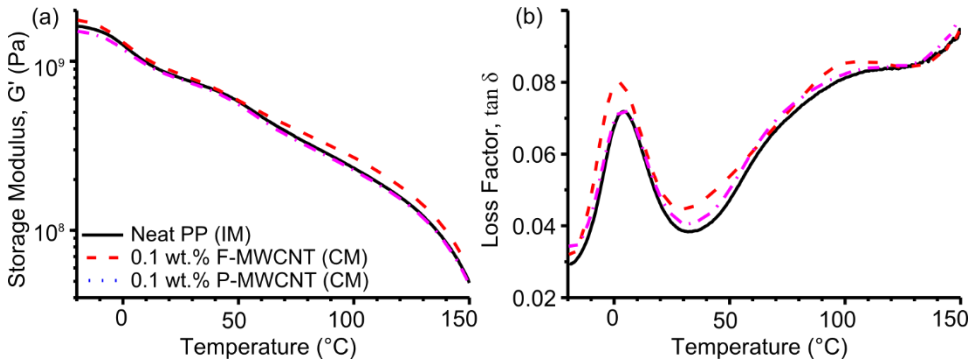

Figure 3.7. DMA measurements of compression-molded PP composite systems. (a) Storage modulus and (b) loss factor, obtained from isochronal measurements at frequency of 1 Hz and ramp rate of 3°C/min in torsion.

3.3.4 Tensile properties

Representative engineering stress – true strain tensile curves of the PP nanocomposites are shown in Figure 3.8. A summary of the tensile properties is provided in Table 3.3. The addition of only 0.1 wt.% F-MWCNT increases elastic modulus ~ 40% compared to the neat PP. To quantitatively compare the change in modulus with other works, we calculated the rate of modulus increased with respect to filler volume, dE/dV_f, which is a figure of merit proposed by Cadek et al. [106]. Assuming that the PP matrix and MWCNTs have densities of 0.91 g/cm^3 and 2.15 g/cm^3, respectively, $dE/dV_f \approx 1440$ GPa at 0.1 wt.% F-MWCNT, which is among the largest values reported for CNT-filled polymers available in the literature [107]. We note that similar gains in mechanical properties have been privately reported to us by industry, which suggests that the improvement may be characteristic of any system containing well dispersed, individual MWCNTs that exhibit adequate compatibility with the host polymer matrix. However, we are unaware of any similar findings in the

published literature. Increasing the concentration of F-MWCNTs does not further enhance modulus, and substantially diminishes the reinforcing efficiency, $dE/dV_f \approx 280$ GPa at 0.6 wt.% F-MWCNT. The PP/P-MWCNT (0.1 wt.%) system shows an insignificant improvement in modulus (7% increase), and relatively low reinforcing efficiency of $dE/dV_f \approx 230$ GPa. At 0.5 wt.% ODA loading, the elastic modulus is decreased slightly, which further confirms that the functionalizing agent has little direct contribution to tensile behavior.

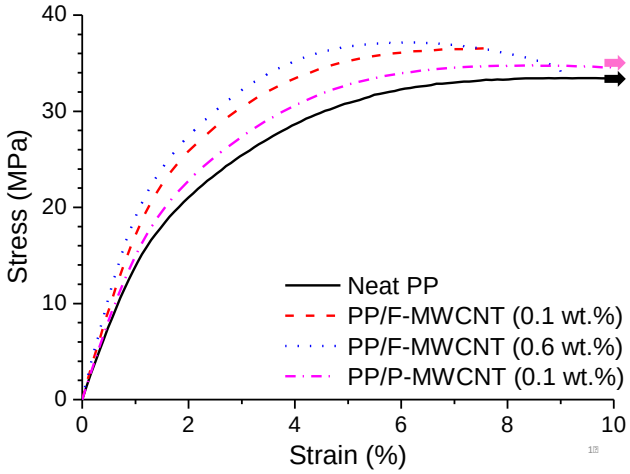

Figure 3.8. Tensile stress-strain curves for neat PP and nanocomposite systems.

Table 3.3. Summary of tensile properties of PP/F-MWCNT composites prepared by injection-molding and compression-molding.

	Injection-Molded			Compression-Molded		
	E (GPa)	σ_y (MPa)	ε_B (%)	E (GPa)	σ_y (MPa)	ε_B (%)
Neat PP	1.5 ± 0.04	34.3 ± 0.82	>300%	1.7 ± 0.05	34.0 ± 2.3	9% ± 1%
0.1 wt.% F-MWCNT	2.1 ± 0.05	39.8 ± 1.70	10% ± 4%	2.0 ± 0.09	33.4 ± 0.9	5% ± 1%
0.6 wt.% F-MWCNT	2.2 ± 0.20	40.7 ± 1.50	12% ± 8%			
0.1 wt.% P-MWCNT	1.6 ± 0.06	34.3 ± 0.61	>300%	1.7 ± 0.17	33.0 ± 1.4	8% ± 3%
0.5 wt.% ODA	1.4 ± 0.10	37.7 ± 0.70				

The yield strength of PP is also significantly improved due to the presence of 0.1 wt.% F-MWCNT (~ 16% increase), although the elongation at break is substantially decreased. Analysis of the tensile fracture surface revealed that fracture occurs following neck formation and limited drawing in the tensile direction. Significant stress

whitening was also observed, which indicates that the PP lamellae are able to exhibit limited plastic deformation prior to fracture. In the PP/F-MWCNT (0.6 wt.%) system, fracture occurs without any evidence of yielding, necking behavior, or stress whitening. The tensile fracture surface was smooth and characteristic of brittle fracture in a glassy polymer. The incorporation of 0.1 wt.% P-MWCNT does not significantly influence any of the tensile properties of the PP matrix, which we attribute to poor dispersion and a lack of interaction between phases. The yield strength of the PP/ODA (0.5 wt.%) system is increased slightly (~ 10%), and ductile fracture was observed with a moderate decrease in elongation at break. The decrease in ε_B for PP/ODA is likely due to the increase in spherulite radius, which typically causes failure at weak interspherulitic boundaries due to the formation of voids during thermal contraction, and segregation of impurities.

Compression-molded samples were prepared to investigate whether the observed changes in mechanical properties may be due to processing conditions or crystal structure (Table 3.3). The unfilled compression-molded PP exhibits a slightly higher modulus, no change in yield strength, and lower elongation at break than the injection-molded PP. These results are in agreement with previous reports on the influence of β-form crystal fraction on mechanical properties [108]. The compression-molded PP/F-MWCNT (0.1 wt.%) shows a much smaller increase in modulus relative to the injection-molded sample, and negligible change in σ_y compared to the neat PP. This indicates that the improvement in elastic modulus must be partially attributed to the α-nucleating ability of the MWCNTs, but does not account for the increase in yield strength. The

mechanical properties of the compression-molded PP/P-MWCNT (0.1 wt.%) are nearly identical to the neat PP, which further supports that there is no significant interaction between the phases.

3.4 Discussion

The improvement in mechanical properties at extremely low loading of MWCNTs greatly exceeds previous reports of semi-crystalline polymers reinforced with CNTs, which may be broadly attributed to the successful dispersion and compatibilization of disentangled MWCNTs into the semi-crystalline PP matrix. Our novel pre-treatment method offers exciting opportunities to significantly improve material properties, particularly electrical conductivity, dimensional stability, thermal stability, and heat deflection temperature, without sacrificing processability or environmental stability. The present discussion will focus on identifying the potential mechanisms responsible for the greatly improved modulus observed in this work, and to consider the generality and broader applications of our findings.

It is well known that the presence of CNTs dramatically modifies the morphology of semi-crystalline polymers. In this work, DSC and WAXD measurements confirmed that the degree of crystallinity is not affected by the MWCNTs, and no changes in lamellar orientation or anisotropy were detected with SAXS and OM observations. The nucleating ability of the MWCNTs substantially reduces spherulite diameter and completely suppresses the formation of β-form crystal at loading of only 0.1 wt.% F-MWCNT. Given the relatively small fraction of β-form crystallites in the

neat PP, this contribution is not sufficient to account for the magnitude of modulus improvement, or the significant decrease in ductility in both PP/F-MWCNT systems. SAXS measurements show the MWCNTs do not change the 2D lamellae structure of the PP, and no significant change in lamellae thickness could be identified. These results show that the indirect contributions of the MWCNTs are not sufficient to adequately describe the change in mechanical behavior observed in the PP/F-MWCNT systems, which indicates that additional, direct reinforcement mechanisms must also be present.

During injection-molding, the molten PP/MWCNT resin is forced into a cold mold cavity and subsequently crystallizes in the presence of a highly heterogeneous distribution of thermal stresses [109]. The PP chains are significantly stretched and uncoiled due to the shear and elongational stresses at the mold entrance, but tend to rapidly relax during cooling, and are generally unoriented in the core region. The shearing stresses also likely extend the individually dispersed MWCNTs in the flow direction, which increases the available surface area and favors a high nucleation density along the entire MWCNT surface. Due to the mutual orientation of the PP chains and MWCNTs in the flow direction during molding, PP chains at the MWCNT surface will tend to be anchored with molecular axis parallel to the long axis of the MWCNTs. Upon cooling, crystal growth proceeds fastest perpendicular to the MWCNT axis, which results in the highly ordered, transcrystalline PP domains observed in Figures 3.1 and 3.2. The WAXD measurements revealed that the (040) lattice planes of the MWCNT-nucleated PP crystals are preferentially oriented in the molding direction, and that crystal growth is favored in the respective b-axis direction. A schematic of the proposed mode

of crystal nucleation is provided in Figure 3.9a, where the shaded and white triangles correspond to the 2 different chiral populations of PP molecules, and are shown with c-axis oriented out of the page. The c-axis of the PP unit cell is depicted parallel to the MWCNT axis, which is in agreement with our description of shear-induced alignment during molding, and consistent with most previous reports [110]. It is clear from Figure 3.9a that even though crystal growth along the a*-axis is preferred [111], the high density of active crystal nuclei behave as lateral barriers and force crystal growth along the b-axis.

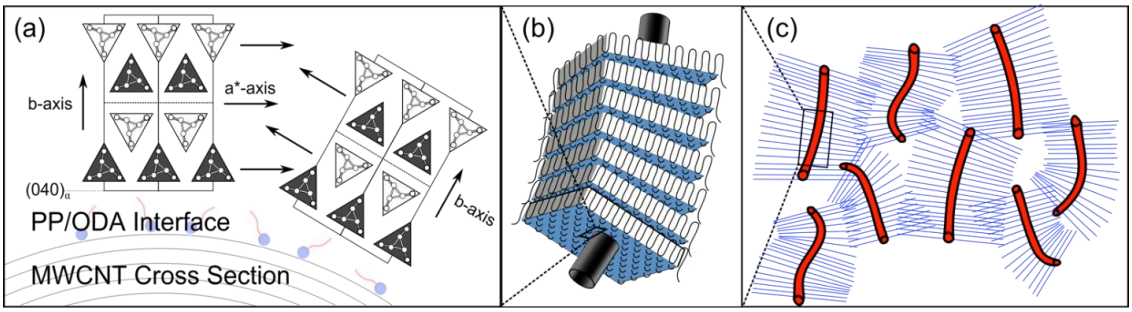

Figure 3.9. Schematic showing structure of PP/F-MWCNT across multiple length scales. (a) Proposed orientation of the PP unit cell at the F-MWCNT surface, where (040) plane of α-form crystal unit cell is parallel and the b-axis is perpendicular to the long axis of the MWCNT. The c-axis of the unit cell is projected out of the page. Each layer corresponds to a population of chiral helices, represented by triangles, with anti-chiral alternating layers. The ODA functional group is shown schematically as a primary head and long tail corresponding to the covalent amide linkage ((C=O)NH) and long-chain alkyl tail ($C_{18}H_{37}$), respectively. (b) Bulk structure of PP/F-MWCNT with localized transcrystalline domains extended radially from the F-MWCNT surface. (c) Network of individual MWCNTs with interfacially crystallized PP domains extending from surface.

For the purpose of this discussion, the most significant consequence of the confined mode of crystal growth is the interaction of extended MWCNTs with highly oriented, uniform transcrystalline PP layers, which is illustrated in Figure 3.9b. The

nucleated crystallites are exclusively α-form PP, and the size and perfection of the crystals are increased relative to the neat PP. Several recent reports have suggested that uniform interfacial crystallization results in excellent load transfer efficiency and high interfacial adhesion between the polymer and CNT [111]. Furthermore, the mismatch in the coefficient of thermal expansion between the PP and CNTs may favor mechanical interlocking between phases due to thermal residual compressive stresses [112, 113]. The resulting global microstructure, illustrated in Figure 3.9c, consists of uniformly dispersed, high aspect ratio F-MWCNTs that are preferentially aligned in the molding direction and integrated within an array of transcrystalline α-form crystals that extend along the length of the MWCNT. The TEM micrographs in Figure 3.2 support the proposed microstructure, and the TEMT results in Figure 3.3 provide the first unambiguous evidence that the PP crystal lamellae and F-MWCNTs are spatially associated in an injection-molded nanocomposite. At low loading, the extended domains will overlap and result in significant load transfer between reinforced regions. This mechanism of global reinforcement is similar to our previous findings in epoxies [68, 69], but is more effective in this case because the transcrystalline domains effectively multiply the volume fraction of MWCNTs.

The formation of a well-defined transcrystalline interface is not unique to this work and may be a general feature of PP/CNT systems [68, 85, 86]. The substantial increase in modulus and associated decrease in ductility has not been reported, which we attribute to previous challenges in achieving adequate dispersion of CNTs in large quantities, and lack of compatibility between phases. The compatibilization is extremely

important in this context because it provides a mechanism for the F-MWCNTs to interact and transfer load between phases. The uniaxial tension and DMA findings indicate that the F-MWCNTs are able to directly reinforce crystalline domains and amorphous interlamellae layers. In this case, the MWCNTs serve as physical anchors and provide continuity between crystalline lamellae, which suggests that they behave as "super" tie-chain molecules. The anchoring of crystalline lamellae will also likely prevent significant intralamellar slip and other dislocation processes in the crystal phase, which should severely inhibit plastic deformation upon yielding.

The above description is consistent with the uniaxial tension results of the PP/F-MWCNT (0.1 wt.%) system, which show limited interlamellar deformation and molecular orientation prior to fracture. At slightly higher loading of 0.6 wt.% F-MWCNT, there is no evidence of plasticity or yield behavior during uniaxial tension. From the SAXS and DMA results, we proposed that the higher loading of F-MWCNTs are not well-integrated in the transcrystalline structure and therefore introduce more significant disorder between ordered domains. The observed brittle fracture prior to necking indicates that the resulting microstructure from the higher loading of F-MWCNTs completely inhibits intralamellar deformation. The relatively high elongation at break of the PP/P-MWCNT (0.1 wt.%) system is attributed to the poor integration of the non-compatibilized CNTs within the lamellar structure of the matrix. Further work is being pursued to more explicitly identify the deformation and fracture mechanisms of these systems.

The proposed reinforcement mechanism does not depend on any particular features of our nanoplatelet-dispersion method, and requires only excellent dispersion and good compatibility between polymer and CNT. This description should therefore be general to any PP/MWCNT systems. The unique feature of the method used in this work is that the MWCNTs are disentangled and isolated prior to dispersing in the PP matrix. Therefore, no significant mechanical forces are required during processing. This approach preserves the useful properties of the MWCNTs, and the stability of the dispersion depends only on the thermal stability and compatibility of the functional group. Furthermore, there is no need to modify the properties of the neat PP matrix through grafting reactions or to introduce surfactants or interfacial agents that may diminish performance and environmental stability. This should enable the production of PP/F-MWCNT nanocomposites using standard processing methods and equipment, and is therefore suitable for high volume production. As the interaction between the PP matrix and the F-MWCNTs is governed by the selection of functional group, this approach may be easily adapted to other semi-crystalline polymers provided that sufficient compatibility is achieved.

3.5 Conclusions

Disentangled MWCNTs were functionalized with ODA and uniformly dispersed in a commercial grade PP by injection-molding. The mechanical properties of the PP were substantially enhanced at low loading, but provided relatively little additional improvement at higher loading. The dispersion approach used in this work reduced the critical concentration for bulk modification of the PP crystal structure and resulted in

preferential crystal growth due to the orientation and extension of the MWCNTs during injection molding. The F-MWCNTs partially influence the tensile properties by modifying the crystal phase of the PP, and are proposed to additionally reinforce multiple lamellar domains and amorphous regions between crystallites as “super”-tie chains. The process may be used in high-volume commercial processing approaches and can be modified by appropriate selection of functionality for use in any polymer matrix.

CHAPTER IV

HYGROTHERMAL BEHAVIOR OF POLYBENZIMIDAZOLE

4.1 Introduction

Polymeric materials have become an attractive choice to address challenges across a wide range of emerging technologies, including those associated with energy generation and storage [114, 115]. Recent advancements in polymer chemistry have also facilitated the design of new materials with improved physical and chemical properties. These properties can be tailored to meet the requirements of many demanding applications [18, 19, 26, 116]. Despite these advances in the development of novel polymeric materials, progress in improving chemical and thermal stability under extremely harsh environments remains a persistent challenge [117-120]. After decades of effort, polymers still suffer from issues such as premature aging and chemical degradation, which significantly limit their application ranges and service life in critical applications [121]. In many of the higher performing polymer types in service, the specific physical processes and chemical reactions that result in polymer degradation remains largely unclear due to a number of factors, including uncertainty in polymer degradation processes and reaction pathways, complex environmental conditions, presence of corrosive species, and so on.

---

*This chapter is reprinted from Polymer Volume 93, 14 June 2016, Pages 88–98. Peng Liu, Michael Mullins, Tim Bremner, James A. Browned and Hung-Jue Sue. Copyright (2016), with permission from Elsevier.

In the past decade, there has been a step change increase in the performance requirements of polymer-based materials in hydrocarbon exploration and recovery phases. For example, high demand exists today for materials that are capable of withstanding high pressure (>15,000 psi) and high temperature (>200 °C) environments, at times accompanied by corrosive or reactive species like H_2S. Poly [2,2'-(*m*-phenylene-5,5'-bibenzimidazole] (PBI) is an aromatic heterocyclic polymer. It is comprised of benzimidazole groups and phenylene groups along its backbone [122]. PBI can be used in high temperature due to its high glass transition temperature (T_g) and good retention of mechanical properties at elevated temperature [3, 123-127]. During the 1960-1980's, considerable effort was devoted to study the effects of specific chemical structure on the properties of PBI [128-130]. A series of isomeric PBI analogs were synthesized and studied to examine the effect of chemical structure on thermal stability. Studies related to the thermal degradation of PBI in inert or oxidizing conditions have also been reported [128, 130, 131].

By far the most widely used method for evaluating the thermal stability of PBI has been thermogravimetric analysis (TGA)[123, 128, 132-136]. Many TGA studies have demonstrated that the total weight loss of PBI at 600 °C is less than 6% in air. In this respect, PBI has always been regarded as a heat-resistant polymer considered to possess excellent thermal stability. However, TGA data provides information only about the threshold temperature at which major chain fragmentation occurs and subsequently causes volatility and weight loss. TGA is unable to measure property loss. For this

reason, the simple use of the onset temperature on rapid weight loss as a criterion to determine the thermal stability of PBI has limited value.

From a practical standpoint, thermal stability implies that the properties of interest, for instance, the mechanical integrity and elasticity, should be maintained at an acceptable level. A few publications have introduced a host of different methodologies and test conditions to investigate early stage thermo-degradation of PBI [51, 137-139]. These studies revealed that detectable changes in the molecular structure have already taken place before significant weight loss is observed. It has been proposed that the degradation of PBI is initiated by hydrolysis of the imidazole rings to an amine-amide structure [137]. The findings also suggest that the reaction is accompanied by cross-linking, subsequently forming a low solubility product. However, the nature of early-stage degradation mechanisms could not be elucidated from either FTIR or solid state NMR results [140, 141]. By analyzing the volatile species, researchers attempted to find trace quantities of small molecules that have functional groups similar to those compounds in the postulated reaction. Unfortunately, no evidence for the proposed mechanism was obtained.

Given the difficulty of the determination of the degradation mechanisms of PBI, model compounds that correspond to the repeat unit of PBI have been synthesized [138, 139, 142-144]. These experimental techniques aimed at validating the proposed mechanism for the thermal oxidative degradation of PBI, specifically to pinpoint the initiation sites where the decomposition occurs [138, 142, 144, 145]. A mass

spectrometer was employed to analyze the degradation products. The experimental results suggest that the oxidization of PBI starts with oxygenation at a specific weak-link in the repeat unit of the polymer chain. The N-H bond was found to be the most reactive site. On the other hand, the *m*-phenylene segment remains intact for longer periods of time or at higher temperature [138, 144]. Additional experimental evidence for this proposed mechanism was obtained by the observation that substitution of the imidazole hydrogen with a phenyl group remarkably increased the stability of the resulting polymer under isothermal conditions in air. However, the PBI polymer may behave differently than the model compounds for several reasons, including differences in end-groups, branching and the presence of impurities.

It should be noted that there is still some uncertainty over the precise mechanism of the degradation of PBI in environments where water is present [51, 140, 141, 146]. Previous studies indicated that the imidazole structure exhibits a high affinity for water, showing a maximum of 12% water can be retained [140, 141, 147-149]. Nuclear magnetic resonance (NMR) results have demonstrated that the water in PBI is able to organize into loosely bound clusters or form intermolecular hydrogen bonds[140]. The existence of large amounts of water inside PBI can facilitate the hydrolysis reaction, which may alter the degradation mechanism and significantly influence the course of the subsequent reactions.

In the present study, we focus on gaining fundamental insight into the mechanisms that cause the property deterioration of PBI. To achieve this objective, a

series of moisture and thermal treatments were applied to the samples to examine their response under various levels of exposure. Subsequently, the sample properties were characterized by TGA-MS, dynamic mechanical analysis (DMA), uniaxial tests and fracture tests. Special emphasis will be placed not only on the effect of heat on PBI but also with the coupled influences of moisture, mechanical stress, and chemicals on degradation. Systematic material conditioning was carefully administered to monitor degradation in PBI and to assure the validity of the comparisons. The relevance of the present study for structural application of PBI in harsh environment is discussed.

An additional aspect of this study is the influence of part fabrication on both mechanical properties and thermal stability. PBI is formed into parts using a sintering process in which powders are compressed and heated to temperatures up to 510 ºC [150]. PBI does not melt under these conditions to a degree that results in melt flow and loss of particle shape, and the "grain boundaries" of the original particles are detected by optical microscopy. The present study provides insight into the coalescence of discrete PBI domains and is therefore crucial to carefully control the molding process to achieve desired mechanical properties. It is hoped that fundamental knowledge can thus be gained regarding structure-property relationship on PBI and its related systems.

4.2 Experiment

4.2.1 Materials

The material used in this study was compression-molded Celazole® U60 PBI (MW=60,000 g/mol). The PBI material was supplied as stock shape with dimensions of 51 mm × 51 mm × 6.35 mm.

4.2.2 Sample conditioning

Previous studies indicated that PBI has high affinity for water and it absorbs moisture even during the sample handling[148, 151, 152]. Different drying processes were applied in this study to remove pre-existing moisture from the as-received samples. It is important to determine an appropriate condition to fully dry the samples as a reference and for comparison purposes. Two different drying processes were attempted. In the first process, the as-received sample was dried in vacuum at 90 ºC for 7 days to fully dry the sample and to minimize possible thermally induced degradation to the samples. To expedite the drying process, a higher drying temperature of 150 ºC for 3 days was also used to remove moisture in PBI.

Moisture saturation of samples was carried out by immersion in deionized water for a period of 7 days at 60 °C to reach equilibrium, but preventing any detectable chemical reaction from occurring (e.g. hydrolysis). Equilibrium saturation was deemed complete when no additional weight gain was observed. Lastly, the 288 ºC hot water treatment of samples was performed using a Parr pressure reactor (Model 4913). PBI plaques were confined in a steel wire cage that was fully immersed in water to stabilize

the sample in a turbulent steam environment. The sample was then heated to 288 ºC in a pressure vessel with a resulting pressure of 7.58 MPa (gauge). The array of samples prepared above gave an adequate range of conditions for understanding moisture and hot water exposure effects on mechanical properties of PBI. For convenience, all the sample treatment conditions are summarized in Table 4.1.

Table 4.1. PBI sample treatment conditions.

Conditioning Histories	Temperature (ºC)	Time	Environment
As-received	25	3 months	Air, 60% RH
Drying	90	7 days	762 mmHg vacuum
Drying	150	3 days	762 mmHg vacuum
Water-saturation	60	7 days	Deionized water
Hot water treated	288	2 days	Hot Water

4.3 Characterization

4.3.1 TGA and Mass Spectroscopy (MS) analysis

A TGA test (TA Instrument Q500) was performed on each of the samples in both nitrogen and air atmospheres. A piece of the sample, roughly 7 mg, was heated from 40 °C to 900 °C at a rate of 10 °C/min.

The TGA coupled with MS analyses were carried out by TA Instruments Discovery Mass Spectrometer operated at 40 eV. The sample was placed in a platinum pan and was heated in helium from ambient temperature to 1000 °C at a rate of 10

°C/min. The scanning range was from 1 to 200 dalton. The quadropolar mass spectrometer was equipped with a dual detector system, which included a Faraday cup detector and secondary electron multiplier.

4.3.2 Swelling measurement

Three rectangular-shaped PBI samples with dimensions of 7 mm × 6 mm × 5 mm were precisely cut from a bulk sample by using a diamond saw. A Keyence VK-9710 violet laser confocal scanning microscope was used to measure the apparent volume V (volume of polymer and incorporated water) of the conditioned specimens at various water uptake levels. Then, the volume change was calculated using: $\Delta V = [(V-V_0)/V_0] \times 100\%$, V_0 is the volume of dried sample before the absorption test.

4.3.3 Dynamic mechanical analysis investigation

DMA was carried out using an ARES-G2 rheometer (TA Instruments) in torsional mode. The strain amplitude was set at 0.05%, which was verified to be within the linear viscoelastic region for all samples at 25 °C. The temperature was increased at a constant rate of 3 °C/min from −140 to 550 °C at fixed frequency of 1 Hz.

4.3.4 Mechanical testing

Uniaxial tensile tests were performed in accordance with ASTM D638–08. All room temperature tensile tests were performed using an MTS screw-driven testing machine operated a crosshead displacement rate of 5 mm/min. A calibrated MTS LX1500 laser extensometer was used to measure the true strain of the sample. The initial gauge length of each tensile specimen was 25.4 mm. The reported standard deviation in

elastic modulus, E, as well as tensile yield stress, σ_y, are based on an average of at least five tested specimens.

The effect of water content and 288 ºC hot water exposure on the fracture toughness values of PBI was determined by performing the single-edge-notch 3-point-bend (SEN-3PB) tests according to ASTM D5528–13. Because the PBI plaques were prepared by compression molding, which should not result in significant anisotropy, the specimens were machined without concern to orientation. The specimens have dimensions of $50.8\ \text{mm} \times 12.7\ \text{mm} \times 6.35\ \text{mm}$. To avoid the formation of unwanted plastic deformation during preparation of sharp crack for the quasi-static fracture test, a V-notch was first generated by using a milling machine, followed by introducing a sharp pre-crack by tapping a razor blade to wedge open the initial V-notch. The ratio of the initial pre-crack (a_o) to the specimen width (W), a_o/W, was controlled to be approximately 0.5. A MTS screw-driven testing machine was used to conduct the test at a constant crosshead speed of 1.25 mm/min at room temperature. At least four specimens were tested under each condition to allow evaluation of the repeatability of the results. The crack propagation was observed by an Olympus BX 60 polarized optical microscope. The fracture surface was examined by Keyence VK-9710 3D violet laser microscope.

Double-notch four-point-bending (DN-4PB) specimens were also prepared in order to study crack tip damage mechanisms upon subcritical crack propagation [153]. In these specimens two nearly identical cracks were prepared with care. The damage zone

region of the survived crack was polished to about 30 μm in thickness. The morphologies of these thin sections were examined using a transmission optical microscope (TOM) Olympus BX 60 under both bright field and crossed-polarized conditions.

4.4 Results and Discussion

4.4.1 Water content determination and volatile analysis of PBI

Figure 4.1 compares the TGA curves of the PBI samples dried in vacuum for 3 days at 150 °C (curve I), dried in vacuum for 7 days at 90 °C (curve II), stored in an ambient environment for 3 months (curve III), hot water treated for 2 days at 288 °C (curve IV) and exposed to water for 7 days at 60 °C (curve V). Despite drying in a vacuum for 7 days at 90 °C (curve II), weight loss does not stabilize until the temperature reaches about 425 °C. This weight loss process occurs both in N_2 and in air (Figure 4.2). Many previous studies attributed this weight loss to the evaporation of absorbed water in PBI [152]. As described qualitatively in previous work, PBI is hydrophilic and able to incorporate large amounts of water from the atmosphere[149, 154]. It has been reported that PBI can absorb as much as 7% water by weight under ambient conditions without receiving any special humidity conditioning treatment.

To determine whether the weight loss is solely due to water alone, a TGA-mass spectroscopy (TGA-MS) analysis was carried out on a sample that was dried in vacuum for 7 days at 90 °C. Mass spectroscopic analysis of the volatile components that are released during heating in helium is presented in Figure 4.3. In the temperature range

between 40 °C and 400 °C, a total weight loss of 4% is observed from the TGA curve. This result is identical to the one that was acquired from TGA without the mass spectrometer attached. In the temperature range between 40 °C to 400 °C, two ions with m/z (mass-to-charge ratio) equal to 17 and 18 are observed with a constant ratio of intensities of 5.8. In addition, the intensities of these two ions have a maximum which matches to the maximum rate of water evaporation at 225 ºC as shown in Figure 4.2. These findings suggest that the ion peaks at m/z = 17 and m/z = 18 are from water, which generates H_2O^+ and OH^+ during the ionization process. The lack of significant ion intensity at 16 m/z rules out ammonia as a degradation product at these temperatures, given the fact that ammonia produces two major ion species at 16 and 17 m/z at a ratio of 1:1.25 under the same ionization conditions [155].

The ion intensity at 17 m/z in the temperature range between 40 ºC and 800 ºC shows two separate peaks at 225 °C and at 700 °C. This suggests two distinct thermal degradation processes. A portion of the weight loss in the higher temperature process may be due to ammonia formation. The observation of a significant peak at 16 m/z supports this hypothesis. The work by Schulman also confirmed that ammonia was not identified by the gas chromatography in the temperature range below 600 ºC [137]. Therefore, the weight loss between 40 and 400 ºC is exclusively due to loss of water. As shown above, TGA-MS is able to accurately determine the water content in the samples that possess different conditioning histories. Since weight loss from 40 °C to 425 °C range is solely due to water loss, TGA analysis was employed to determine the water content of PBI samples.

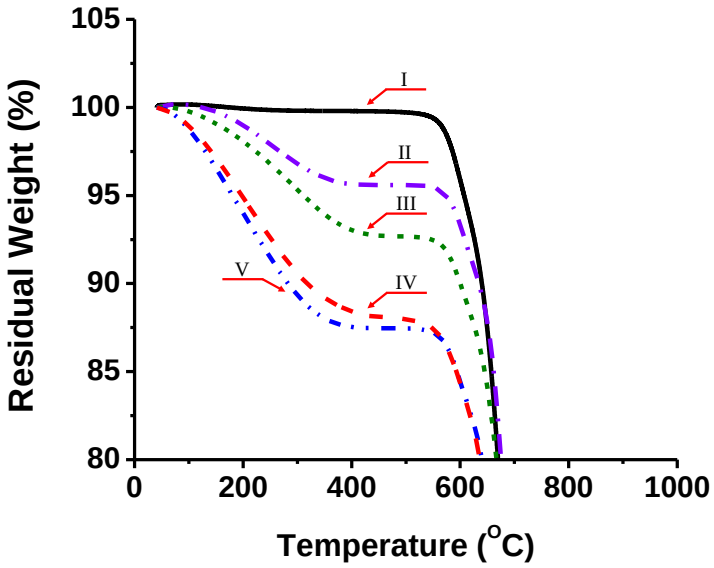

Figure 4.1. TGA curves of the PBI samples. (I)Sample dried in vacuum for 3 days at 150 °C. (II) Sample dried in a vacuum for 7 days at 90 °C. (III) Sample stored in an ambient environment for 3 months. (IV) Sample was hot water treated for 2 days at 288 °C. (V)Sample exposed to water for 7 days at 60 °C (curve V). The atmosphere is air, heating rate is 10 °C/min.

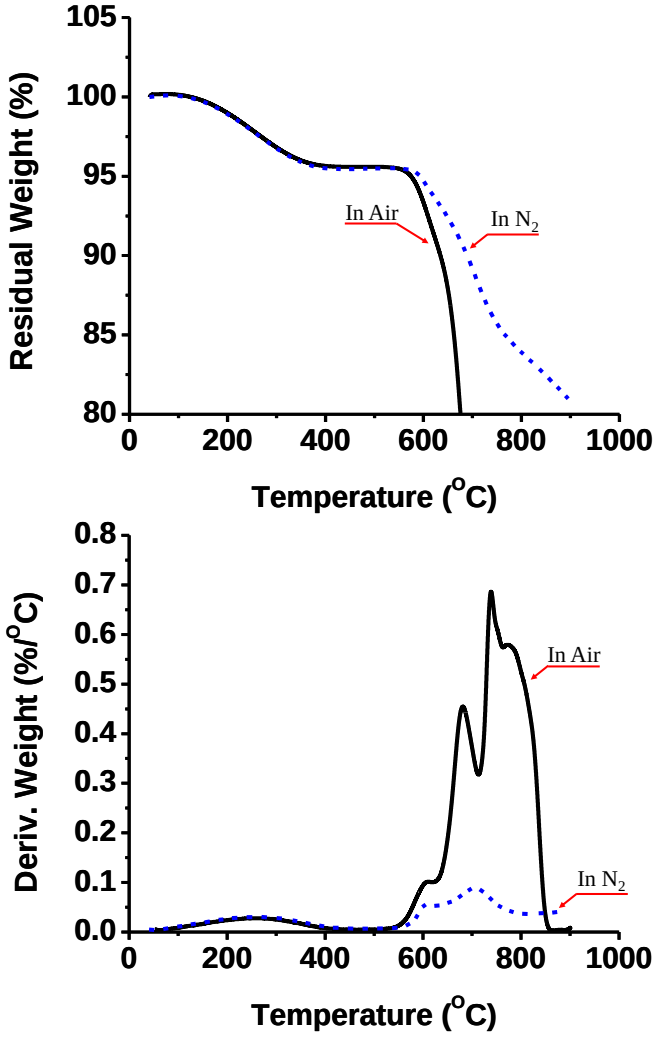

Figure 4.2. TGA curves of the PBI samples after dried in vacuum at 90 °C for 7 days. Heating rate is 10 °C/min.

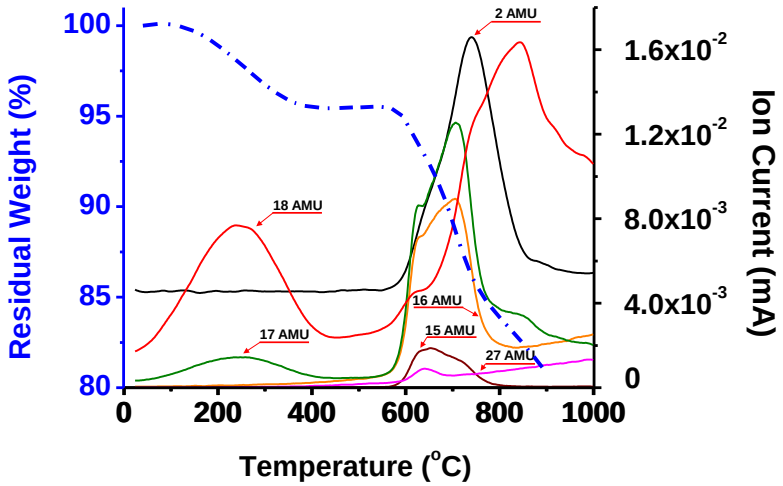

Figure 4.3 TGA-MS curves of PBI samples after dried in vacuum at 90 °C for 7 days. The atmosphere is helium. Heating rate is 10 °C/min. AMU is defined as atomic mass unit.

The weight loss below 300 °C is predominantly caused by loss of water. The polymer is stable until ~550 °C at which point severe degradation occurs as evidenced by numerous fragments that give ions with m/e of 2, 15, 16, 17, 18, and 27 daltons, and by the sharp decline in weight of the sample. The mechanism and products of the decomposition that occurs at high temperature (above 550 °C) are difficult to determine, but it is likely irreversible and involves chain scission. The loss of water that occurs below 300 °C is reversible, and is likely a combination of absorbed water and reversible hydrolysis of the benzimidazole group. More discussion will be included in the dynamic mechanical analysis session.

4.4.2 Dynamic mechanical behavior

The quantitative measurement of energy storage and dissipation as a response to dynamic oscillatory excitation is frequently more sensitive and effective at detecting molecular scale chain motions [156, 157]. Temperature dependence of relaxation time or

activation energy for relaxation, as well as the shape of the relaxation spectrum also allows us to acquire more detailed information on the polymer chain motions. Before the DMA test, the water content for specimens in the as-received condition and water-saturated condition reached 7 wt.% and 13 wt.%, respectively. The dry condition contains 0% water. As shown in Figure 4, the PBI sample in dry condition exhibits three relaxation peaks at +435, +215 and -55 °C, which are labeled as α, β, and γ peaks, respectively. The prominent α relaxation is due to large-scale segmental motion during the glass-rubber transition. However, there is nota general agreement on the mechanism of molecular motion that is associated with the sub-T_g transitions [156]. It is commonly referred to as cooperative or local mode motions of the moieties in the molecule. Early work reported that the β relaxation could be considerably suppressed by annealing at a temperature close to T_g [158]. The annealing process has an effect of increasing bulk density by facilitating chain packing; therefore the relaxation amplitude becomes suppressed. Recent studies on the effect of moisture absorption in polyamide demonstrates that the β relaxation is associated with the interaction between -NH groups and water molecules [159, 160]. Furthermore, these studies have shown that the complete elimination of water results in a disappearance of the β relaxation peak. However, in our case, the dry sample still exhibits a β relaxation peak. It maybe due to

the intrinsic property of PBI and is not influenced by the presence of water, but it is more likely that the strongly hydrogen bonded water molecules were not completely removed during the drying process. As shown in Figures 4.4 and 4.5, it is readily apparent that the presence of water has a great effect on the dynamic mechanical behavior of PBI. In agreement with the previous investigation, by increasing the water content, both of the sub-T_g transitions shift to lower temperatures. The water molecules can form hydrogen bonds with the nitrogen atoms in PBI, which leads to an increase in the motional degrees of freedom of the polymer. This enhances chain mobility such that molecular relaxation is possible at a lower temperature.

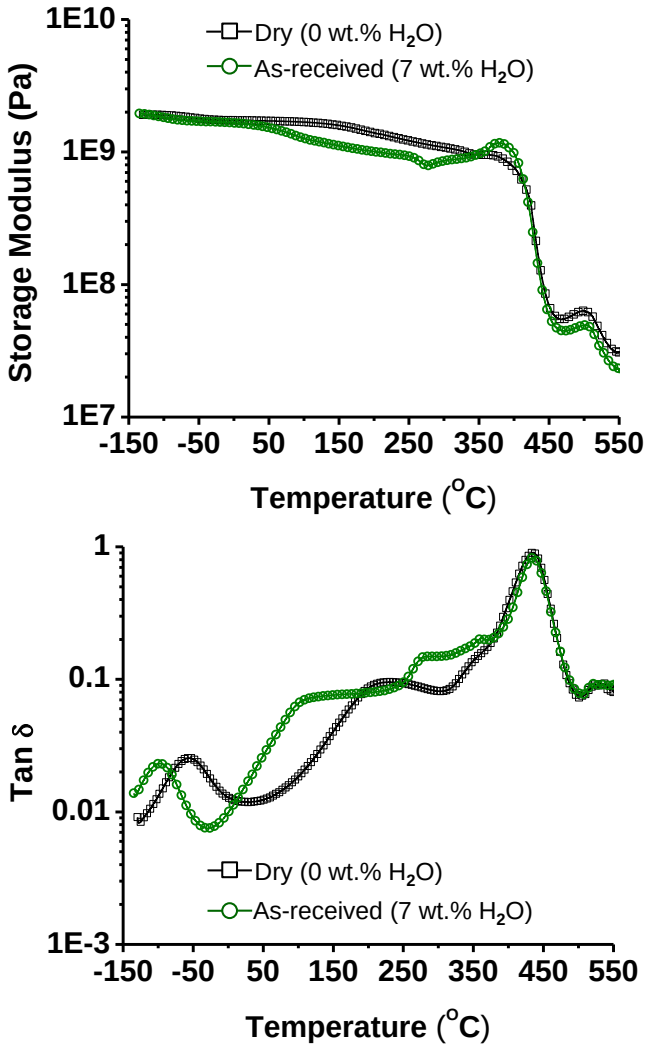

Figure 4.4. Temperature dependence of storage modulus and tan δ for dry and as-received PBI.

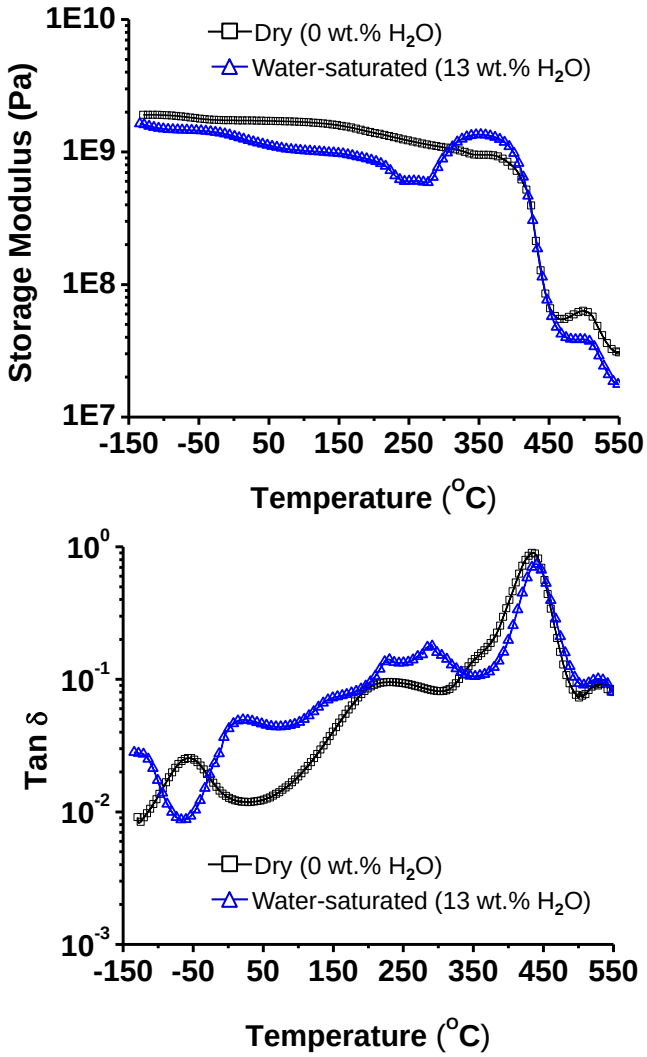

Figure 4.5. Temperature dependence of storage modulus and tan δ for dry and water-saturated PBI.

The nature of the temperature or frequency dependence of many macroscopic mechanical properties can be predicted by assuming an Arrhenius-type relationship using the activation energy of the relaxation[161]. Therefore, DMA testing allows us to assess the mobility of polymer chains, which can be indicative of the elasticity or ductility of the material. However, this relationship becomes considerably more complex when degradation occurring during the test procedure affects the viscoelastic properties.

As shown in Figure 4.4, the as-received sample exhibits an initial decrease in storage modulus, followed by a rapid recovery of the storage modulus with increasing temperature during the DMA experiment. This phenomenon is more prominent for the sample that contains a large amount of water as shown in Figure 4.5. It can be clearly observed in Figure 4.6, after hot water treatment at 288 °C for two days, the intensity of the T_g peak in the tan δ curve is suppressed, and its full-width half-maximum broadened. The storage modulus of the 288 °C hot water treated sample decreased significantly.

The DMA behavior of PBI from room temperature to T_g can be divided into two regions. Initially, in the temperature region from 40 °C to 250 °C, the storage moduli of the two PBI samples containing water are significantly lower than those of the dry sample. This effect can be attributed to the plasticization effect of water on the cooperative motions of the segmental chains involved in this process. Moreover, the plasticization also enhances the level of molecular motion within this temperature regime, leading to an increase in the relaxation characteristics as shown in the tan δ curve. It should be noted that at a ramp rate of 3 °C/min during the DMA test, the timescale of water elimination due to diffusion and evaporation is slow relative to the heating rate, and thus the amount of water retained is much higher than would be experienced at a lower rate or at static conditions. Mobile water is not completely removed until the temperature reaches 420 °C. These results reflect the instantaneous DMA behavior of a 3 mm thick sample.

In the second regime, at about 250 °C, the storage moduli of the two PBI samples containing various amounts of water exhibit a steep decrease of storage modulus, followed by a pronounced recovery of the storage modulus (Figures 4.4 and 4.5). As the temperature rises above the T_g, all the PBI samples exhibit a rubbery plateau, reminiscent of a crosslinked polymer system with a high plateau modulus above T_g. Careful analysis of the DMA in the temperature range from 250 °C to 550 °C suggests chain scission and crosslinking might have taken place sequentially. The steep decline of the storage modulus strongly suggests that hydrolysis reactions on the PBI have occurred. The hydrolysis process presumably can proceed and cause chain scission. However, lower water concentrations favors crosslinking through free radical processes at high temperatures when the majority of mobile water has been evaporated. Therefore, as the temperature is increased, crosslinking processes become significant, and the modulus is increased compared to a non-crosslinked system.

The magnitudes of rubbery plateau moduli of dry, as-received and water-saturated samples follow an expected order from high to low. TGA results indicate that mobile water is completely eliminated at temperatures above 450 °C at a heating rate of 10 °C per minute, at which the plateau modulus is observed. Therefore, the variation of plateau modulus cannot be attributed to different water content, but to an increased crosslink density.

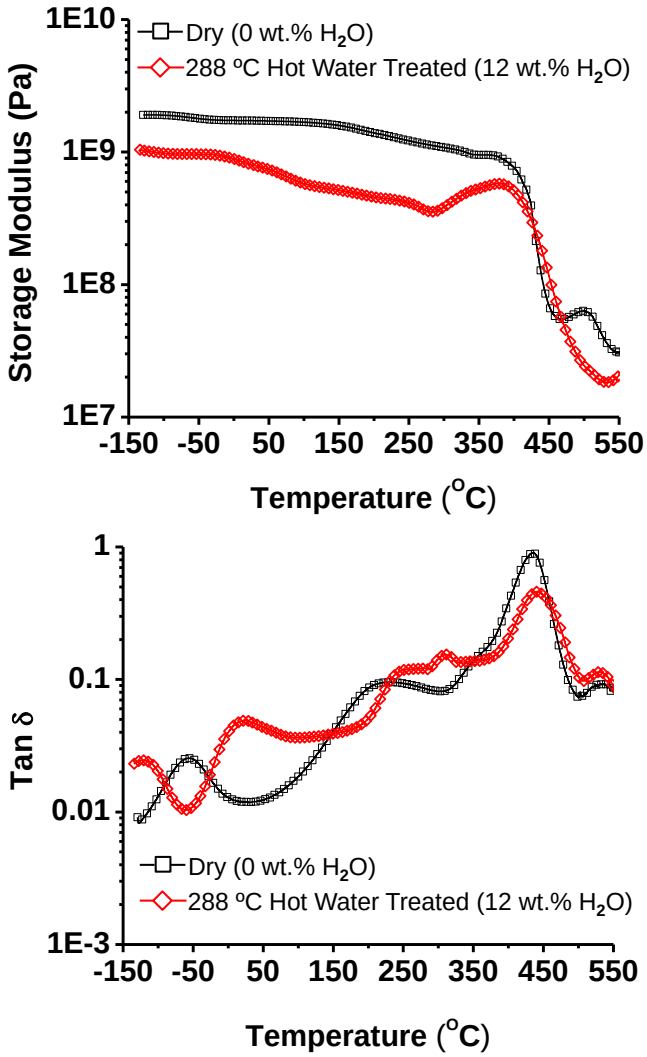

Figure 4.6. Temperature dependence of storage modulus and tan δ for dry and 288 ºC hot water treated PBI.

As shown in Figure 4.5, for the water saturated sample, the increase in storage modulus starting at temperature 300 °C is quite unusual [157, 162]. To the best of our knowledge, this phenomenon has not been reported in the past. The underlying physics behind this behavior needs to be determined. To demonstrate the reproducibility and

reversibility of this phenomenon, successive experiments were carried out whereby the temperature was ramped up to 400 °C followed by cooling back to room temperature, all using the same sample. The selection of this upper temperature limit that is below T_g is to minimize significant molecular relaxation or reorganization that may take place above the T_g, preserving the inherent microstructure of the PBI. As shown in Figure 4.7, the storage modulus of the dry sample is increased on the second heating cycle. The shift in the sub-T_g transition as measured by the tan δ peak is on the order of 50 °C. The amplitude of tan δ decreases after each heating cycle, indicating that there is a reduction in segmental motion of the polymer chains with each heating cycle.

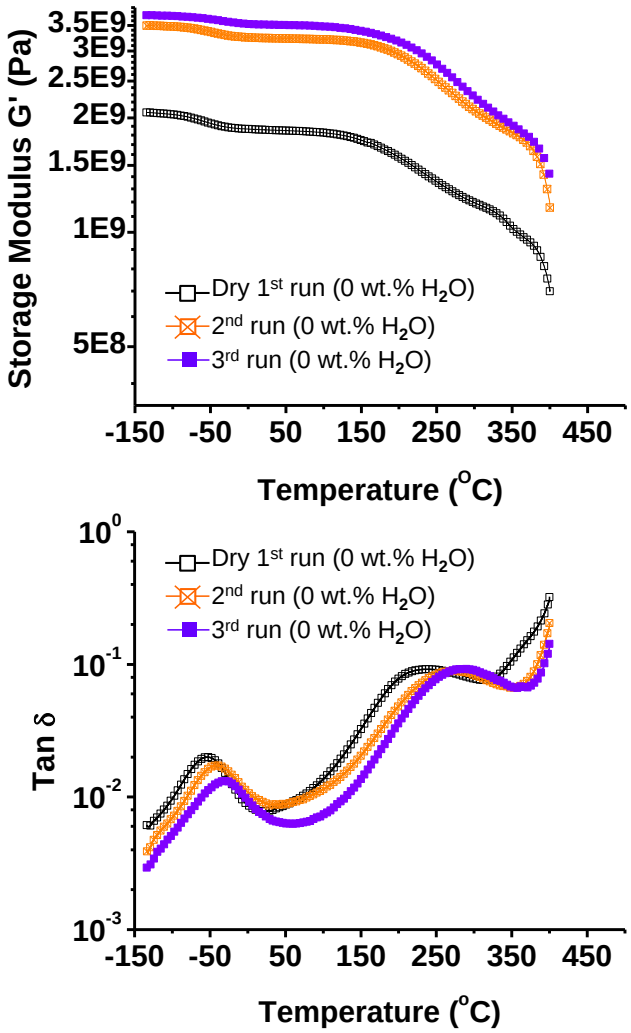

Figure 4.7. Temperature dependence of storage modulus and tan δ for dry PBI. Successive heating cycles were carried out on the same sample.

Before the DMA test, the water content for specimens in water-saturated condition was 13 wt.%. As shown in Figure 4.8, after the first heating cycle, the water content dropped to 1 wt.%. The storage modulus recovery phenomenon that occurs during the first temperature ramp is absent in the subsequent tests. The tan δ peaks are also broadened and shifted to higher temperatures.

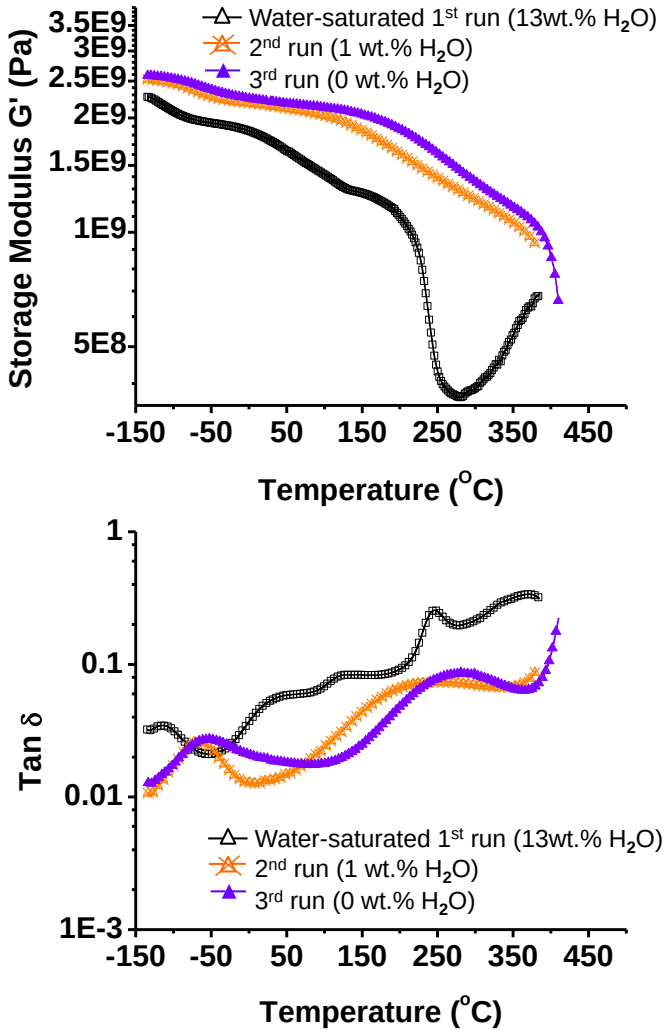

Figure 4.8. Temperature dependence of storage modulus and tan δ for water-saturated PBI. Successive temperature ramps were carried out on the same sample.

The increase in storage modulus that takes place on the second and third experiments can be observed on both the dry and water-saturated samples. This suggests that loss of absorbed water only partially accounts for the modulus increase found in the subsequent heating cycles. It has been suggested that a reversible hydrolysis can take place in PBI [137], as shown in the first step shown in Figure 4.9. When a large amount of water is present, for instance the first temperature ramp of the water-saturated sample

(see Figure 4.8), the decline of the storage modulus becomes apparent at the temperature as low as 225 °C. It is possible that this loss of storage modulus is associated with some of the originally absorbed water during the water immersion process, which then undergoes amine-amide interchange through hydrolysis. Internal re-closure to the imidazole regenerates the linear polymer and releases water.

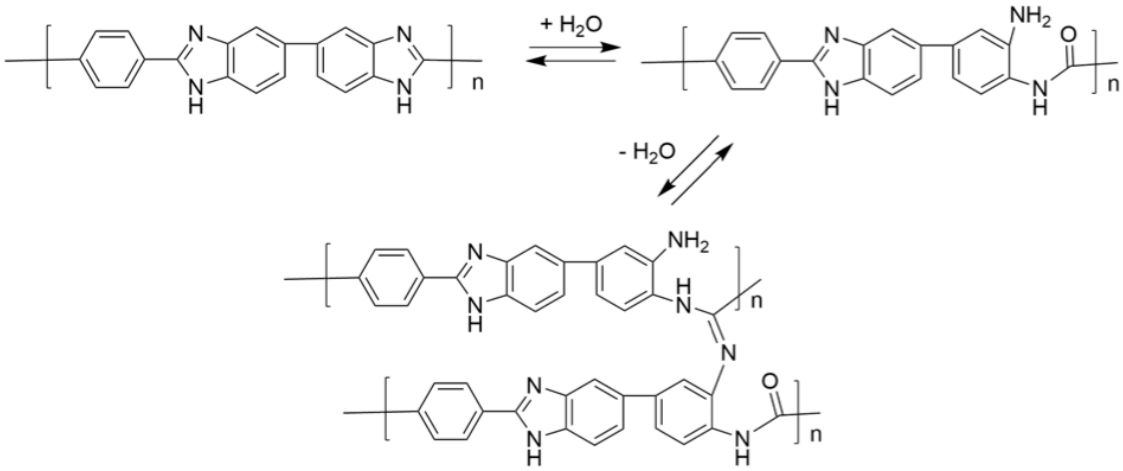

Figure 4.9. Postulated mechanism for crosslinking after hydrolysis.

It is possible that some inter-chain chemistry occurs, i.e., the second reversible step in Figure 4.9, between the amide of one chain and the amine of a second chain. Although this reaction is disfavored, if it occurs even to a small extent, a lightly crosslinked product would result. The results indicate that the increased storage modulus on the second and third heating cycle is a net effect of both the suppression of plasticization effect by water removal and crosslinking reaction as the testing temperature approaches the T_g of PBI.

4.4.3 Uniaxial tensile behavior

Tensile testing was performed at room temperature to evaluate the effect of incorporated water and hot water treatment. As shown in Figure 4.10, the absorption of water is significantly higher than many other engineering polymers. The absorbed water causes swelling of PBI. The volume of water-saturated sample containing 13% of moisture by weight was increased by 8% when comparing against the dry sample. As the subsequent discussion will reveal, water has a significant impact on the mechanical properties, including modulus, strength, and density.

The apparent volume increase of PBI falls below the values that are predicted based on the rule of mixtures. This suggests that some water molecules have strong interaction with hydrophilic groups in PBI, which leads to rearrangement of intermolecular hydrogen bonding between polar groups in the PBI network. The representative tensile stress versus strain curves for all the samples are presented in Figure 4.11 for comparison. The representative tensile properties are listed in Table 4.2. The water-saturated PBI exhibits a lower modulus, lower tensile strengths and ultimate elongation-at-break than the dry PBI. The reduction of the modulus is due to the plasticization effect of water molecules. The decrease of ductility suggests that defects are formed during the water absorption process.

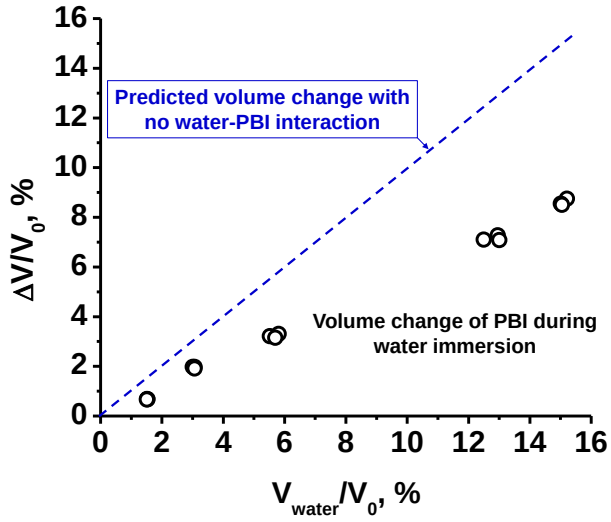

Figure 4.10. Volume change of PBI during water immersion at 60 °C.

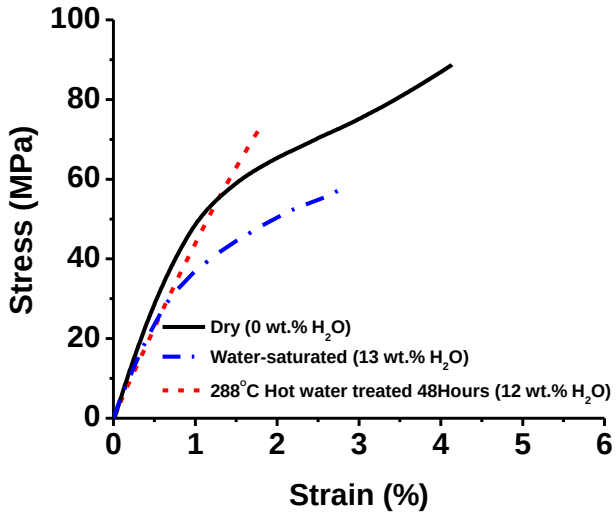

Figure 4.11. Typical stress-strain curves of PBI treated under different conditions.

4.4.4 Fracture toughness measurements and fracture mechanisms investigation

The fracture toughness, described as the critical stress intensity factor, K_{IC}, was measured using SEN-3PB specimens according to ASTM D5528–13. The stress intensity factor values were determined using the following equations:

$$K_{IC} = \left(\frac{P}{BW^{1/2}}\right) f(x)$$

$$f(x) = 6x^{1/2} \frac{[1.99 - x(1-x)(2.15 - 3.96x + 2.7x^2)]}{(1+2x)(1-x)^{3/2}}$$

$$x=a/W$$

where *f(x)* is a shape factor, *P* is the load at failure, *B* is the thickness of the specimen, *W* is the width of the specimen, and *a* is the crack length. The calculated fracture toughness values obtained from these equations are listed in Table 4.2.

Table 4.2. Summary of fracture toughness and tensile properties of PBI treated under different conditions. K_{IC} is the critical mode one stress intensity factor, E is the elastic modulus, σ is the ultimate tensile strength, ε_B is the extension at break.

Conditioning Histories	K_{IC}(MPa*m $^{1/2}$)	E (GPa)	σ (MPa)	ε_B (%)
Dry (0% H_2O)	2.86 ± 0.05	6.7 ± 0.4	87 ± 14	6 ± 2
Water-saturated (13wt.%H_2O)	2.92 ± 0.06	5.5 ± 0.5	65 ± 8	2.6 ± 0.5
288 ºC hot water treated (12 wt.% H_2O)	1.9 ± 0.01	4.7 ± 0.3	69 ± 4	1.8 ± 0.1

Table 4.2 reveals that fracture toughness decreases significantly for the samples that were conditioned in a hot water environment at 288 °C for 2 days. However, the fracture toughness of the water-saturated sample at lower temperatures did not experience significant deterioration compared to the dry samples.

The fracture surfaces of the SEN-3PB samples were analyzed using a Keyence violet laser confocal microscope VK9710. A scanning area of 600 μm × 500 μm was selected to show the representative fracture surface characteristics. As shown in Figures 4.12-4.14, Zone I represents the V notch region, zone II represents the razor tapping region, and zone III represents the crack initiation region.

The crack initiation region (zone III), which is just beyond the razor starter crack, is the focus of the study because this is more revealing of the advent of a fracture process. In the crack initiation region, localized plastic deformation, which led to formation of irregularly shaped ridges and river patterns, are apparent in both the dry sample and the water-saturated sample (Figures 4.12 and 4.13).

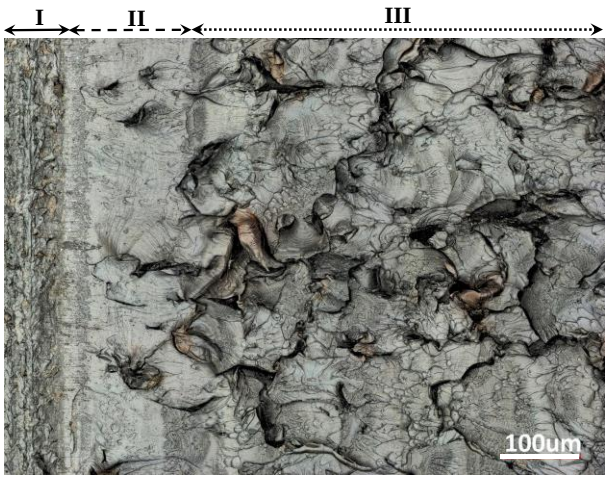

Figure 4.12. Fracture surface morphology of the dry PBI.

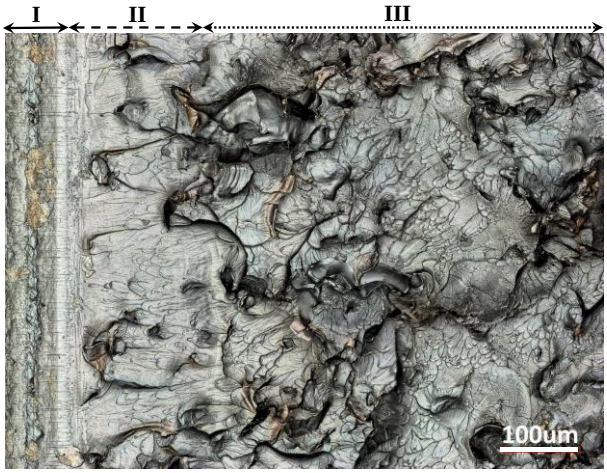

Figure 4.13. Fracture surface morphology of the water-saturated PBI.

In contrast to the dry and water-saturated specimens, the fracture surface of 288 °C, hot water treated sample is relatively smooth and featureless. As shown in Figure 4.14, large flaws are apparent on the surface. These flaws act as stress concentration sites and are surrounded by the closely spaced striations. The relatively featureless fracture surface implies that the 288 °C hot water treatment led to the embrittlement of the PBI and causes rapid crack propagation. Their corresponding fracture toughness value is also significantly lower than the "dry" and "water-saturated" samples.

The results shown in Table 4.2 indicate that water alone is not the primary cause of fracture toughness deterioration for PBI. However, combined with high temperatures, the presence of water can facilitate property deterioration for reasons noted above, and contributes additionally to significant fracture toughness reduction.

Characterizing the fracture toughness in tough materials would require the use of thick samples in order to satisfy the plane strain condition. Certain criteria must be

imposed to ensure that the plastic deformation at the crack tip is small. Brown and Strawley suggested an empirical equation that defines a minimum sample thickness (b_{min}) thus [163]:

$$b_{min} = 2.5(\frac{K_Q}{\sigma_y})^2$$

where K_Q is trial K_{IC} value and $\sigma_y$is the yield stress of the material for the temperature and loading rate of the test. Based on this equation, the minimum specimen thickness should be roughly 3 mm to ensure the crack initiation occurring at nominal stresses that are well below the tensile yield stress of the material. The actual specimens that were used in the SEN-3PB test for this study have a thickness of 6.35 mm. After close examination of the fracture surface of the samples, we found that initial crack front is not in a thumbnail shape. Furthermore, no ductile deformation shear lip at the edges is observed. All the information mentioned above suggests that the K_{IC} values obtained from the SEN-3PB test are valid and is independent of sample geometry. However, it is still difficult to unambiguously determine the fracture behavior of PBI simply based on the fracture surface observation. The DN-4PB test methodology is an effective tool for investigating the fracture process in polymer-based material [153, 164]. As shown in Figure 4.15(a), the dry PBI samples do not show a homogeneous morphology. Instead, micro-domains having a size of around 100 μm are observed.

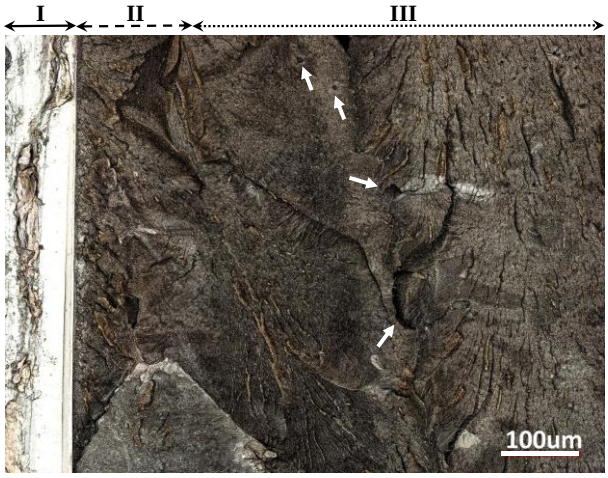

Figure 4.14. Fracture Surface morphology of the 288 °C hot water treated PBI.

Under TOM crossed polarization light, as shown in Figure 4.15(b), localized birefringence could be detected throughout the entire specimen. This further indicates the presence of localized residual stresses around the micro-domains in PBI after the molding process. As shown in Figure 4.15, after the 288 °C hot water exposure, no birefringence is observed. It is noted that the residual stresses around the micro-domains were mostly relaxed during the 288 °C hot water exposure.

TOM of the dry sample shows no evidence of crazing and the deformation zone is not well defined in front of the crack tip (Figure 4.15), suggesting that PBI is inherently tough. After the 288 °C hot water treatment, air bubbles form across the sample. A straight crack is observed (Figure 4.16). As it has been discussed in TGA-MS and DMA results, the hot water treatment induces significant molecular degradation of PBI.

It is noted that the PBI plaques are inhomogeneous in that imperfectly sintered particles are clearly visible, and have not fully coalesced. This finding suggests that the mechanical properties of PBI plaques are going to be greatly influenced by how the PBI molding process is conducted. An in-depth examination of the key processing parameters that will influence fracture behavior in PBI is necessary. The compression molding process for PBI usually requires an application of pressures up to 10,000 psi and temperatures of up to 510 °C to accomplish the coalescence of powdered PBI to produce a mechanically strong plaque[150, 165, 166]. Ward and Harb, et al reported compression molding of PBI that possess tensile strength up to 145 MPa[150]. In order to achieve high tensile strength, however, it was necessary to utilize a resin with an intrinsic viscosity of 1.1 dL/g. Use of resin with lower molecular weight resulted in correspondingly lower tensile strength of the molded article. As stated above, the mechanical properties of PBI are critically influenced by a combination of intrinsic properties and external factors involved during the molding process.

In a good agreement with the influence of absorbed moisture content on the rheological properties of PBI, the study on the mechanical properties of PBI indicates that moisture content will significantly influence fracture behavior when PBI is exposed to water at elevated temperatures. The mechanism of deterioration of mechanical properties over a prolonged exposure at high temperature includes morphological changes, swelling of PBI matrix, hydrolysis and crosslinking. The occurrences of these permanent structural changes on PBI decrease elongation, strength and embrittle the material. The utilization of TGA-MS and DMA as characterization tools enables a

conclusive investigation on the effect of water and other factors on the mechanical and thermal mechanical properties of PBI.

The present study offers important fundamental insights on the mechanisms that cause the property deterioration of PBI. With the key evidences pieced together, the underlying physics of the PBI property deterioration have been revealed. The DMA and TGA-MS results support the hypothesis that water causes reversible ring-opening as shown in Figure 4.9. The initiation of degradation involves hydrolysis and ring opening of the benzimidazole structure as the temperature approaches 225 °C. The presence of water lowers the activation energy for these reactions. For samples containing a large amount of mobile water, the impact of hydrolysis on the molecular structure and plasticization leads to a dramatic drop in storage moduli. Even more surprising is the detection of a rubbery plateau (Figures 4.4-4.6) in PBI above 500 °C. The rubbery plateau phenomenon is analogous to the one observed in cross-linked thermosets. The proposed hydrolysis and ring opening accompanied by cross-linking via amide interchange help explain the increase in storage moduli at temperatures above 280 °C. Structural changes associated with crosslinking can be readily detected by DMA. The water-saturated sample exhibits a rubber plateau modulus approximately 3 times lower than the one for the dry sample. This suggests the reaction products may vary significantly, depending on whether or not a significant amount of mobile water participates in the reaction. Additives or treatments designed to reduce hydrophilicity of PBI could offer property improvements, thus expanding the application for PBI under high temperature aqueous environments.

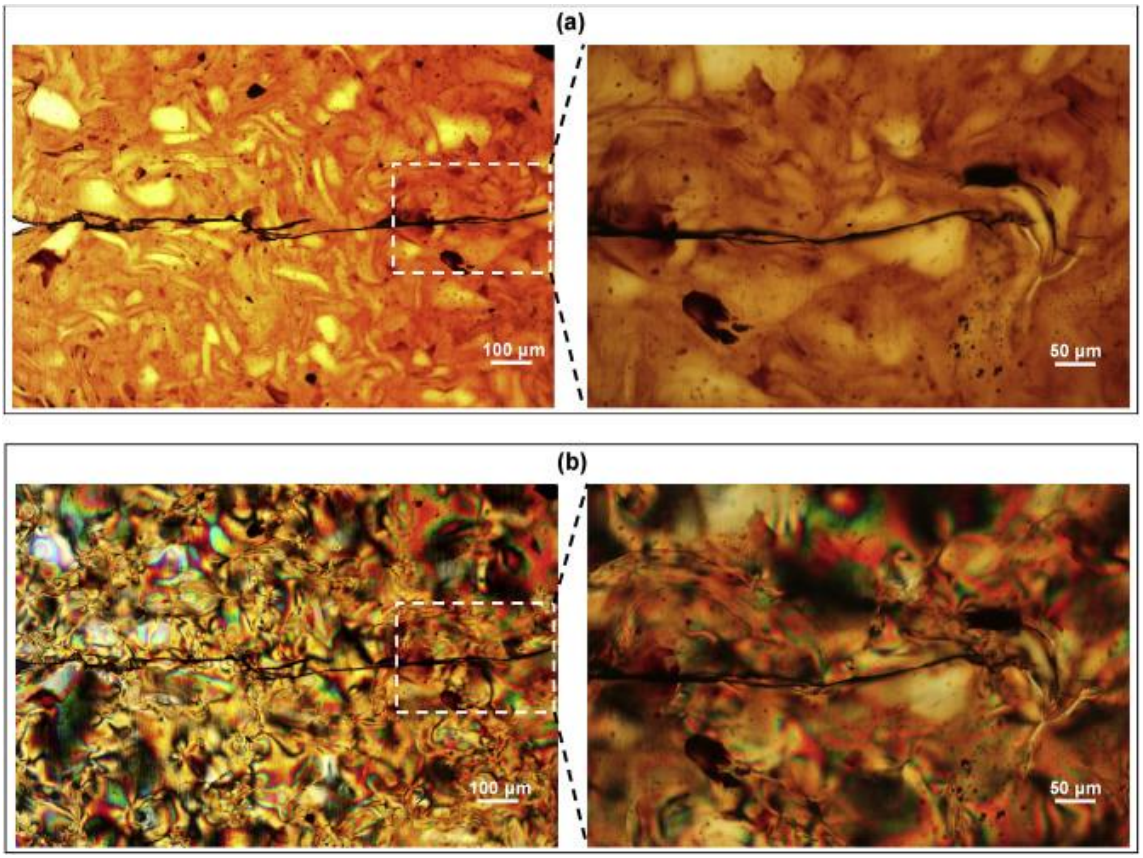

Figure 4.15. TOM images of the dry PBI DN-4PB specimen in the subcritical crack tip damage zone under (a) bright field and (b) cross-polarized light field. The crack propagates from left to right.

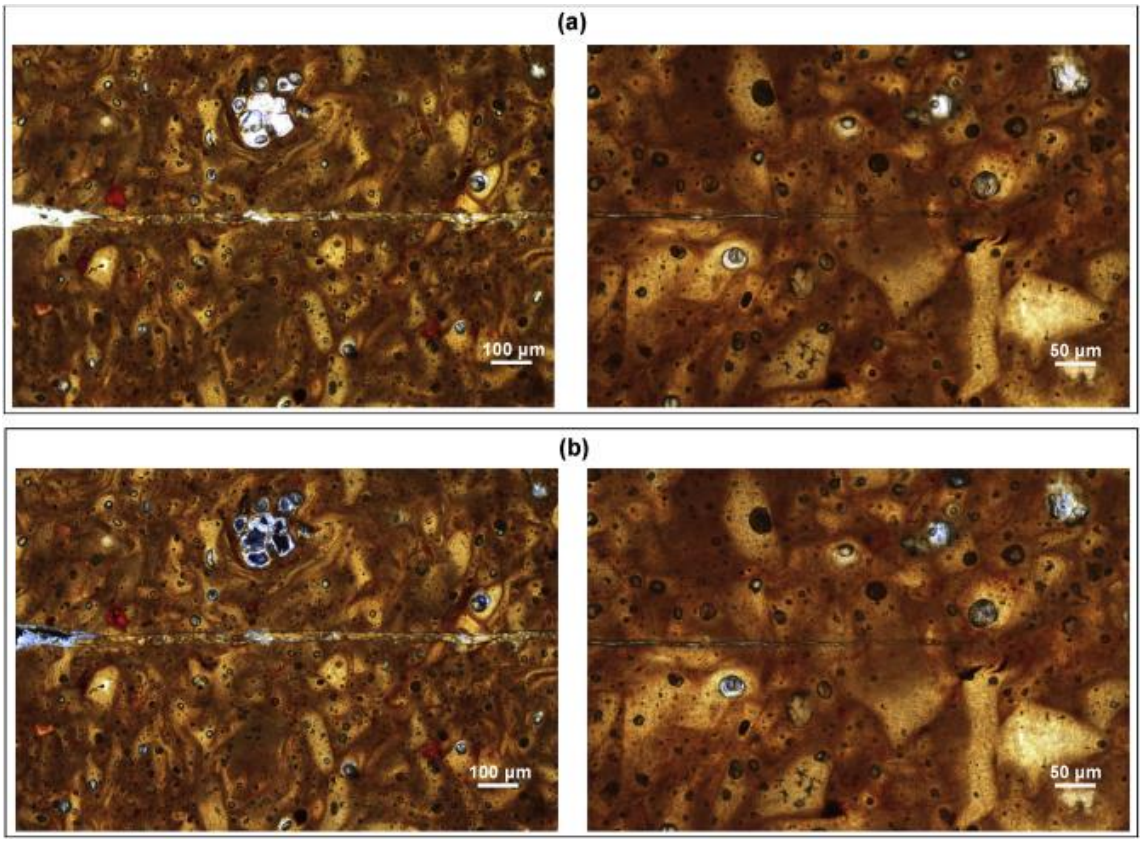

Figure 4.16. TOM images of the 288 °C hot water treated PBI DN-4PB specimen in the subcritical crack tip damage zone under (a) bright field and (b) cross-polarized light field. The crack propagates from left to right.

4.5 Conclusions

In this study we examined the behavior and degradation mechanism of PBI upon exposure to a comprehensive set of environmental exposure conditions for fundamental understanding of PBI degradation upon exposure to heat, water, and their combinations. The TGA-MS results show conclusively that the weight reduction below 300 °C is predominantly caused by desorption of water. A comparison was made among the DMA behaviors of PBI treated under different environmental exposures. With increasing temperatures, the PBI samples that contain water exhibit an initial decrease in storage

modulus, followed by a rapid increase of the storage modulus. The experimental findings support that both chain scission and crosslinking occur at high temperatures in the presence of water. Our study also shows that in dry condition, PBI exhibits relatively high fracture toughness. However, large scale plastic deformation is not observed around the crack tip. The high K_{IC} is primarily resulted from the inherently high fracture toughness of PBI. Unfortunately, the fracture toughness of PBI is significantly reduced after hot water exposure. Examination of the fracture process reveals the brittle fracture nature of the PBI is caused by hot water induced degradation of PBI molecules. It would be valuable to perform a systematic study with different powder sizes and sintering conditions to determine the influence of processing on final part properties.

CHAPTER V

INTERFACIAL AFFINITY AND FRACTURE BEHAVIOR OF POLY(ETHER ETHER KETONE) AND POLYBENZIMIDAZOLE BLENDS UNDER HYDROTHERMAL ENVIRONMENTS

5.1 Introduction

The strength of polymer-polymer interface is important for integrating polymeric components into devices. When two polymers of different compositions are blended, the properties of the resulting material critically depend on the degree of their compatibility. The compatibility of such blends may be promoted by strong secondary intermolecular forces, such as hydrogen bonding and dipole-dipole interactions. Polybenzimidazole (PBI) contains an N-H group that can form hydrogen bonds with other polymer chains, such as PEEK, that have heteroatoms. In this study, PBI particles (average size 50 μm) are blended as an inclusion phase with poly(ether ether ketone) to form a 50:50 weight ratio blend. The interfacial affinity between PEEK and PBI at various conditions has been systematically studied by dynamic mechanical analysis (DMA) and nanomechanical property mapping. In a dry condition, the T_g of the PEEK phase as well as the tan δ curve in the PEEK/PBI composite are identical to the respective values for neat PEEK. After being subjected to water immersion, the T_g of the PEEK phase in the PEEK/PBI blend shifts to lower temperature by 26 ºC, and the extent of this shift is much more significant than the observation from the soaked neat PEEK, which has served as a control. Nano-mechanical property mapping results indicate the relative

elastic modulus in the interfacial region of PEEK/PBI increased after water uptake. The observation strongly suggests the compatibility of PEEK and PBI is promoted by the formation of hydrogen bonding. Direct evidence of enhanced adhesion between PEEK and PBI after water immersion is demonstrated by the fracture behavior of the composite. The mechanisms that cause the property deterioration of the PEEK/PBI composite after hot water treatment are also discussed in this study.

5.2 Experimental

5.2.1 Materials

The material used in this study was melt blended PBI (MW=60,000 g/mol) with PEEK (melt viscosity is 350 Pa.s at 400 °C) with a weight ratio of 50:50. Both the PBI and PEEK resins were powders with particle sizes small enough to pass through a 100 mesh (0.147 mm) screen. The powders were heated to at least 170 °C in oven for 4 hours to ensure < 0.1 wt % water and volatiles. The powders were blended in a high speed mixer at 420 °C and then placed in a sealed mold to prevent exposure to air and moisture. This mixture was then compacted at ambient temperature under pressures of 5,000 - 20,000 psi (34,475 - 137,900 kPa) in a mold for at least 2 minutes. The pressure was released and the mold was heated to 420 °C for 4 - 24 hours. Pressures of 2,000-20,000 psi (13,790 - 137,900 kPa) were then reapplied while the mold was cooled. After the molding process, the material is further machined into the dimensions of 65mm × 3.175mm × 6.35mm.

5.2.2 Sample conditioning

Previous studies indicated that PBI has high affinity for water and it absorbs moisture even during sample handling[141, 148]. Drying processes were applied in this study to remove pre-existing moisture from the as-received samples. Moisture saturation of samples was carried out by immersion in deionized water at 60 °C to reach water saturation state. The moderate temperature was selected for the purpose of minimizing the possible degradation caused by heat. Immersion was determined to be completed when no additional weight gain was observed, usually after 10 days. Lastly, the 288 °C hot water treatment of samples was performed using a Parr pressure reactor (model 4913). PEEK/PBI plaques were confined in a steel wire cage that was fully immersed in water to stabilize the sample in a turbulent environment. The sample was then heated to 288 ºC in a pressure vessel with a resulting pressure of 1,100 psig. An adequate range of conditions were established to understand the individual effects of moisture and high temperature water exposure on the mechanical property deterioration of PEEK/PBI. For convenience, all the sample treatment conditions are summarized in Table 5.1.

Table 5.1. Sample treatment conditions.

Conditioning Histories	Temperature (ºC)	Time	Environment
Drying	110	12 Hours	762 mm. Hg vacuum
Water-saturation	60	7 days	Deionized water
Hot water treated	288	2 days	Hot Water

5.3 Results and Discussion

5.3.1 Dynamic mechanical behavior

In a polymer composite, stress transfer between the inclusion phase and the matrix upon deformation is critically dependent on the interface between the components. In a two-phase system, the interfacial strength dominates the performance of the blend. In some cases, this value can be directly measured. However, PEEK/PBI blends are unusual in that the PBI phase never melts during mixing and fabrication. Interactions between the two phases are formed between the molten PEEK and solid PBI. Factors such as particle size and applied shear rate during the melt compounding process will have an impact on the ultimate interfacial strength. As a result, a direct measurement of the adhesion strength between PEEK and PBI by a double cantilever beam test may give an arbitrary value, which deviates from the realistic scenario. Due to the temperature-dependent nature of relaxation time and activation energy for relaxation, the shape of the tan δ curve can provide detailed information on the state of the inclusion phase in matrix. Information regarding the variation of stress transfer at the interfacial region is known to be a reflection of the extent of interaction between the two components. DMA measurements are able to provide the above-mentioned information as well as a fundamental understanding on the viscoelastic nature of the blend as a whole. As for viscoelasticity, the measurements of transient phenomena such as stress relaxation and creep of the bulk sample are useful, while the damping behavior obtained by DMA is frequently more sensitive, allowing us to gain meaningful insight into

polymer chain motions and interactions at the molecular level. Most of our effort was concentrated on investigating the influence of the microstructure, especially the effect of the presence of water on the molecular chain relaxation of the PEEK/PBI blend. With this information, evidence-based predictions of the behavior of the blend as a bulk may be achieved. To obtain reliable result, a special drying process was applied in order to eliminate the effect of water that is absorbed from ambient environment, therefore a baseline of the samples in dry condition can be established.

The temperature dependence of storage modulus and tan δ for PEEK, PBI and PEEK/PBI 50:50 blend in dry condition are shown in Figure 5.1. The storage modulus of PEEK exhibits a significant drop at temperatures above T_g. Upon further temperature increase beyond T_g, the polymer chains in the amorphous phase gain higher mobility and are less constrained by surrounding chains. In between T_g and the melting transition, the amorphous regions between the lamellae begin to flow, as reflected by the progressively decreasing storage modulus of PEEK. By advantage of its high T_g of 427 °C, PBI is able to retain its storage modulus at elevated temperature. PEEK/PBI composites present nearly one order of magnitude increase in storage modulus compared to neat PEEK. This is commonly observed as an effect of the inclusion of rigid particles into the matrix.

In the dry state, the tan δ curve of the PEEK-PBI blend presents a transition peak at approximately 163 °C and can be largely attributed to the glass transition of PEEK alone (T_g = 165 °C). The tan δ of the PEEK alone and the PEEK/PBI blend are very similar in shape, implying the continuous PEEK phase dominates the damping behavior

of the blend in the dry condition. The temperature value corresponding to the α-relaxation process of PEEK component in the PEEK/PBI blend is not affected by the presence of PBI particles. However, the intensity of the tan δ peak at α-relaxation of PEEK in the blend is significantly suppressed, which is indicative of a reduction of chain segment mobility. It is worth pointing out that the full width half maximum (FWHM) of the tan δ peak at α-relaxation of PEEK with PBI is considerably broader than that of the neat PEEK. It is generally accepted that the α-relaxation is due to the large scale segmental motion during the glass-rubber transition. The FWHM of the tan δ peak at α-relaxation can be correlated to the temperature distribution at which the transition is activated. The area underneath the peaks can provide some insights about the overall amount of molecular segments involved in the relaxation process. To further explain these observations, we will henceforth discuss them jointly. Compared to the PEEK/PBI blend, the α-relaxation of the neat PEEK undergoes a steeper transition peak owing to the more flexible structure and less restricted molecular motion induced by the rigid PBI particles. Although the glass transition is generally thought of as a process associated only with the amorphous regions of the polymer, the effect of crystalline domains on this transition is well documented [167]. The presence of the PBI particles may have disrupted the crystallization kinetics of PEEK, therefore the chain folding process of PEEK might be hindered. As a result of this, the population of imperfect crystals or rigid amorphous phase may have increased. Because of the nature of the highly aromatic structure present in the PEEK backbone, the chain is relatively stiff. During crystallization from the melt, chains tend to form constrained higher rigid amorphous

structure or disordered small crystals. As a consequence, the double melting behavior is commonly observed in the DSC heating traces of PEEK samples [168]. The application of flash DSC technique revealed that the double melting behavior originates from the reorganization and recrystallization of the previously less-ordered structure upon acquiring higher mobility with heating. These recrystallized structures present thinner lamellar thickness and are subsequently melted with further increase temperature. An endothermic peak takes place at a lower temperature than the primary melting peak.

PBI has a tendency to absorb a significant amount of water. The effect of water absorption on the dynamic mechanical properties at various temperatures is of great interest for the blend system. It is first necessary to investigate the effect of water on each of the two components, which are PEEK and PBI, individually. As shown in Figure 5.2, the presence of water has a great effect on the dynamic mechanical behavior of PBI. As observed in the tan δ curve, PBI samples that contain water reveal new transition peaks appearing in the temperature regime between 200 °C to 300 °C. The prominent sub-Tg transition that is originally located at 240 °C has shifted to 25 °C. Water saturated PBI samples exhibit an initial decrease in storage modulus, followed by a rapid increase of the storage modulus. Our previous studies have demonstrated that both chain scission and crosslinking occur at high temperatures in the presence of water, which can account for the phenomenon mentioned above.

Rich and complex activities were detected in the tan δ curve of the PEEK/PBI blend in water-saturated condition. It can be clearly seen that, compared to the neat

PEEK, the α-transition derived from the PEEK matrix in PEEK/PBI blend presents decreased peak intensities accompanied by a downshift in temperature. The magnitude of the shift towards lower temperature is about 26 °C. The sub-T_g transition of PBI located in the temperature range between -50 °C to 120 °C can be partially superimposed onto the relaxation spectrum of the blend system. These phenomena have been commonly attributed to partial mixing between polymer phases [169]. It is worth noting that after subjection to 60 °C water immersion, PEEK reaches its water saturation content at about 0.5 wt%. This small amount of water has a marginal effect on the damping behavior of PEEK near the temperature regime of T_g as has been clearly shown in Figure 5.3. The majority of the water absorbed in the PEEK/PBI blend resides in the PBI component. In previous work it has been demonstrated with the use of NMR technique and a molecular model compound that water molecules can form hydrogen bonds with the N-H group of PBI [140, 170]. In the blend system, water molecules that are attached to the PBI can potentially form hydrogen bridges with the free electron pairs of the oxygen atom in the ether linkage of PEEK. However, previous studies have demonstrated that PBI shows a complex broad asymmetric N-H absorption in FTIR spectrum from 3100 to 3500 cm^{-1}, which makes it insufficient to validate the formation of hydrogen bonding between PEEK and PBI.

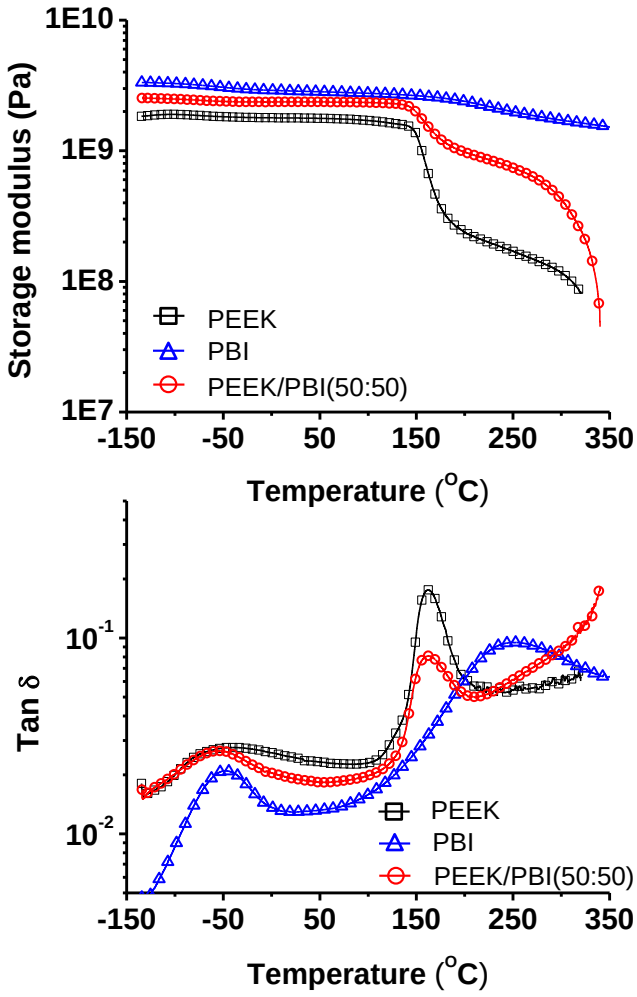

Figure 5.1. Temperature dependence of storage moduli and tan δ for PEEK, PBI and PEEK/PBI (50:50) blend in dry condition.

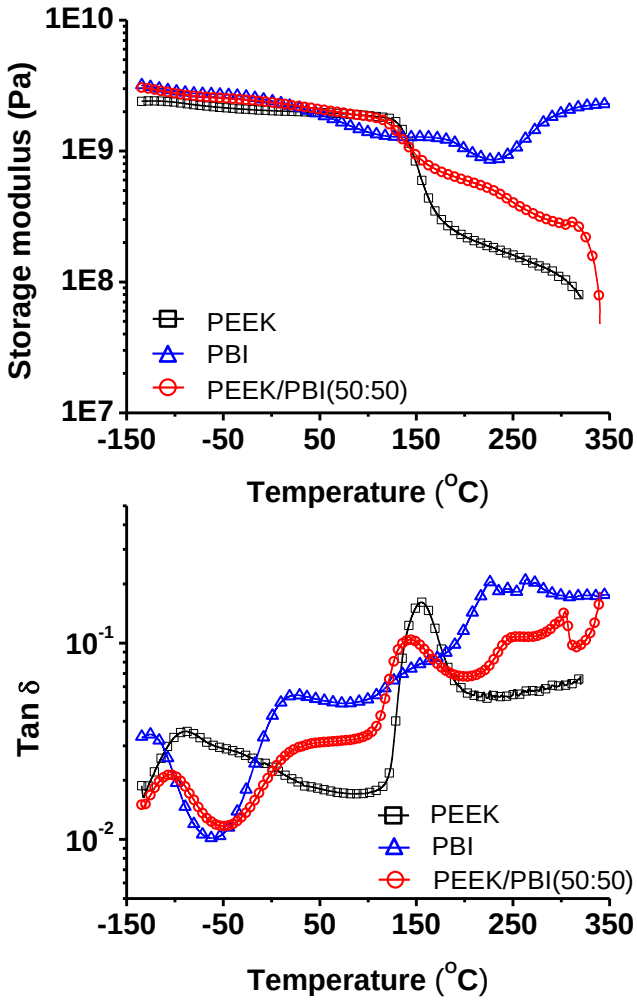

Figure 5.2. Temperature dependence of storage moduli and tan δ for PEEK, PBI and PEEK/PBI (50:50) blend in water-saturated condition. Sample conditioning was achieved by immersion in 60 ºC water. PEEK contains ~0.5 wt.% water, PBI contains ~12.5 wt.% water. PEEK/PBI blend contains ~5.5 wt.% water.

The temperature dependent dynamic mechanical behaviors of PEEK/PBI in three different conditions are shown in Figure 5.4. The influence of the incorporated water on the DMA behavior is examined by comparing the samples in dry condition and water-saturated condition. The storage moduli of the PEEK/PBI sample containing water are significantly lower than the one of the dry sample at temperatures above 0 ºC. The T_g of

the wet sample shifts notably by 26 °C to a lower temperature. To decouple the factors potentially contributing to this change in glass transition temperature, analysis begins with an investigation of the effects of the interactions between PEEK and water molecules. As has been shown in Figure 5.3, the absorption of 0.5 wt. % water by PEEK caused only a 5 °C downshift in T_g. Given this marginal effect, water absorption by PEEK can only account for a small portion of the observed 26 °C downshift in the T_g as observed in blend system. We therefore exclude this possibility and instead focus on the highly favored interactions between water and PBI as a potential influence on the T_g of the PEEK/PBI blend as well as the change in the interfacial behavior caused by the presence of water. It has been demonstrated by previous studies that polymer-polymer miscibility can be promoted by introducing new functional groups to the blend which can promote interactions between the blend components. Tg shift has been observed in the DMA results of systems that exhibit a higher degree of affinity between components. This phenomenon has been demonstrated by Deimede et al for a PBI and sulfonated poly(sulfone) blend, for which sulfonation of the chain backbone of poly(sulfone) promoted miscibility through an acid – base interaction[39]. Improved miscibility of the sulfonated system was confirmed by the observation of a well defined, single tan δ relaxation intermediate between those of the pure components. DMA showed that miscibility was strongly controlled by the degree of sulfonation as well as the blend composition. Even if the affinity between the inclusion phase and the matrix is high, the blend composition must reach a percolation threshold in order to cause a detectable T_g shift. This study highlights the importance of the amount of functional groups available

for forming secondary bonds that can enhance miscibility. Even for partially miscible systems, the higher-Tg blend component readily exhibits a reduced Tg.

The molecular damping behavior of the dry PEEK/PBI blend resembles the PEEK matrix in the dry state [5]. However, when water is present, the transition peak that is caused by the PBI component is revealed. Under the hydrothermal condition, water ingress into a polymer matrix leads to a range of effects. These effects include plasticization through interaction of the water molecules with polar groups in the matrix, creation of micro crazes through environmental stress cracking, leaching of unreacted monomer and hydrolysis of the polymer matrix. Relatively short times of exposure lead to reversible plasticization, producing a reduced glass transition temperature [9]. Particularly for PBI, the damping behavior depends critically on the amount of water absorbed. As shown in Figure 5.4, after the hot water treatment at 288 ºC, the storage moduli are further decreased. The observed temperature window at which the PEEK component experiences a glass transition is further broadened. The magnitude of this transition is also significantly suppressed, indicating the mobility of segmental motion is restricted. In a phase-separated system, a less symmetric band shape of the relaxation peak would be observed owing to the overlapping peaks from individual components. Given the results acquired at this current stage, it is premature to provide a definitive interpretation on the observed phase behavior of PEEK/PBI blend when significant amount of water is retained during the 288 ºC exposure. We will further explain the phenomenon made evident by our results in later sections of this chapter.

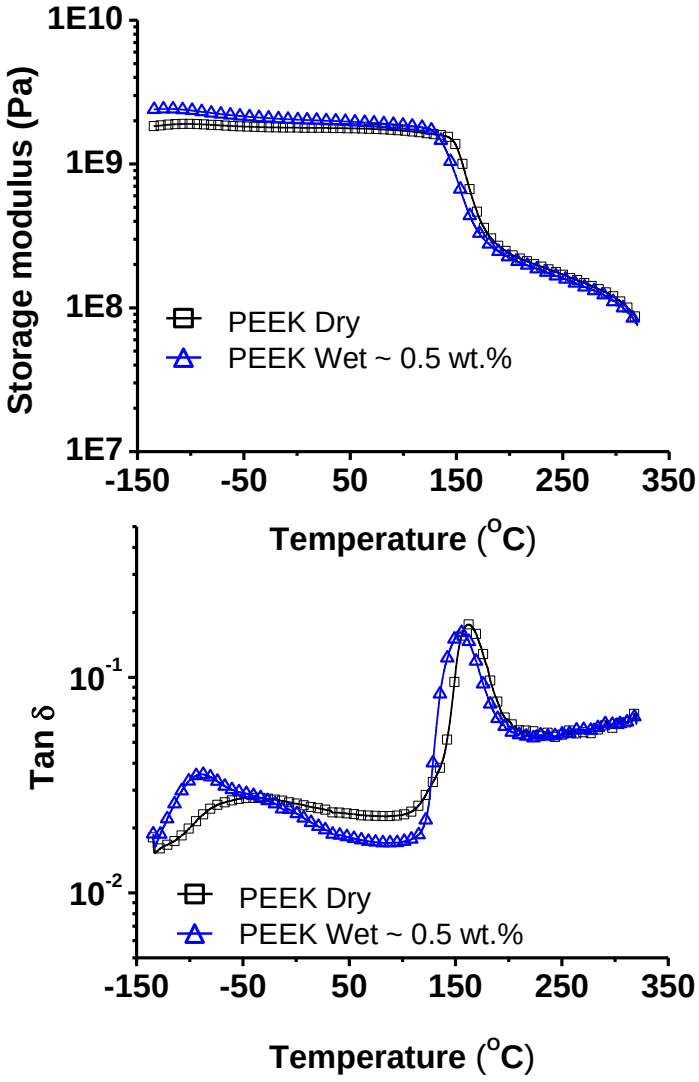

Figure 5.3. Temperature dependence of storage moduli and tan δ for PEEK in dry and wet conditions. Sample contains ≈ 0 wt.% water (dry condition), ≈ 0.5 wt.% water (60 ºC water-saturated condition).

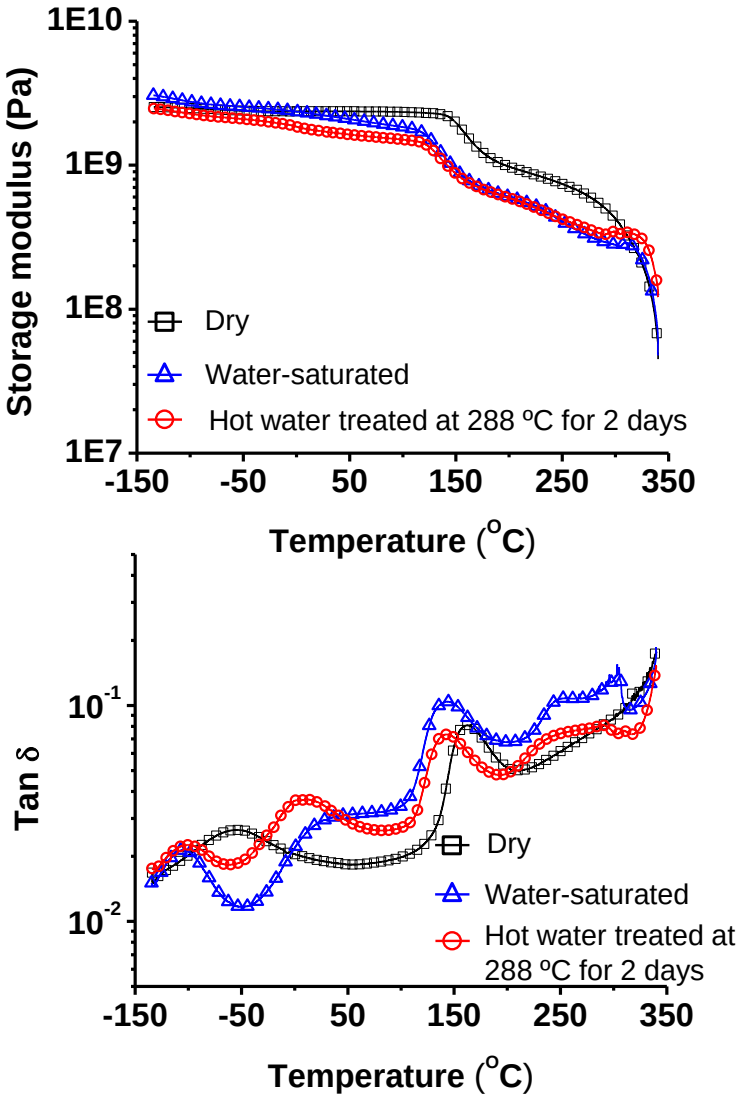

Figure 5.4. Temperature dependence of storage moduli and tan δ for PEEK/PBI (50:50) blend in dry, water-saturated and 288 ºC hot water treated conditions. Sample contains ≈ 0 wt.% water (dry condition), ≈ 5.5 wt.% water (water-saturated condition) and ≈ 5 wt.% water (2 days 288 ºC hot water treated condition).

5.3.2 AFM based PQM analysis

In recent years AFM-based techniques have been tailored to examine a variety of surface properties. While AFM imaging techniques impart valuable qualitative

information about the interface, they cannot be utilized to obtain quantitative measurements of surface properties. An AFM-based technique, PeakForce QNM, has been developed to achieve quantitative mapping of nanomechanical properties at the surface while simultaneously delivering topographical images at nanoscale resolution. PeakForce QNM may be used to map the elastic modulus, adhesion, dissipation, and deformation across a polymer surface. However, it has been demonstrated that employing a sharp probe for PeakForce QNM analysis gives an over-estimated, depth-dependent elastic modulus. This effect is most noticeable for soft materials for which the condition of stress-strain linearity is not met [53]. However, for a comparative study of rigid sample surfaces, this method is useful.

The results of PeakForce QNM analysis of the PEEK-PBI interface in the dry and steam-treated condition are given in Figure 5.5 and 5.6, respectively. The topographical images for PEEK-PBI blend in the dry condition show well-defined boundaries between the two phases. The measured elastic modulus has been normalized against our PEEK sample in dry condition for the purpose of obtaining comparative values. In the normalized elastic modulus vs. position curve, a sharp transition in elastic modulus is seen in the narrow interfacial region (~20 nm) between PEEK and PBI phases. In Figure 5.5, the boundary between PEEK and PBI phases is less distinct when compared to the previous image, suggesting enhanced phase penetration at the interface. This evidence is coherent to the numerical values presented in the normalized elastic modulus vs. position curve. A wider interfacial region of ~ 140 nm can be identified between the positions of 210 nm and 350 nm. Significantly, no sharp transition is

observed; rather, a broad curve has been mapped between the phase boundaries. In contrast to what has been observed for the untreated blend, this interfacial area demonstrates a higher elastic modulus than the adjacent individual components. The observation of this unique blend property implies that interaction between the blend components is promoted after the 288 °C hot water treatment.

Roe's work in extending the Flory-Huggins Theory has used an interaction parameter χ to specify the degree of interaction between two polymers in a system [32]. A larger χ value indicates a demixing of two polymers, for which each polymer component interacts mainly with segments of its own chain. This situation always leads to a narrow interface characterized by limited interactions between phases, as is seen for the PEEK-PBI blend in the dry condition. However, a negative χ value exemplifies a greater affinity between the blend components. Due to these favorable interpolymer interactions, the interface becomes highly diffuse and is characterized by enhanced incorporation of both polymer phases [32]. The resulting interfacial properties are not merely a combination of the two phases based on the rule of mixing; rather, the interfacial properties may exceed that of either individual phase, a situation which is represented by the steam-treated PEEK-PBI interface.

Extensive work in this area has revealed that secondary bonding, namely hydrogen bonding, dramatically enhances blend miscibility on the molecular level, and this promoted miscibility strongly influences the final T_g of the blend [41, 42, 44, 171].

Hydrogen bonding is a possible mechanism for the increased interfacial interaction observed between PEEK and PBI phases. The oxygen atoms of PEEK ketones may form such weak secondary forces with the hydrogen atoms of PBI amines. These non-covalent bonds constitute an interaction between the PEEK-rich phase and the PBI-rich phase and have a stabilizing effect on the interfacial region. Strengthening of the interface through hydrogen bonding may be one reason for the observed increase in interfacial elastic modulus. At this point, a consideration of the relative bonding energies characterizing carbonyl and amine bonds may aid our explanation of the preferential incorporation of water by the PBI component and the observed enhancement of the interfacial region. The carbonyl groups of the PEEK main chain and the amine groups of the PBI main chain are both strongly hydrophilic functional groups, yet in this study they appear to have exhibited very different behaviors upon exposure to water. The single N-H bonds of amine groups are characterized by bonding energies of ~391 kJ/mol, where this value represents the energy required to break a mole of single N-H bonds [172]. Carbonyl bonds are much stronger than amine bonds owing to their double bond character and greater polarity between component atoms. Greater polarity strengthens the degree of attraction between the carbon and oxygen atoms. With these advantages, carbonyl bonds boast bonding energies on the order of 745 kJ/mol, more than twice the value for atoms bonded in an amine group [172]. Hydrogen bonding between water molecules and the carbonyl and amine groups of the PEEK and PBI chains, respectively, requires a transient breakage of these bonds. In the case of PEEK, this will require significant energy owing to the strength of the carbonyl bond. For PBI

amine groups, hydrogen bonding is a more favorable interaction because it requires a relative smaller energy cost. Furthermore, the main chain repeat unit of PBI contains four hydrogen bonding sites, while the PEEK main chain has one carbonyl group and thus one potential hydrogen bonding site per repeat unit.

The formation of hydrogen bonds between PBI amine groups and water molecules can aid in our interpretation of the AFM result. Swelling of PBI particles due to water uptake could amplify the interfacial stress. Consequently, a greater interfacial elastic modulus would be observed across the region. PBI particle swelling could likewise increase the size of the interfacial region.

Swelling-induced stress at the interface is another possible explanation for the observed increase in interfacial elastic modulus. The uptake of water by PBI particles will cause them to increase in volume, and one result of this swelling will be amplification of interfacial stress. Consequently, a greater elastic modulus will be observed across this region. Crosslinking may also be responsible for the increased interfacial elastic modulus. By providing covalent connections between PBI molecules, crosslinking strengthens and stabilizes the interface.

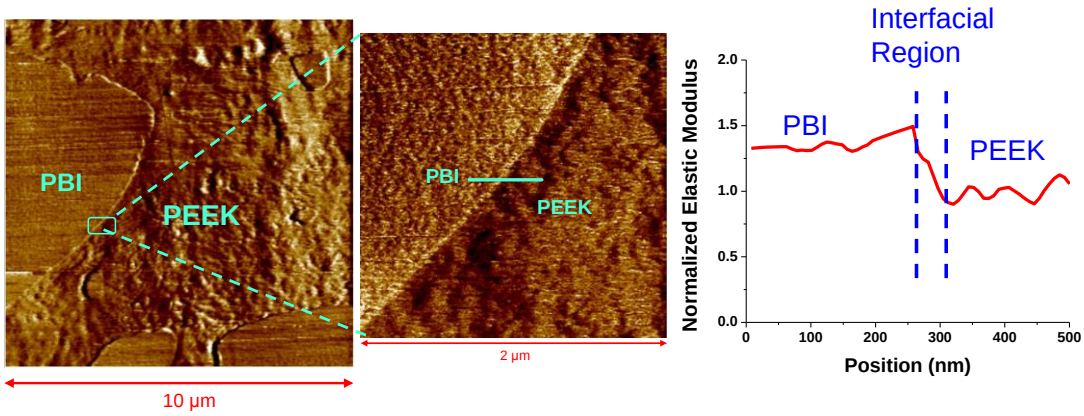

Figure 5.5 Quantitative mapping of relative elastic moduli at interface of PEEK and PBI in dry condition.

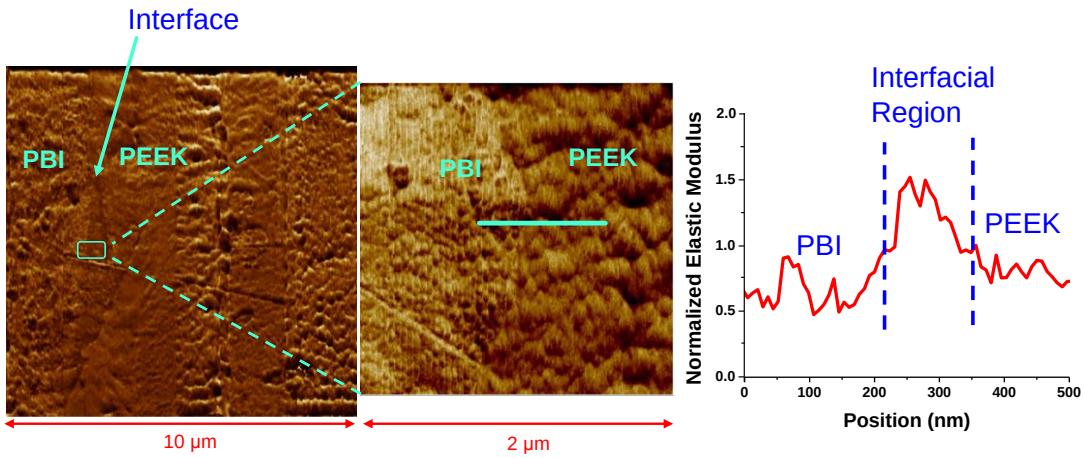

Figure 5.6 Quantitative mapping of elastic moduli at interface of PEEK and PBI after hot water treated at 288 ºC for 2 days.

5.3.3 Uniaxial tensile behavior

The representative tensile stress versus strain curves for all the samples are presented in Figure 5.7 for comparison. The representative tensile properties are listed in Table 5.2. The water-saturated PEEK/PBI exhibits a lower modulus than dry PBI. The decrease in modulus is due to the plasticization effect by the water molecules. The elongation at break is significantly increased for the water-saturated sample. This

observation indicates that a moderation water immersion process does not cause the generation of defects in the PEEK/PBI. Other than causing the debonding between PBI particles and PEEK matrix, the water servers to strength the adhesion between the two components, as evident by the increased elongation at break. However, after the samples were conditioned in 288 ºC hot water environment for 2 days at 288 ºC, the fracture toughness and ductility decreased significantly.

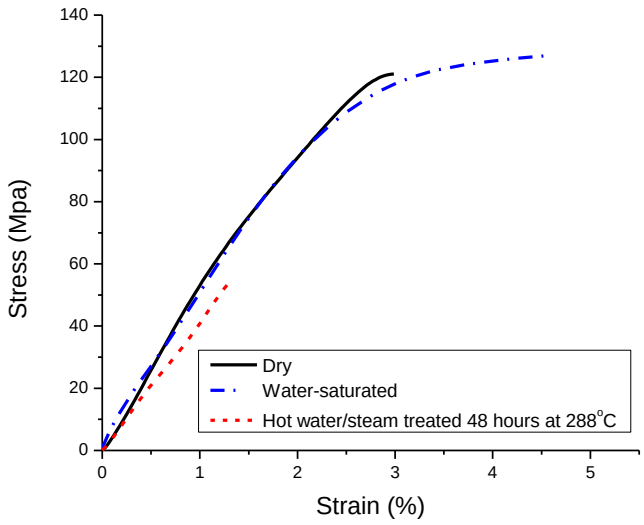

Figure 5.7. Typical stress-strain curves of PEEK/PBI blends treated under different conditions.

5.3.4 Fracture behavior

To carry out fracture behavior study on the PEEK/PBI blend, it is necessary first to examine how the PEEK and PBI individually will respond environmental conditioning. PEEK is regarded as an inherently tough material. A significant body of

work has been devoted to determining fracture toughness value of PEEK under various testing conditions [173, 174]. Certain criteria must be met to ensure that the measured values are independent of sample geometry. It has been shown that the K_{IC} value of PEEK drops from 8.7 to 7.0 MPa×$m^{1/2}$ for a specimen thickness of 1.9 mm and 5.3 mm, respectively [174]. It has also been demonstrated that the fracture toughness of PEEK is rate dependent [173]. In our current study, the specimens have a thickness of 6.35 mm. A testing rate of 1.25 mm/min was selected for the single-edge-notch three-point-bend (SEN-3PB) tests. The fracture toughness results of PEEK in three different conditions are shown in Figure 5.8. The results indicate that the 288 ºC hot water treatment embrittles the PEEK, causing the K_{IC} value to drop from 7.1 to 3.5 MPa·$m^{1/2}$. Karger-Kocsis and Friedrich demonstrates that the fracture surface of PEEK shows an apparent stress whitening zone when tested at a deformation rate of 1 mm/min [173]. This observation suggests that during the fracture of PEEK, significant amount of plastic flow has taken place prior to final fracture. To further investigate into the fracture behavior of PEEK, as well as learning the effects of hot water exposure on fracture process, the DN-4PB test was employed to reveal the fracture mechanisms of PEEK in different conditions. The TOM images of the sub-critical crack of PEEK in dry condition and after 288 ºC hot water treatment are shown in Figure 5.9. It can be observed that the PEEK in dry condition shows massive crazing. On the other hand, the crazing phenomenon in the 288 ºC hot water treated sample significantly diminishes. Formation of crazes and the resultant craze density are directly related to fracture resistance. Our previous study shows that PBI has a fracture toughness value of 2.86 MPa·$m^{1/2}$ in dry

condition[52]. Although PBI can absorb a significant amount of water, the water content alone does not affect fracture toughness much. However, the fracture toughness value of PBI is greatly reduced after the 288 °C hot water exposure, suggesting molecular scale degradation has taken place.

Adding PBI to PEEK results in better preservation of elasticity and shape stability upon exposure to elevated temperature. An equally important question is that of the mechanical properties. Previous studies have shown that poor filler-polymer matrix interaction leads to low fracture toughness, which greatly limits their engineering applications. In addition to that, it is of great interest to examine the mechanical performance change after a certain period of time of exposure to the hydrothermal environment. These complex morphologies, as well as the divergence between the mechanical properties of the two phases, can result in complicated stresses, strains, and fracture phenomena within the blend. It is necessary to examine how the PEEK alone will respond when it is subjected to the same environmental conditioning. PEEK is regarded as an inherently tough material. A significant body of work has been devoted to acquiring the geometry independent intrinsic toughness value of PEEK. Certain criteria must be imposed to ensure that the measured values are independent to the geometry. Among these criteria, a sufficient specimen thickness is critical to satisfy the plane strain condition which is required for conducting linear elastic fracture mechanics analysis. Wu's work has shown that the measured K_{IC} value drops from 8.7 $MPa \times m^{1/2}$ to 7.0 $MPa \times m^{1/2}$ for a specimen thickness of 1.9 mm and 5.3 mm, respectively [174]. It has also been demonstrated that the fracture of PEEK appears to be rate dependent [173].

PEEK samples appear to be more brittle when a testing rate of 100 mm/min is applied. In our current study, specimen have a thickness of 6.35 mm. A testing rate of 1.25 mm/min was selected for the single-edge-notch three-point-bend (SEN-3PB) tests. The fracture toughness results of PEEK, PBI and PEEK/PBI 50:50 composites are shown in Figure 5.8. From the morphological observation, the crack propagates along the interface of PEEK and PBI under dry condition as shown in Figure 5.10. The interfacial adhesion between PEEK and PBI appears to be enhanced upon exposure to water as evidenced by crack propagation through the PBI particles. It is also possible that the cohesive strengths of PEEK and PBI were greatly reduced. However, this is unlikely since neither the fracture toughness value of PEEK nor that of PBI is reduced in water-saturated condition. As has been shown in the AFM-QMN results, the width of the interface between PEEK and PBI in dry condition is quite small, and it is reasonable to postulate that limited interaction is formed in this region. The effective width of the interface is increased by the penetration of the PEEK and PBI at the interface when water is present. It gives rise to an increased interfacial strength as has been verified by direct measurement of fracture values and two distinct characteristics of crack propagation.

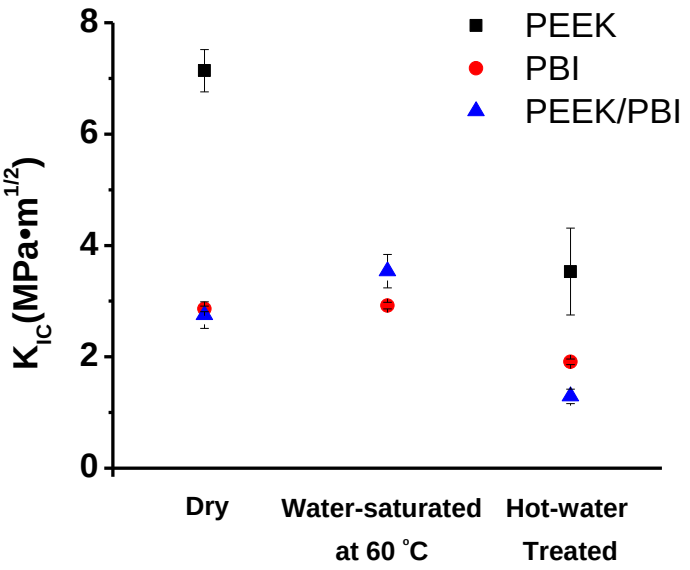

Figure 5.8. K_{IC} of PEEK, PBI and PEEK/PBI in different conditions.

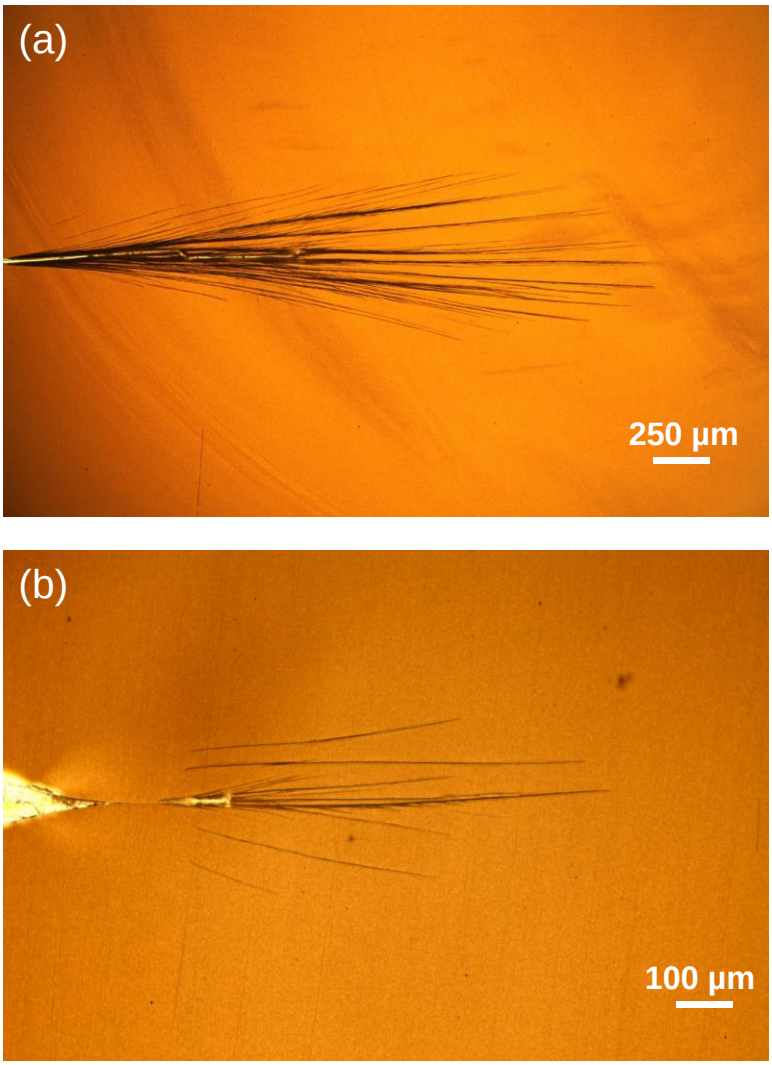

Figure 5.9. TOM images of the dry PEEK DN-4PB specimen in the subcritical crack tip damage zone under (a) dry sample (b) 288 °C hot water treated sample. The crack propagates from left to right.

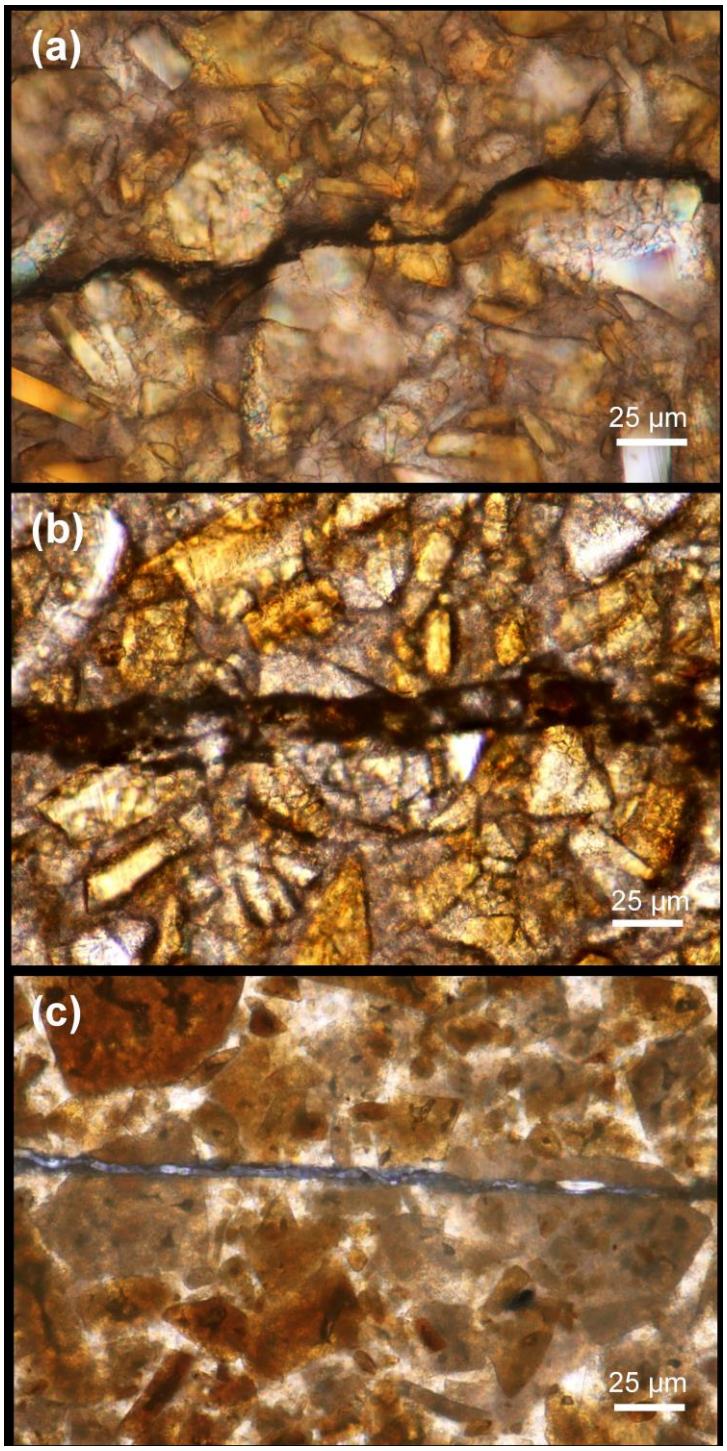

Figure 5.10. Crack propagations in PEEK/PBI. (a) Dry condition. (b) Water-saturated condition. (c) After hot water/steam treatment at 288 ºC for 2 days.

Table 5.2. Summary of fracture toughness and tensile properties of PEEK/PBI treated under different conditions.

Conditioning Histories	K_{IC} (MPa*$m^{1/2}$)	E (GPa)	σ (MPa)	ε_B (%)
Dry	2.7 ± 0.2	5.4 ± 0.2	122 ± 15	2.9 ± 0.3
Water-saturated	3.5 ± 0.3	4.8 ± 0.1	127 ± 10	4.7 ± 0.4
288 °C Hot water treated	1.2 ± 0.1	4.0 ± 0.2	56 ± 8	1.3 ± 0.2

The mechanical properties of PEEK such as tensile strength, elongation at break and impact strength for a particular polymer blend vary with the morphology and the crystallinity. PEEK used in the current study has a crystallinity of 39% as determined by DSC. During the crystallization of PEEK, once a sample has been cooled to a temperature below the melting temperature, a combination of the thermodynamics and kinetics dominates the process of chain organization and subsequent formation into higher order crystal domains. This mechanism may have resulted in two different molecular morphologies in terms of how the crystallites and amorphous region are spatially arranged with the PBI particles. One possibility is that crystal domains of PEEK segregate from the amorphous phase, resulting in an increased content of PBI in the remaining amorphous phase of the blend. The other possibility is that PBI serves as an initiation site for crystallization of PEEK. Essentially, PBI particles provide the surface or site to reduce the free-energy barrier associated with achieving the critical nucleus. As a result of this, PBI particles will be in closer proximity to the crystal domains than the amorphous domains. For some of the high crystallinity polymers, for instance linear polyethylene, this kind of spherulitic arrangement can be better revealed by electron microscopy. Strict analysis of molecular arrangements with polymer crystal

yields detailed electron micrograph of lamellar structure as observed in melt crystallized linear polyethylene. The micrograph reveals strong evidence of the state of polymer chains in the crystalline texture. This method is, however, not adequate in the case of PEEK. Morphological investigations have not completely clarified the understanding of the chain folding process of PEEK. In spite of that, they demonstrate that PEEK crystals are unique compared to those of more flexible polymers. When crystallized either from the melt or from solutions, lamellae are narrow and febrile instead of the more typical fully developed spherulite shape. The spatial arrangement of the PEEK crystallites is compact as revealed by limited morphological evidence. According to previous studies on melt blended PEEK and poly(ether imide), the two polymeric components are compatible in the melt, and phase separation occurs during crystallization of the PEEK component [175]. The morphological observation and electron scattering reveal the PEEK crystal domains separate from the miscible amorphous phase, resulting in a PEI rich phase in the remaining amorphous region of the blend. Given the size of the PBI particle, which is on the order of 50 μm, it is more likely the case that PBI particles will be excluded from the lamellar structure. Compared to an arrangement in which crystal domains are directly connected to PBI particles, the presence of an amorphous region surrounding the PBI particles will allow water to more easily diffuse and reside. This could support the feasibility of a layered structure having compositional gradients that present a transition from PBI rich phase to PEEK rich phase. This paper is not intended to assess the effect of the presence of PBI on the crystallization behavior of PEEK. Rather, it is intended to investigate the behavior of the current system that is processed

under the given condition as mentioned above, and the overall performance variation of the blend compared to neat PEEK.

5.4 Conclusions

In this study, the interfacial affinity of a 50:50 wt. PEEK/PBI blend in a hygrothermal environment has been assessed. We have quantified the deterioration of mechanical properties, including fracture toughness and tensile behavior, induced by hygrothermal exposure. DMA was employed to examine the effect of water immersion on the damping behavior of the PEEK/PBI blend. In dry condition, the damping behavior of the PEEK/PBI blend is dominated by the PEEK phase. With the presence of water, the sub-Tg transition of the PBI superimposes itself onto the tanδ curve of the blend. A significant Tg shift is observed, suggesting enhanced interaction between the polymer phases. The results of AFM-QNM analysis provide the evidence of an expanded interfacial region for the PEEK/PBI blend after water uptake. Enhanced adhesion between PEEK and PBI after water immersion is also demonstrated by the fracture behavior of the composite. Hydrogen bonding between water molecules and PBI has been implicated for enhancing phase penetration, consequently expanding the PEEK-PBI interface as evidenced by the AFM-QNM result. Future work in this area will focus on reducing water uptake in PBI by selecting an alternative chemical structure.

CHAPTER VI

CONCLUSIONS AND FUTURE WORKS

6.1 Summary

Translation of microscale properties into bulk response is of significant interest to the nanomaterials community and is prerequisite to the use of nanomaterials for commercial applications. Obstacles to this goal are mainly associated with experimental discrepancies involving poor, inconsistent dispersion of nanomaterials, as well as a dearth of experimental tools capable of effectively characterizing interactions between nanoscale anisotropic materials. This dissertation described a reliable method for CNT dispersion in organic solvents and polymers, and this dissertation has discussed recent efforts to establish a comprehensive basis for understanding behavior of PP/CNT nanocomposite. We have also highlighted hybrid composites as a potential new field of study due to the ability of nanomaterials of different geometries to interact with a matrix across distinct length scales, although control of dispersion will also be essential for progress in this field.

One aspect of this dissertation work focus on one area of technology that is in fact growing in importance to the challenging imposed by the rising demand for the polymeric materials that can withstand harsh environments. As thermal, pressure and corrosive conditions become more demanding the likelihood that one polymer will be able to perform as a structural material under high temperature conditions is becoming problematic. Innovative polymeric blend approaches using multiple materials seem to be

promising. The most popular and rapidly growing base polymer material for these applications comes from the polyaryletherketone (PAEK) family of polymers, namely the polyetheretherketone (PEEK) type. This semi-crystalline material has many desirable features when compared to the current hierarchy of commercial, high performance thermoplastics, in low chemical reactivity, high corrosion resistance in acidic and caustic environments, high modulus, and high glass transition temperature and crystalline melting point. A critical aspect of this material from the perspective of engineering design and risk management is the durability of the component in service at these upper end limits of the material capability. In order to provide higher confidence in the lifetime of this material, it is critical that we bring understanding to the fundamental mechanisms of the property deterioration events that ultimately dictate useful service life. These events may be contributed to from a number of fundamental features of the polymer system that are cumulatively and generically termed "degradation", but can include such processes as thermal degradation, thermo-oxidative degradation, dynamic fatigue, thermal fatigue, physical processes (liquid absorption, leaching etc). To say the least, the mechanisms of degradation are poorly understood, and it is difficult to predict lifetimes under various conditions. The engineering, environmental and social risks are too great to ignore this gap in the science and engineering associated with better understanding how these polymers behave in prolonged service.

This dissertation work describes the mechanisms of degradation and the factors contributing to service life reduction of PEEK/PBI. The focus is on the mechanisms of mechanical property deterioration caused by heat and water.

6.2 Concluding Remarks and Future Work

Fundamental structure-property relationships of polymer matrix with solid inclusion phase were investigated. Overall, fundamental detail achieved in this work is significant compared to other works. This study is also critical for potential future application of polymer composites and blends.

Further investigation of the reinforcement effect of the individually dispersed MWCNT towards different types of polypropylene (isotactic polypropylene and syndiotactic polypropylene) are of interest to show the influence of different PP chain architecture and crystallinity.

Further investigation of the PEEK/PBI will be directed to using PBI with different chemical structure for the purpose of reducing the water uptake which has been determined to be the primary reason of causing property deterioration. In this dissertation work, the samples were conditioned in hot water (288 °C) then tested and analyzed under ambient conditions. Given the wide range of conditions ('sour gas' (H_2S), pH, metal ions, oxygen concentration, temperature) that PEEK/PBI is used by industry, this study does not shed light on all of the environmental factors that may impact field lifetimes. Research related to the influence of these additional factors will be left for the future.

REFERENCES

[1] D. Sun, W.N. Everett, C.C. Chu, H.J. Sue, Single‐Walled carbon‐nanotube dispersion with electrostatically tethered nanoplatelets, Small 5(23) (2009) 2692-2697.

[2] L.P. DISano, Thermoplastic materials and designs for ultra high temperature environments, High Performance Thermoplastics & Composites for Oil and Gas Applications (2011).

[3] H.H. Levine, Encyclopedia of polymer science and technology, Wiley-Interscience, New York 10 (1969).

[4] M. Cadek, J. Coleman, V. Barron, K. Hedicke, W. Blau, Morphological and mechanical properties of carbon-nanotube-reinforced semicrystalline and amorphous polymer composites, Applied physics letters 81(27) (2002) 5123-5125.

[5] A.C. Balazs, T. Emrick, T.P. Russell, Nanoparticle polymer composites: where two small worlds meet, Science 314(5802) (2006) 1107-1110.

[6] C.B. Bucknall, I.K. Partridge, Phase separation in epoxy resins containing polyethersulphone, Polymer 24(5) (1983) 639-644.

[7] C.W. Macosko, Morphology development and control in immiscible polymer blends, Macromolecular Symposia, Wiley Online Library, 2000, pp. 171-184.

[8] S. Hobbs, M. Dekkers, V. Watkins, Morphology and properties of toughened poly (phenylene oxide)-polyamide blends, Journal of materials science 24(6) (1989) 2025-2030.

[9] P. Subramanian, Permeability barriers by controlled morphology of polymer blends, Polymer Engineering & Science 25(8) (1985) 483-487.

[10] M. Kawasumi, N. Hasegawa, M. Kato, A. Usuki, A. Okada, Preparation and mechanical properties of polypropylene-clay hybrids, Macromolecules 30(20) (1997) 6333-6338.

[11] H.G. Premalal, H. Ismail, A. Baharin, Comparison of the mechanical properties of rice husk powder filled polypropylene composites with talc filled polypropylene composites, Polymer Testing 21(7) (2002) 833-839.

[12] M. Huda, L. Drzal, A. Mohanty, M. Misra, The effect of silane treated-and untreated-talc on the mechanical and physico-mechanical properties of poly (lactic

acid)/newspaper fibers/talc hybrid composites, Composites Part B: Engineering 38(3) (2007) 367-379.

[13] T. Kietzke, D. Neher, K. Landfester, R. Montenegro, R. Güntner, U. Scherf, Novel approaches to polymer blends based on polymer nanoparticles, Nature materials 2(6) (2003) 408-412.

[14] W. Bauhofer, J.Z. Kovacs, A review and analysis of electrical percolation in carbon nanotube polymer composites, Composites Science and Technology 69(10) (2009) 1486-1498.

[15] L. Dai, D.W. Chang, J.B. Baek, W. Lu, Carbon nanomaterials for advanced energy conversion and storage, Small 8(8) (2012) 1130-1166.

[16] L. Guadagno, L. Vertuccio, A. Sorrentino, M. Raimondo, C. Naddeo, V. Vittoria, G. Iannuzzo, E. Calvi, S. Russo, Mechanical and barrier properties of epoxy resin filled with multi-walled carbon nanotubes, Carbon 47(10) (2009) 2419-2430.

[17] T.-S. Chung, L.Y. Jiang, Y. Li, S. Kulprathipanja, Mixed matrix membranes (MMMs) comprising organic polymers with dispersed inorganic fillers for gas separation, Progress in Polymer Science 32(4) (2007) 483-507.

[18] C.-C. Chu, K.L. White, P. Liu, X. Zhang, H.-J. Sue, Electrical conductivity and thermal stability of polypropylene containing well-dispersed multi-walled carbon nanotubes disentangled with exfoliated nanoplatelets, Carbon 50(12) (2012) 4711-4721.

[19] P. Liu, K.L. White, H. Sugiyama, J. Xi, T. Higuchi, T. Hoshino, R. Ishige, H. Jinnai, A. Takahara, H.-J. Sue, Influence of trace amount of well-dispersed carbon nanotubes on structural development and tensile properties of polypropylene, Macromolecules 46(2) (2013) 463-473.

[20] X. Zhang, H.-J. Sue, R. Nishimura, Electrostatically controlled isolation of debundled single-walled carbon nanotubes from nanoplatelet dispersant, Journal of Materials Chemistry 22(13) (2012) 6156-6164.

[21] K.L. White, M. Shuai, X. Zhang, H.-J. Sue, R. Nishimura, Electrical conductivity of well-exfoliated single-walled carbon nanotubes, Carbon 49(15) (2011) 5124-5131.

[22] D. Sun, C.-C. Chu, H.-J. Sue, Simple approach for preparation of epoxy hybrid nanocomposites based on carbon nanotubes and a model clay, Chemistry of Materials 22(12) (2010) 3773-3778.

[23] K.L. White, H.J. Sue, Electrical conductivity and fracture behavior of epoxy/polyamide‐12/multiwalled carbon nanotube composites, Polymer Engineering & Science 51(11) (2011) 2245-2253.

[24] K.L. White, H.-J. Sue, Delamination toughness of fiber-reinforced composites containing a carbon nanotube/polyamide-12 epoxy thin film interlayer, Polymer 53(1) (2012) 37-42.

[25] M.M. Hossain, E. Moghbelli, E. Jahnke, P. Boeckmann, S. Guriyanova, R. Sander, R. Minkwitz, H.-J. Sue, Rubber particle size and type effects on scratch behavior of styrenic-based copolymers, Polymer 63 (2015) 71-81.

[26] N. Priyadarshani, C.W. Benzine, B. Cassidy, J. Suriboot, P. Liu, H.-J. Sue, D.E. Bergbreiter, Polyolefin soluble polyisobutylene oligomer-bound metallophthalocyanine and azo dye additives, Journal of Polymer Science Part A: Polymer Chemistry 52(4) (2014) 545-551.

[27] K.R. Shull, E.J. Kramer, G. Hadziioannou, W. Tang, Segregation of block copolymers to interfaces between immiscible homopolymers, Macromolecules 23(22) (1990) 4780-4787.

[28] E. Helfand, Y. Tagami, Theory of the interface between immiscible polymers, Journal of Polymer Science Part B: Polymer Letters 9(10) (1971) 741-746.

[29] E. Helfand, Y. Tagami, Theory of the interface between immiscible polymers. II, The Journal of Chemical Physics 56(7) (1972) 3592-3601.

[30] D. Broseta, G.H. Fredrickson, E. Helfand, L. Leibler, Molecular weight and polydispersity effects at polymer-polymer interfaces, Macromolecules 23(1) (1990) 132-139.

[31] D. Patterson, A. Robard, Thermodynamics of polymer compatibility, Macromolecules 11(4) (1978) 690-695.

[32] R.J. Roe, Theory of the interface between polymers or polymer solutions. I. Two components system, The Journal of Chemical Physics 62(2) (1975) 490-499.

[33] G. Crevecoeur, G. Groeninckx, Binary blends of poly (ether ether ketone) and poly (ether imide): miscibility, crystallization behavior and semicrystalline morphology, Macromolecules 24(5) (1991) 1190-1195.

[34] H.R. Brown, Effect of a diblock copolymer on the adhesion between incompatible polymers, Macromolecules 22(6) (1989) 2859-2860.

[35] C. Creton, E.J. Kramer, C.Y. Hui, H.R. Brown, Failure mechanisms of polymer interfaces reinforced with block copolymers, Macromolecules 25(12) (1992) 3075-3088.

[36] T. Ge, G.S. Grest, M.O. Robbins, Structure and strength at immiscible polymer interfaces, ACS Macro Letters 2(10) (2013) 882-886.

[37] S. Wu, Surface and interfacial tensions of polymer melts. II. Poly (methyl methacrylate), poly (n-butyl methacrylate), and polystyrene, The Journal of Physical Chemistry 74(3) (1970) 632-638.

[38] A. Walther, K. Matussek, A.H. Muller, Engineering nanostructured polymer blends with controlled nanoparticle location using Janus particles, Acs Nano 2(6) (2008) 1167-1178.

[39] V. Deimede, G. Voyiatzis, J. Kallitsis, L. Qingfeng, N. Bjerrum, Miscibility behavior of polybenzimidazole/sulfonated polysulfone blends for use in fuel cell applications, Macromolecules 33(20) (2000) 7609-7617.

[40] G. Adams, J. Cowie, Blends of rigid and flexible macromolecules: poly (benzimidazole) mixed with poly (vinyl acetate-stat-vinyl alcohol) copolymers, Polymer 40(8) (1999) 1993-2001.

[41] X. Lu, R. Weiss, Development of miscible blends of polyamide-6 and manganese sulfonated polystyrene using specific interactions, Macromolecules 24(15) (1991) 4381-4385.

[42] T.-K. Ahn, M. Kim, S. Choe, Hydrogen-bonding strength in the blends of polybenzimidazole with BTDA-and DSDA-based polyimides, Macromolecules 30(11) (1997) 3369-3374.

[43] D. Paul, J. Barlow, A binary interaction model for miscibility of copolymers in blends, Polymer 25(4) (1984) 487-494.

[44] W. Stockton, M. Rubner, Molecular-level processing of conjugated polymers. 4. Layer-by-layer manipulation of polyaniline via hydrogen-bonding interactions, Macromolecules 30(9) (1997) 2717-2725.

[45] E.J. Moskala, S.E. Howe, P.C. Painter, M.M. Coleman, On the role of intermolecular hydrogen bonding in miscible polymer blends, Macromolecules 17(9) (1984) 1671-1678.

[46] S. Jiang, A. Göpfert, V. Abetz, Novel morphologies of block copolymer blends via hydrogen bonding, Macromolecules 36(16) (2003) 6171-6177.

[47] P. Cebe, S.-D. Hong, Crystallization behaviour of poly (ether-ether-ketone), Polymer 27(8) (1986) 1183-1192.

[48] S.J. Zaidi, S. Mikhailenko, G. Robertson, M. Guiver, S. Kaliaguine, Proton conducting composite membranes from polyether ether ketone and heteropolyacids for fuel cell applications, Journal of Membrane Science 173(1) (2000) 17-34.

[49] G. Guerra, S. Choe, D.J. Williams, F.E. Karasz, W.J. MacKnight, Fourier transform infrared spectroscopy of some miscible polybenzimidazole/polyimide blends, Macromolecules 21(1) (1988) 231-234.

[50] L. Leung, D.J. Williams, F.E. Karasz, W.J. MacKnight, Miscible blends of aromatic polybenzimidazoles and aromatic polyimides, Polymer Bulletin 16(5) (1986) 457-464.

[51] P. Musto, F.E. Karasz, W.J. MacKnight, Fourier transform infra-red spectroscopy on the thermo-oxidative degradation of polybenzimidazole and of a polybenzimidazole/polyetherimide blend, Polymer 34(14) (1993) 2934-2945.

[52] P. Liu, M. Mullins, T. Bremner, J.A. Browne, H.-J. Sue, Hygrothermal behavior of polybenzimidazole, Polymer 93 (2016) 88-98.

[53] M.E. Dokukin, I. Sokolov, Quantitative mapping of the elastic modulus of soft materials with HarmoniX and PeakForce QNM AFM modes, Langmuir 28(46) (2012) 16060-16071.

[54] B.X. Yang, J.H. Shi, K. Pramoda, S.H. Goh, Enhancement of the mechanical properties of polypropylene using polypropylene-grafted multiwalled carbon nanotubes, Composites Science and Technology 68(12) (2008) 2490-2497.

[55] S. Pujari, T. Ramanathan, K. Kasimatis, J. Masuda, R. Andrews, J.M. Torkelson, L.C. Brinson, W.R. Burghardt, Preparation and characterization of multiwalled carbon nanotube dispersions in polypropylene: Melt mixing versus solid-state shear pulverization, J Polym Sci Pol Phys 47(14) (2009) 1426-1436.

[56] J.G. Simmons, Generalized formula for the electric tunnel effect between similar electrodes separated by a thin insulating film, Journal of Applied Physics 34(6) (1963) 1793-1803.

[57] K. Jeon, L. Lumata, T. Tokumoto, E. Steven, J. Brooks, R.G. Alamo, Low electrical conductivity threshold and crystalline morphology of single-walled carbon nanotubes-high density polyethylene nanocomposites characterized by SEM, Raman spectroscopy and AFM, Polymer 48(16) (2007) 4751-4764.

[58] K. Jeon, S. Warnock, C. Ruiz‐Orta, A. Kismarahardja, J. Brooks, R.G. Alamo, Role of matrix crystallinity in carbon nanotube dispersion and electrical conductivity of iPP‐based nanocomposites, Journal of Polymer Science Part B: Polymer Physics 48(19) (2010) 2084-2096.

[59] L.A. Girifalco, M. Hodak, R.S. Lee, Carbon nanotubes, buckyballs, ropes, and a universal graphitic potential, Physical Review B 62(19) (2000) 13104.

[60] Y. Qin, L. Liu, J. Shi, W. Wu, J. Zhang, Z.X. Guo, Y. Li, D. Zhu, Large-scale preparation of solubilized carbon nanotubes, Chemistry of Materials 15(17) (2003) 3256-3260.

[61] B.P. Grady, F. Pompeo, R.L. Shambaugh, D.E. Resasco, Nucleation of polypropylene crystallization by single-walled carbon nanotubes, The Journal of Physical Chemistry B 106(23) (2002) 5852-5858.

[62] V. Causin, B.-X. Yang, C. Marega, S.H. Goh, A. Marigo, Nucleation, structure and lamellar morphology of isotactic polypropylene filled with polypropylene-grafted multiwalled carbon nanotubes, European Polymer Journal 45(8) (2009) 2155-2163.

[63] L. Valentini, J. Biagiotti, J. Kenny, S. Santucci, Effects of single‐walled carbon nanotubes on the crystallization behavior of polypropylene, Journal of Applied Polymer Science 87(4) (2003) 708-713.

[64] D. Bikiaris, A. Vassiliou, K. Chrissafis, K. Paraskevopoulos, A. Jannakoudakis, A. Docoslis, Effect of acid treated multi-walled carbon nanotubes on the mechanical, permeability, thermal properties and thermo-oxidative stability of isotactic polypropylene, Polymer Degradation and Stability 93(5) (2008) 952-967.

[65] A.R. Bhattacharyya, T. Sreekumar, T. Liu, S. Kumar, L.M. Ericson, R.H. Hauge, R.E. Smalley, Crystallization and orientation studies in polypropylene/single wall carbon nanotube composite, Polymer 44(8) (2003) 2373-2377.

[66] E. Assouline, A. Lustiger, A. Barber, C. Cooper, E. Klein, E. Wachtel, H. Wagner, Nucleation ability of multiwall carbon nanotubes in polypropylene composites, Journal of Polymer Science Part B: Polymer Physics 41(5) (2003) 520-527.

[67] M.L. Manchado, L. Valentini, J. Biagiotti, J. Kenny, Thermal and mechanical properties of single-walled carbon nanotubes–polypropylene composites prepared by melt processing, Carbon 43(7) (2005) 1499-1505.

[68] H.E. Miltner, N. Grossiord, K. Lu, J. Loos, C.E. Koning, B. Van Mele, Isotactic polypropylene/carbon nanotube composites prepared by latex technology. Thermal analysis of carbon nanotube-induced nucleation, Macromolecules 41(15) (2008) 5753-5762.

[69] M. Razavi‐Nouri, Effect of carbon nanotubes on dynamic mechanical properties, TGA, and crystalline structure of polypropylene, Journal of Applied Polymer Science 124(3) (2012) 2541-2549.

[70] T. Kashiwagi, E. Grulke, J. Hilding, R. Harris, W. Awad, J. Douglas, Thermal degradation and flammability properties of poly (propylene)/carbon nanotube composites, Macromolecular Rapid Communications 23(13) (2002) 761-765.

[71] T. Kashiwagi, E. Grulke, J. Hilding, K. Groth, R. Harris, K. Butler, J. Shields, S. Kharchenko, J. Douglas, Thermal and flammability properties of polypropylene/carbon nanotube nanocomposites, Polymer 45(12) (2004) 4227-4239.

[72] J. Yang, Y. Lin, J. Wang, M. Lai, J. Li, J. Liu, X. Tong, H. Cheng, Morphology, thermal stability, and dynamic mechanical properties of atactic polypropylene/carbon nanotube composites, Journal of Applied Polymer Science 98(3) (2005) 1087-1091.

[73] S.B. Kharchenko, J.F. Douglas, J. Obrzut, E.A. Grulke, K.B. Migler, Flow-induced properties of nanotube-filled polymer materials, Nature Materials 3(8) (2004) 564-568.

[74] T. Kashiwagi, F. Du, J.F. Douglas, K.I. Winey, R.H. Harris, J.R. Shields, Nanoparticle networks reduce the flammability of polymer nanocomposites, Nature Materials 4(12) (2005) 928-933.

[75] C.-C. Chu, K.L. White, P. Liu, X. Zhang, Y. Ryousho, H.J. Sue, Electrical conductivity and thermal stability of polypropylene containing well-dispersed multi-walled carbon nanotubes disentangled with exfoliated nanoplatelets, Carbon, (2012).

[76] D. Sun, W.N. Everett, C.C. Chu, H.J. Sue, Single walled carbon nanotube dispersion with electrostatically tethered nanoplatelets, Small 5(23) (2009) 2692-2697.

[77] K.L. White, M. Shuai, X. Zhang, H.J. Sue, R. Nishimura, Electrical conductivity of well-exfoliated single-walled carbon nanotubes, Carbon 49(15) (2011) 5124-5131.

[78] X. Zhang, H.J. Sue, R. Nishimura, Electrostatically controlled isolation of debundled SWCNTs from nanoplatelet dispersant, Journal of Materials Chemistry 22(13) (2012) 6156-6164.

[79] L. Sun, W.J. Boo, H.J. Sue, A. Clearfield, Preparation of α-zirconium phosphate nanoplatelets with wide variations in aspect ratios, New J Chem 31(1) (2006) 39-43.

[80] L. Sun, W.J. Boo, R.L. Browning, H.J. Sue, A. Clearfield, Effect of crystallinity on the intercalation of monoamine in α-zirconium phosphate layer structure, Chem Mater 17(23) (2005) 5606-5609.

[81] W.J. Boo, L.Y. Sun, J. Liu, A. Clearfield, H.J. Sue, M.J. Mullins, H. Pham, Morphology and mechanical behavior of exfoliated epoxy/α-zirconium phosphate nanocomposites, Compos Sci Techn 67(2) (2007) 262-269.

[82] J. Frank, Electron tomography, Springer U.S., (1992).

[83] H. Jinnai, R.J. Spontak, T. Nishi, Transmission electron microtomography and polymer nanostructures, Macromolecules 43(4) (2010) 1675-1688.

[84] J. Park, K. Eom, O. Kwon, S. Woo, Chemical etching technique for the investigation of melt-crystallized isotactic polypropylene spherulite and lamellar morphology by scanning electron microscopy, Microsc Microanal 7(3) (2001) 276-286.

[85] S. Zhang, M.L. Minus, L. Zhu, C.P. Wong, S. Kumar, Polymer transcrystallinity induced by carbon nanotubes, Polymer 49(5) (2008) 1356-1364.

[86] K. Lu, N. Grossiord, C.E. Koning, H.E. Miltner, B. Mele, J. Loos, Carbon nanotube/isotactic polypropylene composites prepared by latex technology: morphology analysis of CNT-induced nucleation, Macromolecules 41(21) (2008) 8081-8085.

[87] H. Jinnai, K. Sawa, T. Nishi, Direct observation of twisted grain boundary in a block copolymer lamellar nanostructure, Macromolecules 39(17) (2006) 5815-5819.

[88] H. Jinnai, Y. Nishikawa, R.J. Spontak, S.D. Smith, D.A. Agard, T. Hashimoto, Direct measurement of interfacial curvature distributions in a bicontinuous block copolymer morphology, Physical Review Letters 84(3) (2000) 518.

[89] H. Jinnai, T. Kaneko, K. Matsunaga, C. Abetz, V. Abetz, A double helical structure formed from an amorphous, achiral ABC triblock terpolymer, Soft Matter 5(10) (2009) 2042-2046.

[90] H. Jinnai, R.J. Spontak, Transmission electron microtomography in polymer research, Polymer 50(5) (2009) 1067-1087.

[91] Q. Zeng, A. Yu, G. Lu, Multiscale modeling and simulation of polymer nanocomposites, Progress in Polymer Science 33(2) (2008) 191-269.

[92] H. Nishioka, K.-I. Niihara, T. Kaneko, J. Yamanaka, T. Inoue, T. Nishi, H. Jinnai, Three-dimensional structure of a polymer/clay nanocomposite characterized by transmission electron microtomography, Composite Interfaces 13(7) (2006) 589-603.

[93] H. Jinnai, Y. Shinbori, T. Kitaoka, K. Akutagawa, N. Mashita, T. Nishi, Three-dimensional structure of a nanocomposite material consisting of two kinds of nanofillers and rubbery matrix studied by transmission electron microtomography, Macromolecules 40(18) (2007) 6758-6764.

[94] A. Turner-Jones, J.M. Aizlewood, D.R. Beckett, Crystalline forms of isotactic polypropylene, Die Makromolekulare Chemie 75(1) (1964) 134-158.

[95] T. Inada, H. Masunaga, S. Kawasaki, M. Yamada, K. Kobori, K. Sakurai, Small-angle x-ray scattering from multi-walled carbon nanotubes (CNTs) dispersed in polymeric matrix, Chemistry Letters 34(4) (2005) 524-525.

[96] M. Fujiyama, T. Wakino, Crystal orientation in injection molding of talc‐filled polypropylene, Journal of Applied Polymer Science 42(1) (1991) 9-20.

[97] Q. Zheng, Y. Shangguan, S. Yan, Y. Song, M. Peng, Q. Zhang, Structure, morphology and non-isothermal crystallization behavior of polypropylene catalloys, Polymer 46(9) (2005) 3163-3174.

[98] Y. Jin, M. Rogunova, A. Hiltner, E. Baer, R. Nowacki, A. Galeski, E. Piorkowska, Structure of polypropylene crystallized in confined nanolayers, Journal of Polymer Science Part B: Polymer Physics 42(18) (2004) 3380-3396.

[99] C.A. Avila-Orta, F.J. Medellin-Rodriguez, M.V. Davila-Rodriguez, Y.A. Aguirre-Figueroa, K. Yoon, B.S. Hsiao, Morphological features and melting behavior of nanocomposites based on isotactic polypropylene and multiwalled carbon nanotubes, J Appl Polym Sci 106(4) (2007) 2640-2647.

[100] B. Chu, B.S. Hsiao, Small-angle X-ray scattering of polymers, Chem Rev 101(6) (2001) 1727-1762.

[101] Z. Xia, H.J. Sue, Z. Wang, C.A. Avila-Orta, B.S. Hsiao, Determination of crystalline lamellar thickness in poly(ethylene terephthalate) using small-angle x-ray scattering and transmission electron microscopy, Journal of Macromolecular Science, Part B 40(5) (2001) 625-638.

[102] G.R. Strobl, M. Schneider, Direct evaluation of the electron density correlation function of partially crystalline polymers, Journal of Polymer Science: Polymer Physics Edition 18(6) (1980) 1343-1359.

[103] P. Jacoby, B.H. Bersted, W.J. Kissel, C.E. Smith, Studies on the β-crystalline form of isotactic polypropylene, J Polym Sci Pol Phys 24(3) (1986) 461-491.

[104] N. McCrum, The kinetics of the α and β relaxations in isotactic polypropylene, Polymer 25(3) (1984) 299-308.

[105] J. Crissman, J. Sauer, A. Woodward, Dynamic mechanical behavior of some high polymers at temperatures from 6° K.: Polyethylene, nylon 66, polypropylene, poly (vinyl chloride), poly‐(d, l‐propylene oxide), polybutene‐1, poly (4‐methyl‐pentene‐1), poly (methyl methacrylate), poly (ethyl methacrylate), poly‐4‐methylpentene‐1 and poly (isobutyl methacrylate), Journal of Polymer Science Part A: Polymer Chemistry 2(12) (1964) 5075-5091.

[106] M. Cadek, J.N. Coleman, K.P. Ryan, V. Nicolosi, G. Bister, A. Fonseca, J.B. Nagy, K. Szostak, F. Beguin, W.J. Blau, Reinforcement of polymers with carbon nanotubes: the role of nanotube surface area, Nano Lett 4(2) (2004) 353-356.

[107] M.T. Byrne, Y.K. Gun'ko, Recent advances in research on carbon nanotube–polymer composites, Advanced Materials 22(15) (2010) 1672-1688.

[108] M. Raab, J. Scudla, J. Kolarik, The effect of specific nucleation on tensile mechanical behaviour of isotactic polypropylene, European Polymer Journal 40(7) (2004) 1317-1323.

[109] M. Fujiyama, T. Wakino, Distribution of higher‐order structures in injection moldings of particulate‐filled polypropylenes, Journal of Applied Polymer Science 43(1) (1991) 97-128.

[110] N. Ning, S. Fu, W. Zhang, F. Chen, K. Wang, H. Deng, Q. Zhang, Q. Fu, Realizing the enhancement of interfacial interaction in semicrystalline polymer/filler composites via interfacial crystallization, Progress in Polymer Science 37(10) (2012) 1425-1455.

[111] E.J. Clark, J.D. Hoffman, Regime III crystallization in polypropylene, Macromolecules 17(4) (1984) 878-885.

[112] K. Liao, S. Li, Interfacial characteristics of a carbon nanotube–polystyrene composite system, Applied Physics Letters 79(25) (2001) 4225-4227.

[113] M. Wong, M. Paramsothy, X. Xu, Y. Ren, S. Li, K. Liao, Physical interactions at carbon nanotube-polymer interface, Polymer 44(25) (2003) 7757-7764.

[114] T.-H. Lee, H.-J. Sue, X. Cheng, Solid-state dye-sensitized solar cells based on ZnO nanoparticle and nanorod array hybrid photoanodes, Nanoscale Res Lett 6(1) (2011) 1-8.

[115] T.-H. Lee, H.-J. Sue, X. Cheng, ZnO and conjugated polymer bulk heterojunction solar cells containing ZnO nanorod photoanode, Nanotechnology 22(28) (2011) 285401.

[116] P. Liu, R.L. Browning, H.-J. Sue, J. Li, S. Jones, Quantitative scratch visibility assessment of polymers based on Erichsen and ASTM/ISO scratch testing methodologies, Polymer Testing 30(6) (2011) 633-640.

[117] D.P.N. Vlasveld, J. Groenewold, H.E.N. Bersee, S.J. Picken, Moisture absorption in polyamide-6 silicate nanocomposites and its influence on the mechanical properties, Polymer 46(26) (2005) 12567-12576.

[118] R.D. Adams, M.M. Singh, The dynamic properties of fibre-reinforced polymers exposed to hot, wet conditions, Composites Science and Technology 56(8) (1996) 977-997.

[119] R.J. Morgan, J.E. O'neal, D.L. Fanter, The effect of moisture on the physical and mechanical integrity of epoxies, Journal of Materials Science 15(3) (1980) 751-764.

[120] H. Jiang, R. Browning, P. Liu, T.A. Chang, H.-J. Sue, Determination of epoxy coating wet-adhesive strength using a standardized ASTM/ISO scratch test, Journal of Coatings Technology and Research 8(2) (2011) 255-263.

[121] T. Sugama, Hydrothermal degradation of polybenzimidazole coating, Materials Letters 58(7–8) (2004) 1307-1312.

[122] C. Arnold, Stability of high-temperature polymers, Journal of Polymer Science: Macromolecular Reviews 14(1) (1979) 265-378.

[123] H. Vogel, C.S. Marvel, Polybenzimidazoles, new thermally stable polymers, Journal of Polymer Science 50(154) (1961) 511-539.

[124] H. Vogel, C. Marvel, Polybenzimidazoles. II, Journal of Polymer Science Part A: General Papers 1(5) (1963) 1531-1541.

[125] J. Critchley, G. Knight, W.W. Wright, Heat-resistant polymers: Technologically useful materials, 2nd ed., Springer Science & Business Media, U.S. (1986).

[126] K. Friedrich, H.J. Sue, P. Liu, A.A. Almajid, Scratch resistance of high performance polymers, Tribology International 44(9) (2011) 1032-1046.

[127] S. Sharma, E. Padenko, J. Bijwe, B. Wetzel, K. Friedrich, Erosive and sliding wear of polybenzimidazole at elevated temperatures, Journal of Materials Science 51(1) (2016) 262-270.

[128] V.V. Korshak, M.M. Teplyakov, R.D. Fedorova, Synthesis and investigation of polybenzimidazoles containing alkyl substituents in aromatic nuclei, Journal of Polymer Science Part A-1: Polymer Chemistry 9(4) (1971) 1027-1043.

[129] C.D. Dudgeon, O. Vogl, Bisorthoesters as polymer intermediates. II. A facile method for the preparation of polybenzimidazoles, Journal of Polymer Science: Polymer Chemistry Edition 16(8) (1978) 1831-1852.

[130] W. Wrasidlo, R. Empey, Pyrolysis of polyaromatic heterocyclics, Journal of Polymer Science Part A-1: Polymer Chemistry 5(7) (1967) 1513-1526.

[131] P.M. Hergenrother, W. Wrasidlo, H.H. Levine, Polybenzothiazoles. I. Synthesis and preliminary stability evaluation, Journal of Polymer Science Part A: General Papers 3(5) (1965) 1665-1674.

[132] S. Qing, W. Huang, D. Yan, Synthesis and characterization of thermally stable sulfonated polybenzimidazoles, European Polymer Journal 41(7) (2005) 1589-1595.

[133] K.J. Scariah, V.N. Krishnamurthy, K.V.C. Rao, M. Srinivasan, Synthesis and properties of new polybenzimidazoles and N-phenyl polybenzimidazoles with flexibilizing spacers on the polymer backbone, Journal of Polymer Science Part A: Polymer Chemistry 25(10) (1987) 2675-2687.

[134] S.-K. Kim, T.-H. Kim, T. Ko, J.-C. Lee, Cross-linked poly(2,5-benzimidazole) consisting of wholly aromatic groups for high-temperature PEM fuel cell applications, Journal of Membrane Science 373(1–2) (2011) 80-88.

[135] H. Luo, H. Pu, Z. Chang, D. Wan, H. Pan, Crosslinked polybenzimidazole via a Diels–Alder reaction for proton conducting membranes, Journal of Materials Chemistry 22(38) (2012) 20696.

[136] H. Xu, K. Chen, X. Guo, J. Fang, J. Yin, Synthesis of novel sulfonated polybenzimidazole and preparation of cross-linked membranes for fuel cell application, Polymer 48(19) (2007) 5556-5564.

[137] G.P. Shulman, W. Lochte, Thermal Degradation of Polymers. IV. Poly-2,2′-(m-phenylene)-5,5′-bibenzimidazole, Journal of Macromolecular Science: Part A - Chemistry 1(3) (1967) 413-428.

[138] Y. Tsur, Y.L. Freilich, M. Levy, TGA–MS degradation studies of some new aliphatic–aromatic polybenzimidazoles, Journal of Polymer Science: Polymer Chemistry Edition 12(7) (1974) 1531-1539.

[139] L.R. Belohlav, Polybenzimidazole, Die Angewandte Makromolekulare Chemie 40(1) (1974) 465-483.

[140] J. Guenther, M. Wong, H.-J. Sue, T. Bremner, J. Blümel, High-temperature steam-treatment of PBI, PEKK, and a PEKK-PBI Blend: A solid-state NMR and IR spectroscopic study, Journal of Applied Polymer Science 128(6) (2013) 4395-4404.

[141] J.C. Pope, H.-J. Sue, T. Bremner, J. Blümel, High-temperature steam-treatment of PBI, PEEK, and PEKK polymers with H2O and D2O: A solid-state NMR study, Polymer 55(18) (2014) 4577-4585.

[142] Y. Tsur, H.H. Levine, M. Levy, Effects of structure on properties of some new aromatic‐aliphatic polybenzimidazoles, Journal of Polymer Science: Polymer Chemistry Edition 12(7) (1974) 1515-1529.

[143] A.R. Katritzky, K. Sakizadeh, J. Swinson, S.M. Heilmann, J.K. Rasmussen, L.R. Krepski, D.M. Moren, H.K. Smith, S.V. Pathre, Azlactones as polymer components and

intermediates, Journal of Polymer Science Part A: Polymer Chemistry 27(5) (1989) 1781-1790.

[144] R.T. Conley, J.J. Kane, S. Ghosh, Mechanism of Thermal Oxidation of the Benzimidazole System, DTIC Document, 1971.

[145] S. Samms, S. Wasmus, R. Savinell, Thermal stability of proton conducting acid doped polybenzimidazole in simulated fuel cell environments, Journal of the Electrochemical Society 143(4) (1996) 1225-1232.

[146] I.B. Valtcheva, S.C. Kumbharkar, J.F. Kim, Y. Bhole, A.G. Livingston, Beyond polyimide: Crosslinked polybenzimidazole membranes for organic solvent nanofiltration (OSN) in harsh environments, Journal of Membrane Science 457 (2014) 62-72.

[147] S.E. Keinath, R.J. Morgan, Moisture content of aramid and polybenzimidazole fibers, Thermochimica Acta 166 (1990) 17-26.

[148] N.W. Brooks, R.A. Duckett, J. Rose, I.M. Ward, J. Clements, An n.m.r. study of absorbed water in polybenzimidazole, Polymer 34(19) (1993) 4038-4042.

[149] D.W. Tomlin, A.V. Fratini, M. Hunsaker, W. Wade Adams, The role of hydrogen bonding in rigid-rod polymers: the crystal structure of a polybenzobisimidazole model compound, Polymer 41(25) (2000) 9003-9010.

[150] B.C. Ward, E. Alvarez, R.S. Blake, Sintered polybenzimidazole article, Google Patents, 1989.

[151] Y. Takahashi, Crystal Structure of Poly(pyridobisimidazole), PIPD, Macromolecules 36(23) (2003) 8652-8655.

[152] A. Sannigrahi, S. Ghosh, S. Maity, T. Jana, Structurally isomeric monomers Directed copolymerization of polybenzimidazoles and their properties, Polymer 51(25) (2010) 5929-5941.

[153] H.J. Sue, Study of rubber‐modified brittle epoxy systems. Part I: Fracture toughness measurements using the double‐notch four‐point‐bend method, Polymer Engineering & Science 31(4) (1991) 270-274.

[154] S. Zhu, L. Yan, D. Zhang, Q. Feng, Molecular dynamics simulation of microscopic structure and hydrogen bond network of the pristine and phosphoric acid doped polybenzimidazole, Polymer 52(3) (2011) 881-892.

[155] Mass spectrum of Ammonia, NIST mass spectrometry data center, (2014).

[156] A. Yee, S. Smith, Molecular structure effects on the dynamic mechanical spectra of polycarbonates, Macromolecules 14(1) (1981) 54-64.

[157] P.B. Messersmith, E.P. Giannelis, Synthesis and characterization of layered silicate-epoxy nanocomposites, Chemistry of Materials 6(10) (1994) 1719-1725.

[158] L.C.E. Struik, Physical aging in amorphous polymers and other materials, TU Delft, Delft University of Technology, 1977.

[159] Y. Park, J. Ko, T.-K. Ahn, S. Choe, Moisture effects on the glass transition and the low temperature relaxations in semiaromatic polyamides, Journal of Polymer Science Part B: Polymer Physics 35(5) (1997) 807-815.

[160] K. Pramoda, T. Liu, Effect of moisture on the dynamic mechanical relaxation of polyamide‐6/clay nanocomposites, Journal of Polymer Science Part B: Polymer Physics 42(10) (2004) 1823-1830.

[161] Y. Li, J. Miranda, H.-J. Sue, Hygrothermal diffusion behavior in bismaleimide resin, Polymer 42(18) (2001) 7791-7799.

[162] H.J. Kim, Z. Brunovska, H. Ishida, Dynamic mechanical analysis on highly thermally stable polybenzoxazines with an acetylene functional group, Journal of Applied Polymer Science 73(6) (1999) 857-862.

[163] W.F. Brown, Review of developments in plane strain fracture toughness testing, ASTM International1970.

[164] H.-J. Sue, A.F. Yee, Toughening mechanisms in a multi-phase alloy of nylon 6, 6/polyphenylene oxide, Journal of Materials Science 24(4) (1989) 1447-1457.

[165] L.P. Suffredini, Sintered polymers, US Patent 3,340,325, 1967.

[166] J.S. Letinski, Process for the production of molded polybenzimidazole articles and the resultant articles, Google Patents, 1988.

[167] S.B. Shen, H. Ishida, Dynamic mechanical and thermal characterization of high-performance polybenzoxazines, Journal of Polymer Science Part B Polymer Physics 37(23) (1999) 3257-3268.

[168] D. Blundell, On the interpretation of multiple melting peaks in poly (ether ether ketone), Polymer 28(13) (1987) 2248-2251.

[169] A. Arzak, J. Eguiazabal, J. Nazabal, Compatibility in immiscible poly (ether ether ketone)/poly (ether sulfone) blends, Journal of Applied Polymer Science 58(3) (1995) 653-661.

[170] M.B. Djordjevic, R.S. Porter, NMR characterization of intermolecular interactions for polymers, IV. Intermolecular interactions of low molecular weight analogues for compatible blends of polystyrene and poly (2, 6 - dimethyl - 1, 4 - phenylene oxide), Polymer Engineering & Science 23(12) (1983) 650-657.

[171] K. Ivanova, R. Pethrick, S. Affrossman, Investigation of hydrothermal ageing of a filled rubber toughened epoxy resin using dynamic mechanical thermal analysis and dielectric spectroscopy, Polymer 41(18) (2000) 6787-6796.

[172] R.H. Petrucci, W.S. Harwood, F. Herring, General Chemistry, Principles and Modern Applications, Journal of Chemical Education 74(5) (1997) 491-491.

[173] J. Karger-Kocsis, K. Friedrich, Temperature and strain-rate effects on the fracture toughness of poly (ether ether ketone) and its short glass-fibre reinforced composite, Polymer 27(11) (1986) 1753-1760.

[174] G.M. Wu, J.M. Schultz, Fracture behavior of oriented poly (ether - ether - ketone)(PEEK), Polymer Engineering & Science 29(6) (1989) 405-414.

[175] H.L. Chen, R.S. Porter, Phase and crystallization behavior of solution - blended poly (ether ether ketone) and poly (ether imide), Polymer Engineering & Science 32(24) (1992) 1870-1875.